

RS-8232-2/169187

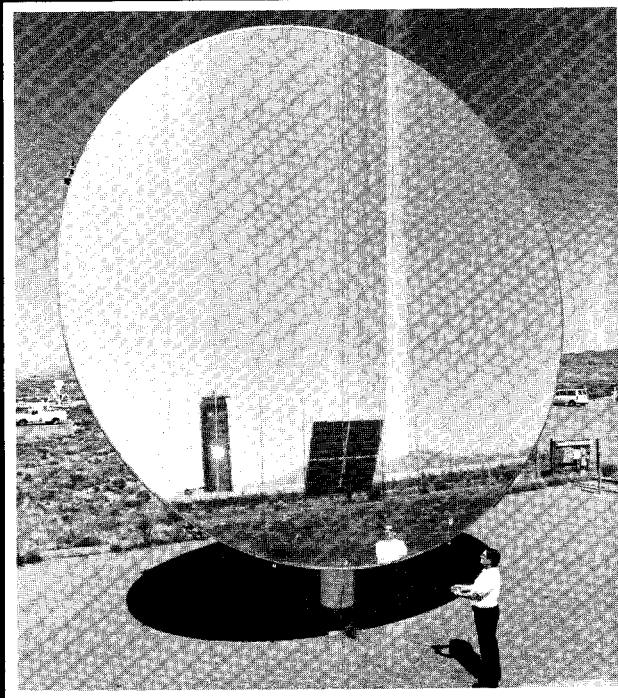
cy



8232-2/069187



00000001 -



An Improved Design for Stretched- Membrane Heliostats

by Science Applications
International Corporation

Issued by Sandia National Laboratories, operated for the United States Department of Energy by Sandia Corporation.

NOTICE: This report was prepared as an account of work sponsored by an agency of the United States Government. Neither the United States Government nor any agency thereof, nor any of their employees, nor any of their contractors, subcontractors, or their employees, makes any warranty, express or implied, or assumes any legal liability or responsibility for the accuracy, completeness, or usefulness of any information, apparatus, product or process disclosed, or represents that its use would not infringe privately owned rights. Reference herein to any specific commercial product, process, or service by trade name, trademark, manufacturer, or otherwise, does not necessarily constitute or imply its endorsement, recommendation, or favoring by the United States Government, any agency thereof or any of their contractors or subcontractors. The views and opinions expressed herein do not necessarily state or reflect those of the United States Government, any agency thereof or any of their contractors.

Printed in the United States of America. This report has been reproduced directly from the best available copy.

Available to DOE and DOE contractors from
Office of Scientific and Technical Information
PO Box 62
Oak Ridge, TN 37831

Prices available from (615) 576-8401, FTS 626-8401

Available to the public from
National Technical Information Service
US Department of Commerce
5285 Port Royal Rd
Springfield, VA 22161

NTIS price codes
Printed copy: A08
Microfiche copy: A01

Cover design: Gene Clardy, Sandia National Laboratories

Cover photos: Randy Montoya, Sandia National Laboratories

SAND89-7027
Unlimited Release
Printed June 1989

AN IMPROVED DESIGN FOR
STRETCHED-MEMBRANE HELIOSTATS

Kelly Beninga
Barry Butler, Ph.D.
Jeff Sandubrae
Kerry Walcott

Science Applications International Corporation
Energy Projects Division
10401 Roselle Street
San Diego, CA 92121

Sandia Contract 33-1226

ABSTRACT

Science Applications International Corporation (SAIC) has developed an improved stretched-membrane heliostat mirror module under contract to Sandia National Laboratories, Albuquerque, New Mexico. Both a 150-m² commercial mirror module and a 50-m² prototype mirror module have been designed. The prototype mirror module has been fabricated and is being tested at the Central Receiver Test Facility (CRTF) in Albuquerque. Two .0762-mm (.003-in) thick stainless steel membranes are stressed to approximately 90 MPa (13,000 psi) and welded to either side of a carbon steel, rectangular cross-section ring, which is compressed to approximately one-tenth of its yield strength. The ring is supported by five trusses, which radiate from a central hub. The mirror module is mounted on a conventional pedestal drive system for sun-tracking purposes. The mirror module is air-tight, and focusing is achieved by modulating the position of the back membrane. The ring stiffness and tolerance achievable by conventional manufacturing methods dictate the ring distortions prior to installation of the mirror module. Once the mirror module is installed, wind loads on the heliostat exert additional out-of-plane loads. A comprehensive finite-element computer model of the mirror module was used for the structural design of the ring/membrane system and truss supports. The analysis and design methods used are reported, and an improved mirror module design is described. Preliminary test results indicate the prototype mirror module meets all design and performance goals. The unit has a full cone angle reflected beam dispersion of 2.8 mrad and can defocus in five seconds.

ACKNOWLEDGEMENT

This work was supported by the U.S. Department of Energy through Sandia National Laboratories under Contract SAND33-1226. The authors thank John Holmes, Dan Alpert, and Richard Houser of Sandia National Laboratories, Albuquerque for their support and guidance. Marty Murphy and Richard Wood of the Solar Energy Research Institute, and Dan Sallis of DAN-KA Products are also thanked for their technical support.

TABLE OF CONTENTS

<u>Section</u>	<u>Title</u>	<u>Page</u>
1.0	INTRODUCTION	1
1.1	Background	2
1.2	Design Improvements	6
2.0	DESCRIPTION OF THE IMPROVED COMMERCIAL MIRROR MODULE DESCRIPTION	8
3.0	DESIGN CRITERIA FOR THE MIRROR MODULE.	21
4.0	TRADE STUDIES FOR THE COMMERCIAL MIRROR MODULE	24
4.1	Material Selection	24
4.2	Selection of the Ring Type	26
4.3	Effects of Thermal Expansion	27
4.4	Trade Study of Ring Support Points	29
5.0	STRUCTURAL ANALYSIS OF THE COMMERCIAL MIRROR MODULE	36
5.1	Wind Load Model Description	37
5.2	Membrane Finite Element Model	39
5.3	Finite-Element Model of the Ring	46
5.4	Finite-Element Model of the Truss	49
5.5	Out-of-Plane Buckling of the Ring	56
5.6	Local Buckling of the Ring Wall	58
6.0	DESIGN OF THE FOCUS-CONTROL SYSTEM	60
6.1	Description of the Plenum Pressure Adjustment Subsystem	60
6.2	Selection of the Front Membrane Position Measurement Subsystem	67
6.3	Fluid Dynamic Analysis of the Mirror Module	69
6.4	Focus Control Logic	74

7.0	COMMERCIAL MANUFACTURING SCENARIO	78
7.1	Assembly of the Mirror Module	78
7.2	Bench Scale Model of Membrane Tensioning	82
7.3	Fabrication of the Support Truss	82
7.4	Hub Production	86
7.5	Focus/Defocus Pad Production	87
7.6	Focus Control System	88
7.7	Finishing	88
7.8	Transportation	90
7.9	Operation and Maintenance	90
8.0	COST OF THE COMMERCIAL HELIOSTAT	92
8.1	Cost Modifications	92
9.0	DESCRIPTION OF THE IMPROVED PROTOTYPE MIRROR MODULE	99
10.0	COMMERCIAL-PROTOTYPE MIRROR MODULE COMPARISON	110
11.0	STRUCTURAL ANALYSIS OF THE PROTOTYPE MIRROR MODULE	113
12.0	FABRICATION OF THE PROTOTYPE MIRROR MODULE	118
13.0	PRELIMINARY TEST RESULTS OF THE PROTOTYPE HELIOSTAT	136
14.0	SUGGESTIONS FOR FURTHER DEVELOPMENT	140
14.1	Potential Cost Reduction	140
14.2	Life of the Reflective Surface	142
14.3	Development of Commercial Tooling	143
14.4	Suggested Development Program	148
15.0	REFERENCES	146

LIST OF FIGURES

<u>Figure No.</u>	<u>Title</u>	<u>Page</u>
1.1-1	DOE Heliostat Development	3
2.0-1	150 Square Meter Heliostat Plan Views	9
2.0-2	Membrane To Ring Attachment	11
2.0-3	Ring To Membrane Weld Cross-Sections	13
2.0-4	Tubular Triangular Tapered Space Truss	15
2.0-5	Mirror Module Mounting Trunion	16
2.0-6	Commercial Truss Mounting Hub	18
4.3-1	Thermal Response of Heliostat Membrane	30
4.3-2	Thermal Response of Heliostat Ring	31
4.4-1	Weight of Ring, Trusses, and Hub Versus Number of Trusses	33
4.4-2	Material and Labor Cost of Ring, Trusses, and Hub Versus Number of Trusses	34
5.0-1	Mirror Module Finite Element Model	37
5.1-1	Wind Velocity Profiles	40
5.1-2	Wind Drag Profiles	41
5.1-3	Heliostat Wind Loading	42
5.2-1	Commercial Design Rear Membrane - Deformed Shape	44
5.2-2	Rear Membrane Stress Shading	45
5.3-1	Commercial Design Deformed Ring	47
5.3-2	Front Membrane Stress Shading For Front and Rear Truss Attachment	48
5.4-1	Commercial Design Triangular Truss Finite Element Model	50
5.4-2	Commercial Design Deformed Triangular Truss	51

5.4-3	Commercial Design Deformed Triangular Truss Magnified 500 X	52
5.4-4	Commercial Design Side Loaded Triangular Truss	53
5.4-5	Roof Truss Finite Element Model	54
5.4-6	Deformed Roof Truss 500X	55
5.5-1	Rectangular Tube Aspect Ratio Versus Magnification Factor	57
6.1-1	Focus Control System Isometric View	61
6.1-2	Membrane Modulation System Worst Case Operating Conditions	62
6.1-3	Focus Control System Diagram	64
6.1-4	Focus Pad Assembly	66
6.2-1	Focus Control - Membrane Position Measurement Options .	68
6.3-1	Linear Actuator Position Versus Ambient Temperature . .	72
6.3-2	Commercial Heliostat Predicted Focus-Control Wind Load Response Time	73
6.4-1	Focus Control Logic	75
6.4-2	Reference Positions for the Focus Control Linear Actuator	77
7.1-1	Commercial Tooling Concept For Ring Compression and Membrane Tensioning	79
7.1-2	Commercial Mirror Module Assembly	80
7.2-1	Commercial Membrane Tensioning System	83
7.2-2	Hydraulic Tensioning Tool Bench Scale Experiment (View 1)	84
7.2-3	Hydraulic Tensioning Tool Bench Scale Experiment (View 2)	84
7.2-4	Membrane Tensioning Tool	85
9.0-1	50-m ² Prototype Heliostat Plan View	100
9.0-2	Photo - Prototype Heliostat Front View	101

9.0-3	Photo - Prototype Heliostat Back View	101
9.0-4	Prototype Triangular Tapered Space Truss	103
9.0-5	Prototype Truss Mounting Hub	104
9.0-6	Hub to Truss Attachment	105
9.0-7	Installed Hub And Focus Pad	107
9.0-8	Prototype Focus Control Pad Assembly	108
11.0-1	Membrane Focusing Analysis-Membrane Deflections	115
11.0-2	Membrane Focusing Analysis-Membrane Stress	116
11.0-3	Hub Model Deformed Under Applied Loading	117
12.0-1	Second Generation Prototype Welding Fixture	120
12.0-2	Prototype Mirror Module Membrane Tensioning	121
12.0-3	Ring Section Nickel Electroplating	123
12.0-4	Prototype Ring to Truss Attachment Bracket	123
12.0-5	Membrane Welding (View 1)	124
12.0-6	Membrane Welding (View 2)	124
12.0-7	Reflective Film Lamination to Membrane	125
12.0-8	Membranes Prepared For Shipment	125
12.0-9	Prototype Truss Fabrication	126
12.0-10	Prototype Hub	126
12.0-11	Checkout of the Focus Control System Checkout	127
12.0-12	Tensioning Strips to Membrane Weld (View 1)	129
12.0-13	Tensioning Strips to Membrane Weld (View 2)	129
12.0-14	Welding of Back Membrane Porthole Reinforcement	130
12.0-15	View of Inside of Back Membrane	130
12.0-16	Membrane Tensioning	131
12.0-17	Membrane to Ring Welding	131
12.0-18	Truss/Hub Subassembly	132
12.0-19	Mirror Module Assembly	132
12.0-20	Installation of Mirror Module (View 1)	134
12.0-21	Installation of Mirror Module (View 2)	134
12.0-22	Installation of Mirror Module (View 3)	135

13.0-1	Membrane Heliostat Measured Isoflux Contours - Day 196 .	137
13.0-2	Full Beam Cone Angle at 90% Power Intercept	
	Actual Versus Helios Prediction	138
13.0-3	Defocus Time of the Membrane Heliostat	139
A-1	Wind Velocity Profiles	A-6
A-2	Wind Drag Profiles	A-7
A-3	
A-4	Diagram of the Wind Load Force	A-10
B-1	Coordinate System	B-1

LIST OF TABLES

<u>Table Number</u>	<u>Title</u>	<u>Page</u>
2.0-1	Commercial Heliostat Specifications	10
2.0-2	Stressed Membrane Mirror Module Weight	20
3.0-1	Design Criteria for the Mirror Module	22
4.2-1	Ring Cross-Section Comparison - Specific Stiffness	28
5.0-1	Analysis Results for the Commercial Design	38
6.3-1	Program Focus - Focus Control Simulation Program	77
6.4-1	Computer Menu for Focus Control	77
7.8-1	Transportation	91
7.8-2	Heliostat Trucking Load	91
8.0-1	150-m ² Second Generation Commercial Stretched Membrane Heliostat Cost	93
8.0-2	Commerical Stretched Membrane Mirror Module Cost Analysis	94
8.1-1	Direct Labor Central Manufacturing Facility	95
8.1-2	Direct Labor Field Site	96
8.1-3	Total Labor Per Heliostat	98
9.0-1	Prototype Heliostat Specifications	102
10.0-1	Heliostat Specifications	111
11.0-1	Analysis Results for the Prototype Design	114

APPENDICES

Appendix	<u>Title</u>	<u>Page</u>
A	SAIC Heliostat Design Criteria	A-1
B	Structural/Optical Coupling Equations Derivation	B-1
C	Bench Tensioning Experiment - Operating Procedure	C-1

Foreword

The research described in this report was conducted within the U. S. Department of Energy's Solar Thermal Technology Program. This program directs efforts to incorporate technically proven and economically competitive solar thermal options into our nation's energy supply. These efforts are carried out through a network of national laboratories that work with industry.

In a solar thermal system, mirrors or lenses focus sunlight onto a receiver where a working fluid absorbs the solar energy as heat. The system then converts the energy into electricity or uses it as process heat. There are two kinds of solar thermal systems: A central receiver system uses a field of heliostats (two-axis tracking mirrors) to focus the sun's radiant energy onto a receiver mounted on a tower. A distributed receiver system uses three types of optical arrangements—parabolic troughs, parabolic dishes, and hemispherical bowls—to focus sunlight onto either a line or point receiver. Distributed receivers may either stand alone or be grouped.

This report summarizes the design of a heliostat that uses a stretched-membrane reflector. The field of heliostats is the most expensive part of a central receiver power plant, so costs must be as low as possible for the technology to be commercially viable. Stretched-membrane heliostats are being developed because their simplicity and light weight should afford a considerable reduction in cost over current glass-mirror designs.

1.0 INTRODUCTION

A solar central receiver power system uses a large field of mirrors to reflect the sun's energy onto a receiver that is placed on a tower. The receiver is illuminated with concentrated sunlight to a high temperature (565°C, 1050°F), and steam is produced to drive a turbine-generator to make electricity. The concentrated solar energy can also be used to detoxify hazardous waste, or generate electricity directly with the use of a photovoltaic receiver panel. The term heliostat (helio-stat meaning sun-constant) refers to the heliostat's function of positioning the sun's reflected image on the receiver, which is at a fixed location with respect to the heliostat. As the sun moves, its reflected image remains at the same location.

Sandia National Laboratories, a prime contractor to the Department of Energy, is developing heliostats for use in solar central receiver power plants. Current efforts are directed toward the development of light-weight heliostats that employ reflective surfaces mounted on stretched membranes. The stretched-membrane concept is radically different from current glass/metal designs in that the mirror module consists of two thin metal membranes stretched over either side of a large-diameter metal ring. The reflective surface is a silvered polymer film laminated onto the front membrane. The pressure in the space between the two membranes is actively controlled to provide a concave shape to the reflective surface for focusing. The space between the metal membranes can also be quickly pressurized to defocus the mirror for safety procedures.

In FY86, two parallel studies evaluating the feasibility and cost effectiveness of stretched-membrane heliostats for solar central receiver systems were completed. These studies, performed under contract to Sandia, were divided into two phases. In the first phase the design, ease of fabrication, and cost of a commercial-scale, mass-produced heliostat were studied. In the second phase, each contractor fabricated and installed a 50-m² prototype mirror module for testing and evaluation at the Central Receiver Test Facility (CRTF) in Albuquerque, NM. The two parallel studies were performed by Science Applications International Corporation (SAIC) [1] and Solar Kinetics, Inc. (SKI) [2]. Both contractors selected a mirror area of 150 m² for their optimal commercial-scale heliostat design. Both contractors concluded that stretched-membrane heliostats

were feasible and cost effective for solar central receiver systems. Stretched-membrane heliostats were found to be simpler and lighter in weight than glass/metal designs. Moreover, the cost per square meter of an installed heliostat was estimated to be between 15 and 20% less for stretched-membrane heliostats in mass production than for a comparable glass/metal design.

In the design and fabrication of the prototype mirror module, SAIC identified a number of areas where additional improvements in the design and manufacturing might be possible. A second contract was awarded to SAIC and SKI to improve the commercial-scale and prototype heliostat designs produced under the first contracts.

This report describes the analysis and design of an improved commercial-scale (150-m²) stretched-membrane mirror module, and the design, fabrication, and initial test results of an improved 50-m² prototype mirror module.

1.1 Background

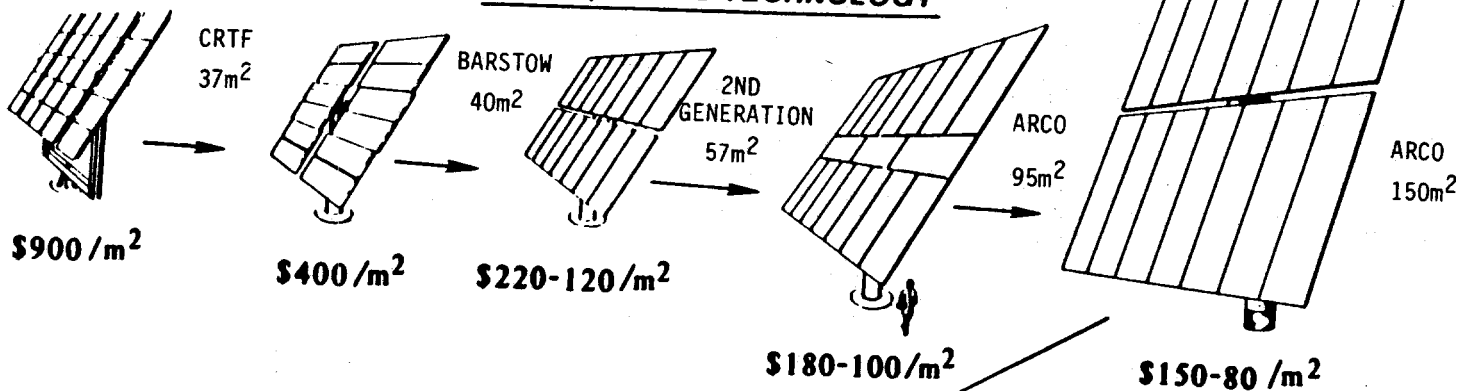
Early heliostats were made from small, flat, or slightly concave mirror facets made of silvered glass with a rigid backing. With all heliostats, a tracking mechanism is needed for each heliostat to keep the sun's image on the tower. Since trackers are expensive, the larger the reflector a tracker can carry, the less the heliostat costs per square meter of reflector. Figure 1.1-1 shows the trends in DOE's heliostat development program in the last 10 years. Heliostat size has increased by adding more and larger mirror facets to steel truss support structures. These heliostats are referred to as glass/metal heliostats.

Research on stretched-membrane heliostats is being pursued because of the significantly lower cost and weight potential of this design concept as compared to more conventional glass/metal heliostats. The basic precept of the design is that a metal foil membrane, when placed in uniform tension, provides an excellent substrate for an optically reflective surface.

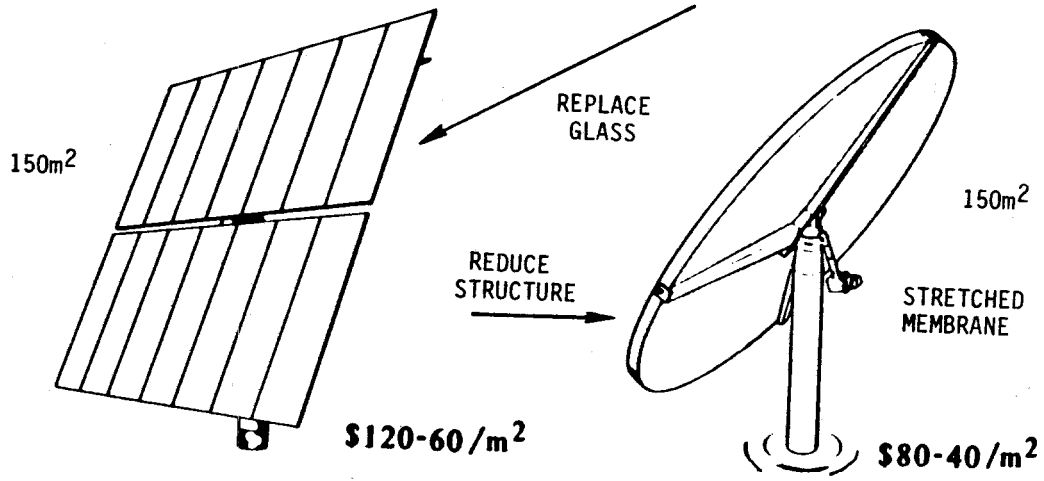
SAIC developed and fabricated a first-of-a-kind 50-m² stretched-membrane mirror module in 1986. Both a 150-m² commercial mirror module for mass production and a 50-m² prototype mirror module were designed. Fabrication of the prototype mirror module was completed in September 1986 at the CRTF.

**DOE
SOLAR THERMAL TECHNOLOGY
HELIOSTAT R&D**

GLASS/METAL TECHNOLOGY



SILVER POLYMER AND SILVER STEEL TECHNOLOGY



SAIC-86BLB-203

Figure 1.1-1. DOE Heliostat Development

This first mirror module design consisted of a ring of circular cross-section with stainless steel membranes on both sides of the ring. The membranes were made up of .0762-mm (.003-in) thick, .61-m (24-in) wide Type 304 stainless steel strips, which were roll-resistance welded together. The membranes were then tensioned by inflating a tensioning bladder, which was placed around the circumference of the ring between the ring wall and the membranes, prior to welding the top and bottom membranes together around the perimeter.

Much information was gained from the fabrication and testing of the first-generation prototype mirror module. The out-of-plane ring distortions were greater than expected due to non-uniform membrane stress caused by manufacturing errors and an undersized support ring. The resulting stress non-uniformity in the back membrane caused ring out-of-plane bending forces, which in turn caused the ring to saddle or "potato chip" ($n = 2$ deformation mode) as the membrane tension was increased.

The loads on heliostats are mainly caused by gravity and wind loading. In glass/metal heliostats, gravity loads are aggregated from the mirror facets and transferred into a structural truss network that ultimately delivers these loads to an azimuth and elevation drive system, usually located near the center of the back of the heliostat.

Optical accuracy is determined by the shape of the individual mirror facets, i.e., their spherical curvature, and by the rigidity with which they can be supported to aim at a common point in space. In the absence of wind loading, faceted heliostats could be designed utilizing stiffness-to-weight criteria to minimize the optical errors due to distortion of the heliostat frame under gravity loading. However, because this structure must be designed to meet wind loads of 22.3 m/s (50 mph) in any direction and up to 40.2 m/s (90 mph) in a horizontal stow position, the heliostat structure is strength limited. The wind-load strength requirements exceed the optical stiffness requirements.

Under normal operation in conventional faceted-mirror-panel heliostats, the working stress in most of the components is very low, and the average overall stress in the material is on the order of 0.5 to 1 MPa (a few hundred psi) in materials capable of handling 350 to 415 MPa (50,000 to 60,000 psi). As a result, the weight of conventional heliostats with a glass/facet metal truss structure tends to be in the range from 41 to 49 kg/m² (8.4 to 10 lbs/ft²). To reduce the

weight and cost of materials that go into the manufacture of the heliostat, it is necessary to operate the structure at a higher fraction of its available working stress. The stressed-membrane design described in this report results in a mirror and support structure weight of 13.8 kg/m^2 (2.8 lb/ft^2).

The utilization of stretched membranes to achieve low weight was initially demonstrated by the Boeing Company and the General Electric Company in 1976 [3 - 6]. They used a stretched polymer reflector on a lightweight hoop that was entirely enclosed from the weather in a clear plastic bubble. These designs were built and tested in the mid-1970s as part of the Sandia/DOE advanced heliostat program. The losses sustained by transmitting solar energy into the bubble and then reflecting it back out of the bubble were not totally offset by reduced cost.

In 1978, The Solar Energy Research Institute (SERI) reviewed the Boeing and General Electric work with in bubble heliostats in efforts to develop a low-cost heliostat [7]. SERI decided that a high-performance membrane heliostat without a bubble to protect it from the environment was necessary. Initial work led to a SERI/DOE patent, with disclosure in 1979 and a proof-of-principle in early 1980 (References). This research led to a polypropylene membrane stretched at 5.253 kN/m (30 lbs/linear in) on a large-diameter (4 m) hoop. This heliostat, which had 25-cm square glass reflector tiles bonded onto a highly stressed trampoline, was the first attempt at fabricating a large-area membrane heliostat intended for exposure to a terrestrial environment.

Once the initial feasibility of a non-enclosed membrane heliostat was determined, both SERI and Sandia embarked on research programs to develop advanced heliostats based on this general concept. SERI pursued single-membrane concepts, while Sandia developed double-membrane concepts. The double-membrane concepts allowed for differential pressure focusing. Results from both SERI's membrane and ring structural research, and Sandia's double-membrane development have been utilized extensively to yield the commercial heliostat design described in this report [8 - 15].

1.2 Design Improvements

Continued development of the stretched-membrane mirror module is necessary to improve its structural integrity, optical properties, and fabricating techniques. SAIC has completed the design of an improved 150-m² commercial-scale and a 50-m² prototype-scale mirror module. Improvements in this second mirror module include:

- o a redesigned focus control system
- o use of a rectangular ring with increased out-of-plane moment of inertia
- o use of five ring support trusses instead of four
- o a revised membrane fabrication alignment procedure
- o elimination of the pressurized tensioning bladders
- o use of an external, reusable tensioning tool
- o welding of the membranes directly to the top and bottom of the rectangular ring to provide a stiffer ring/membrane structure.

Improvement in the performance of the focus control system was necessary in order to more accurately detect the position of the front membrane, and also to decrease the response time in reaction to wind load changes on the membranes. The optically based front-membrane position-detection system used on the first-generation heliostat design has been replaced with a more reliable and accurate Linear Variable Differential Transducer (LVDT) mechanical measurement system.

The approach taken to control the focal length of the front membrane on the first-generation prototype mirror module was to control the internal plenum pressure by the use of a fan or blower to move air into or out of the plenum. The response time to compensate for increases in external pressure due to wind gusts was considered to be inadequate with this type of system. The fan could simply not move a high enough volume of air in a short enough period of time to obtain the desired response. The second-generation focus-control system does not depend on the movement of air into and out of the plenum. With the improved system, internal plenum pressure changes are accomplished by actively moving the rear membrane in and out with the use of the linear actuator in order to change

the plenum volume, and therefore the plenum pressure. Since no movement of air into and out of the plenum is necessary, the mirror module can be a sealed unit. Initial tests on the prototype mirror module have shown that not only is the response time to wind gusts much faster, but also the parasitic power required for the focus-control system has been greatly reduced.

A ring of circular cross section was used in the first-generation heliostat design. Increased out-of-plane moment of inertia can be provided with the use of a channel or rectangular cross-section beam. Although these cross sections have reduced resistance to torsional loads, most of the torsional loads in the ring are either reacted by the membranes, or countered by compression and tension in the beam flanges as a result of the curvature of the beam. A rectangular tube with a height to width aspect ratio of 3:1 was selected for the improved ring design.

Tensioning bladders made from fire hose were used in the first prototype heliostat to tension the membranes. The bladders were positioned on the outside perimeter of the ring and inflated in order to tension the membranes. Unfortunately, leaks in the bladders caused frequent decreases in membrane tension. In addition, the bladders did not provide a rigid, fixed attachment of the membranes to the ring. In the second-generation design, the membranes are tensioned with an external tool and then welded directly to the top and bottom surfaces of the rectangular ring. This type of attachment allows the membranes to provide more out-of-plane stiffness to the ring.

The first-generation mirror module included four trusses for ring support. The improved design uses five trusses, based on cost and structural considerations described in Section 4.0.

A comprehensive finite-element model of the mirror module including the ring, membranes, and support trusses has been developed. This model provides a realistic assessment of the actual stresses and resulting deformations incurred in the mirror module and is an accurate tool for the design and sizing of various components for the mirror module. The finite-element model analysis is described in Section 5.0.

2.0 DESCRIPTION OF THE IMPROVED COMMERCIAL MIRROR MODULE

A drawing of the commercial size mirror module mounted on the Peerless-Winsmith advanced low-cost drive is shown in Figure 2.0-1. The commercial mirror-module specifications are shown in Table 2.0-1. The total area of the module is 150 m^2 with a diameter of 14 meters. Tensioned stainless steel foil membranes are welded to both sides of the carbon steel ring. The ring is supported by five trusses, which radiate from a central hub. The hub is mounted on a pedestal-type drive system for purposes of tracking in the azimuth and the elevation directions. In order to compensate for changes in pressure on the front reflective membrane due to wind forces, an active focus-control system is utilized. The system consists of a LVDT mechanical position indicator that measures the position of the front membrane and a linear actuator that is attached to a pad on the rear membrane. The linear actuator modulates the position of the rear membrane in order to change the internal volume and therefore, pressure. A refocus valve is included to periodically compensate for air leaks in the mirror module. A more detailed description of each of the components is provided below.

The A500B carbon steel ring is made of rectangular tube cross-section with a height of 22.9 cm (9 in) and a width of 7.6 cm (3 in). Its wall thickness is 2.29 mm (.09 in). The dimensions of the ring were determined based on a mirror module with five truss supports and a maximum allowable deflection between supports of 4.2 mm (.165 in) under a 12-m/s (27-mph) wind load. This out-of-plane deflection corresponds to an optical slope error of .60 mrad RMS, based on the relations described in Appendix B.

The .0762-mm (.003-in) thick 304L stainless steel membranes are roll-resistance lap-seam welded from 61.0-cm (24-in) wide rolls of stock. The membranes are tensioned to a 89.6-MPa (13,000-psi) stress level. The ring is pre-compressed to 44.8 MPa (6500 psi). The membranes are then welded directly to the ring on the top and bottom surface, as shown in Figure 2.0-2. Welding of the membranes to the ring is accomplished with a roll-resistance welding head. An electrical current is passed from a copper electrode wheel on the top of the ring to a second copper electrode wheel on the bottom of the ring.

TABLE 2.0-1 COMMERCIAL HELIOSTAT SPECIFICATIONS

Heliostat Diameter	14 m	(46 ft)
Area	154.4 m ²	(1661.9 ft ²)
Reflective Area	148.85 m ²	(1602.2 ft ²)
Support Ring Material	A500B Carbon Steel	A500B Carbon Steel
Support Ring Cross Section	7.62 cm x 22.86 cm	(3 in x 9 in)
Ring Wall Thickness	0.23 cm	(0.09 in)
Ring Cross Sectional Area	13.94 cm ²	(2.16 sq in)
Ring Moment of Inertia - I _x	875.75 cm ⁴	(21.01 in ⁴)
Ring Moment of Inertia - I _y	156.92 cm ⁴	(3.77 in ⁴)
Front Membrane Material	304L Stainless Steel-Annealed	
Back Membrane Material	304L Stainless Steel-Half Hard	
Membrane Thickness	0.008 cm	(0.003 in)
Membrane Preload	6.829 nt/mm	(39 lbs/in)
Membrane Stress	89.64 m Pa	(13000 psi)
Number of Ring Supports	5 Each	5 Each
Span	7.0 m	(23 ft)
Depth of Support at Hub	0.76 m	(30 in)
Depth of Support at Outer Ring	0.305 m	12 (in)
Modulation Pad Diameter	1.83 m	(6 ft)
*Center of Gravity	56.6 cm	(22.3 in)

*Note: Distance From Front Membrane

MEMBRANE TO RING ATTACHMENT

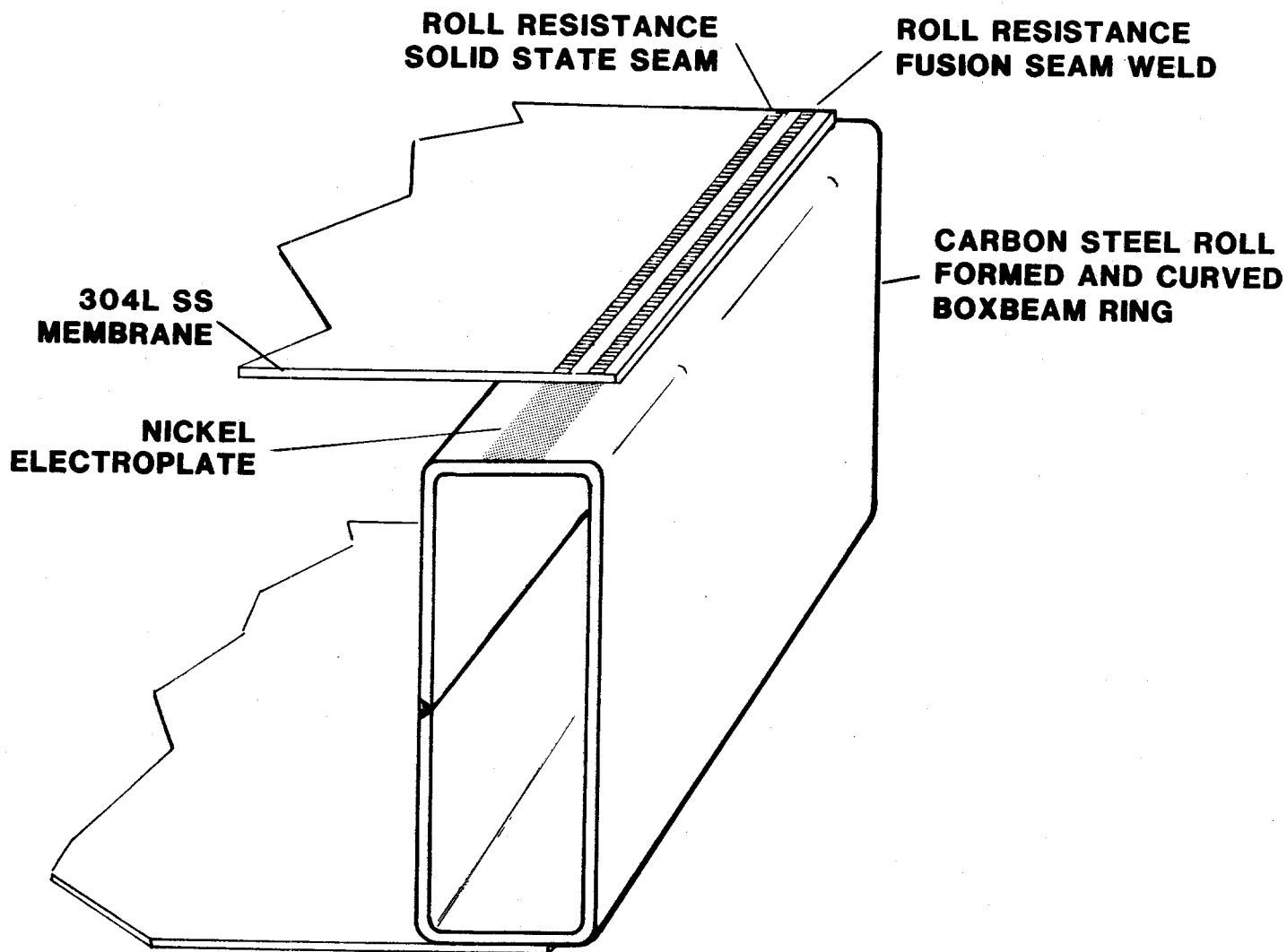


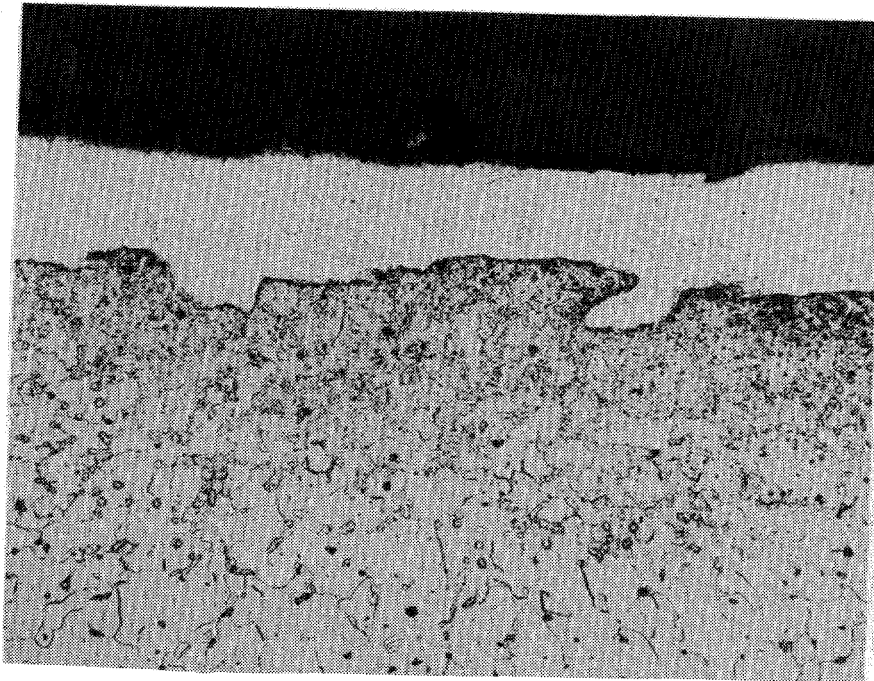
Figure 2.0-2. Membrane To Ring Attachment

The membranes are tensioned prior to welding in a manner that imparts uniform circumferential and radial stress over the surface of the membrane. The rigid attachment to the ring increases the stiffness of the overall mirror module.

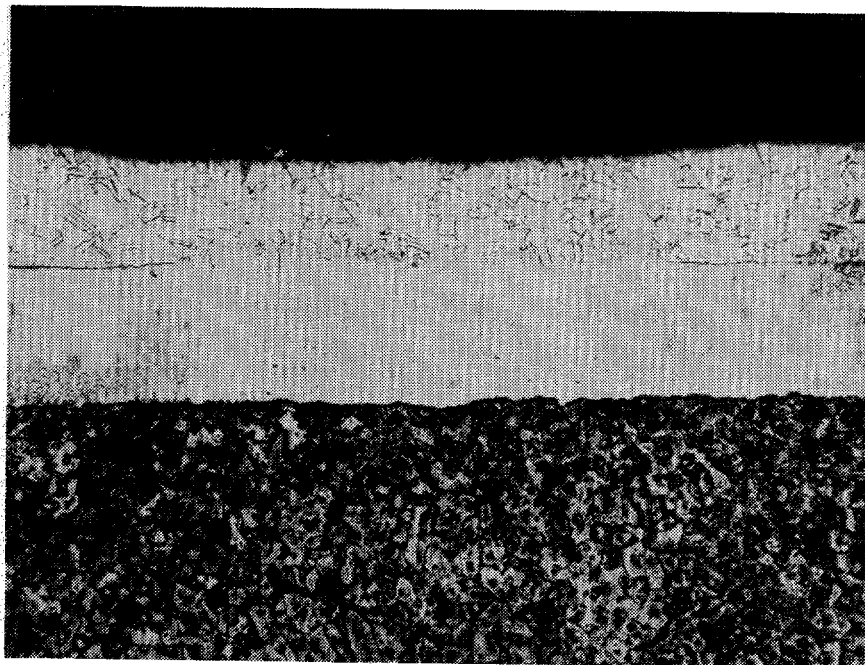
The top and bottom of the carbon steel ring are electroplated with nickel to form an interface between the stainless steel and the carbon steel. This technique, developed for welding the dissimilar metals, improves the weld ductility and resistance to corrosion by reducing the amount of carbon at the weld site and minimizes the weld pool melt-time to prevent chromium-carbide precipitation. The nickel is applied in an acid bath with a negative electrode attached to the ring. The nickel then precipitates from the acid as it is attached to the carbon-steel ring. This technique is relatively rapid, and good control over electroplate thickness is achievable.

Metallurgical photographs of membrane-to-ring welds are shown in Figure 2.0-3. A stainless steel membrane welded directly to the carbon steel ring is shown in the top photo. Rockwell hardness tests showed a very hard but brittle fusion area for this weld due to chromium-carbide precipitation. In the lower photo, a 3-mil layer of nickel electroplate is used as an interface layer between the stainless steel foil (top) and the carbon steel (bottom). The hardness of the fusion area with the nickel was considerably lower, indicating a more ductile weld. Peel tests of the nickel electroplate showed good adhesion to the carbon steel surface. This type of weld should be fatigue and corrosion resistant. A low-temperature solid-state seam weld is first used to attach the membranes to the ring while the membrane is under tension in a tensioning fixture. A higher temperature fusion seam weld is accomplished outside of the first weld once the membrane tension has been reduced.

ECP-300 silverized polymer reflective film is laminated to the stainless steel foil to form the reflective surface of the mirror module. The reflective film is applied in strips slightly narrower than the width of the stainless steel strips. Therefore, the reflective film is not laminated over the overlapping welds of the membrane. A dry lamination process is used to apply the film to the stainless steel foil prior to the membrane welding process. Once membrane welding has been completed, an ECP 244 aluminized acrylic reflective tape is applied over the welds and over the two edges of the reflective film adjacent



3 mil 304 SS to A500 Carbon Steel - 200X
Rockwell Hardness : 304 SS = R_B90 A500 = R_B82 Fusion = R_c 30-35



3 mil 304 SS to 3 mil Nickel Electroplate on A500 Carbon Steel

Figure 2.0-3. Ring To Membrane Weld Cross-Sections

to the welds. Finally, a sealant is applied at each edge of the tape. This lamination process may be revised as we learn more about the causes of delamination of the silvered polymer film in this application.

Five trusses radiating from a central hub are used to support the mirror module at the perimeter. A three-dimensional truss design was selected that has significant torsional and in-plane stiffness in addition to out-of-plane stiffness. This eliminates the need for inter-truss diagonal cables for bracing and maintains the ring planarity at the attachment points. The truss has a triangular cross-section with round tubing at the three corners and bent wire diagonal webbing between the three tubes. The trusses are tapered from the hub to the ring with a depth of .76 m (30 in) at the hub, and a depth of .305 m (12 in) at the ring.

A drawing of the truss design is shown in Figure 2.0-4. The width of the truss at the base is 61.0 cm (24 in). This aspect ratio of 76.2 cm by 61.0 cm (30 in by 24 in) provides increased stiffness in the out-of-plane direction as compared to a truss with an equilateral triangular cross section. The truss is mounted to the mirror module with a base of the triangle toward the back membrane. Steel tubing of 7.62-cm (3-in) diameter is used at the two corners forming the base of the triangle, and 10.2-cm (4-in)-diameter tubing is used at the top of the triangle. Together, the two 7.62-cm (3-in)-diameter tubes have nearly an equivalent cross sectional area as compared to the single 10.2-cm (4-in)-diameter tube. This is necessary to provide equal strength to the truss when the tubes are put in compression or tension due to out-of-plane forces. Tubing was selected as opposed to other types of cross sections due to the lower cost of manufacturing. Steel wire with a diameter of 1.27 cm ($\frac{1}{2}$ inch) is used for the webbing of the truss. Low-cost materials, ease of automated manufacture, and reduced component counts made the concept both cost effective and clean looking.

The method of attaching the truss to the ring is shown in Figure 2.0-5. A mounting trunnion is welded to a doubler plate, which is in turn welded to the ring at five locations. Truss mounting gussets are attached to each of the two 7.62-cm (3-in)-diameter tube truss ends. A pin is used to attach the mounting trunnion to the truss mounting gussets. This type of attachment allows rotation of the ring about the mounting pin, but is rigid in rotation and translation in

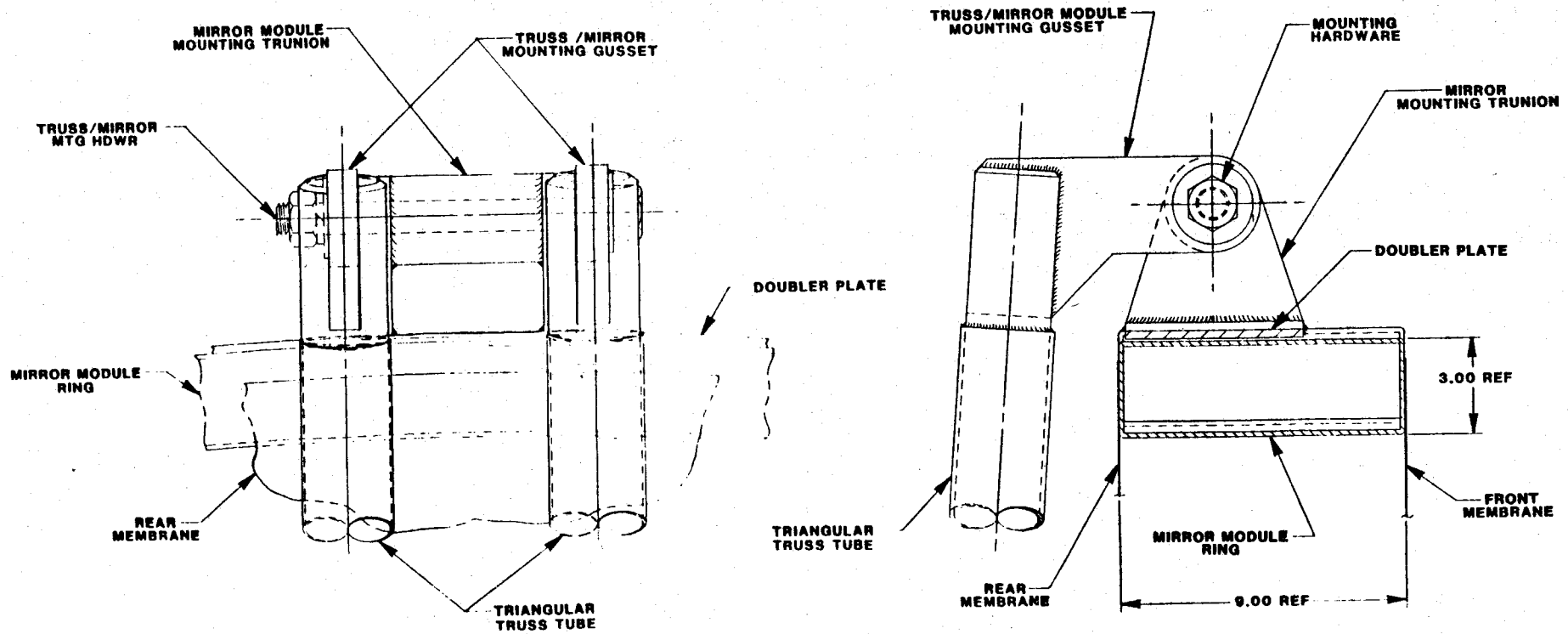


Figure 2.0-5. Mirror Module Mounting Trunion

all other directions. The center line of the mounting pin is located one-third of the distance from the back side of the ring. This mounting location has been shown to impart the least optical error due to distortion of the membrane and ring under wind loading. This analysis is discussed further in Section 5.0, Structural Analysis of the Commercial Mirror Module.

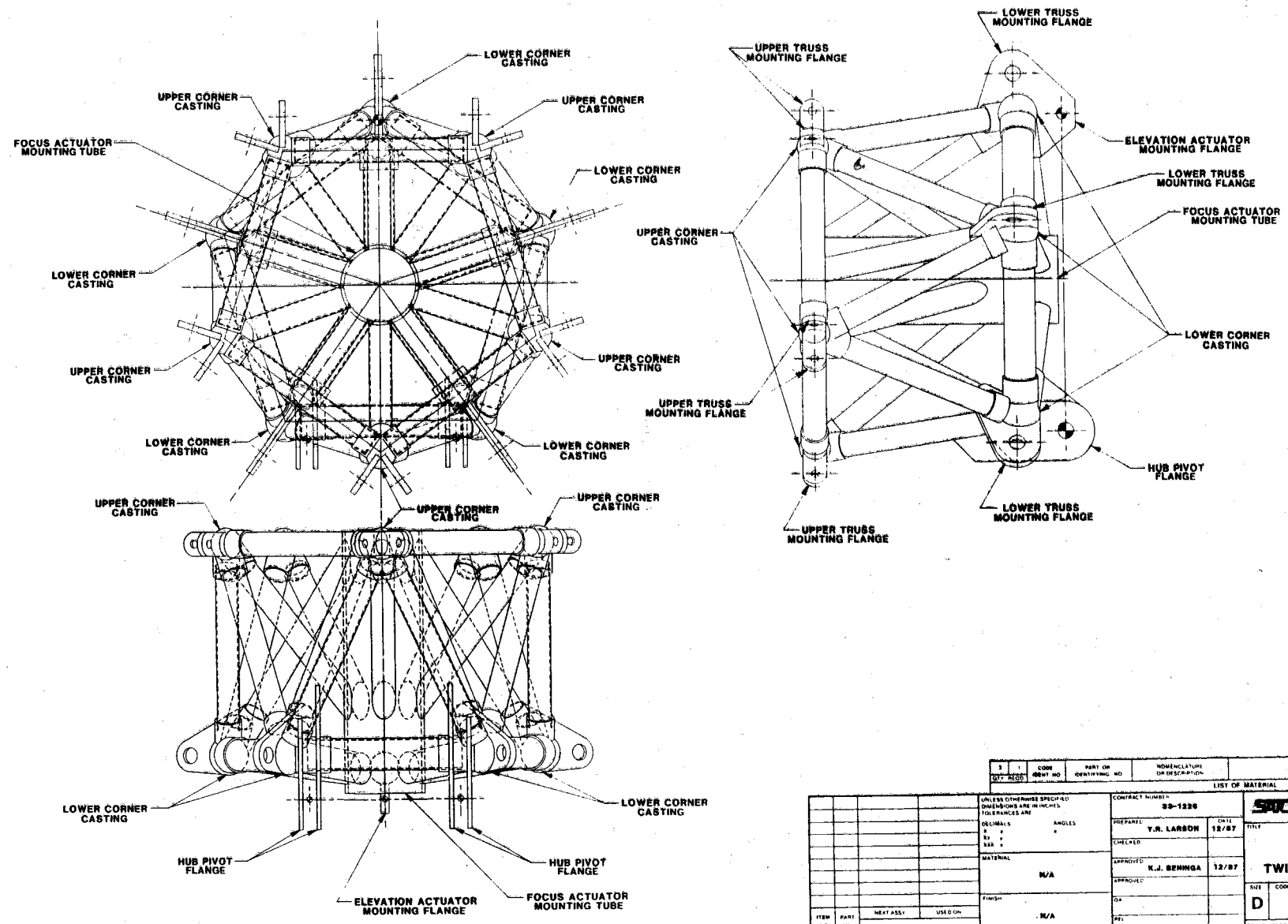
The truss mounting hub is shown in Figure 2.0-6. This central hub is used for mounting the trusses and subsequently mounting the mirror module to the drive system. This type of hub is termed a twisted tubular pentagon. As shown in the drawing, two tubular pentagons form the main structure of the hub at the top and bottom. The bottom pentagon is rotated 36° from the top pentagon. Diagonal tubes are used to form the connection between the top pentagon and the bottom pentagon. The diagonal tubes also support the center focus actuator mounting tube. Truss mounting flanges are located at each corner of both the top and bottom pentagon. The geometry of the hub is such that the three corners of the truss base can mount directly to three corners of the hub, as shown in Figure 2.0-6. A mounting flange is provided for each of the three corners for all five trusses. Castings are used to facilitate assembly of the hub and reduce fabrication time. Two configurations of castings are required to form the corners of the twisted tubular pentagonal hub.

Pivot flanges for the drive system are provided on the hub to attach to the elevation drive pivot. Another flange is provided for attaching the elevation jack screw rod end to the hub. The design shown results in a very stiff hub. Since high moments are imparted from the base of the trusses to the hub and these moments must be transferred efficiently to the drive pedestal, the hub is a critical component in maintaining the stiffness and rigidity of the mirror module. Modulation of the rear membrane to accomplish focus control is accomplished with the use of a linear actuator connected to a 1.83-m (6 ft)-diameter steel pad that is attached to the center of the rear membrane. The pad distributes the stress caused by active modulation of the membrane. Two steel pads are used to sandwich the rear membrane. The inner pad also has a ring attached for the purpose of defocusing the front membrane. A plenum pressure equalization valve is mounted on the outside pad.

A weight break-down of the commercial mirror module is shown in Table 2.0-2. The total weight of the mirror module is 2072 kg (4559 lbs), which

MODEL		REVISIONS	
EFFECTIVITY	DATE	DESCRIPTION	DATE

18



QTY	UNIT	EDGE VIEW NO.	PART OR IDENTIFYING NO.	NOMENCLATURE OR DESCRIPTION	MATERIAL AND SPECIFICATION	ITEM NO.

LIST OF MATERIAL		CONTRACT NUMBER	
		33-1226	

PREPARED	DATE	TITLE
Y.R. LARSON	12/87	HUB, TRUSS MOUNTING COMMERCIAL TWISTED TUBULAR PENTAGON

APPROVED	DATE	REV
K.J. BEMINGA	12/87	

ITEM NO.	PART NO.	WEIGHT	USED ON	FINISH
				N/A

SCALE	CODE	DATE	DATE
D		999D121087-001	

PROJECT	SHEET	OF
	1	1

Figure 2.0-6. Commercial Truss Mounting Hub

corresponds to an area density of 13.8 kg per m² (2.82 lbs per ft²). The area density of SAIC's first commercial membrane heliostat design (1986) was 10.7 kg/m² (2.2 lb/ft²). The increase in weight is due to increased ring and support structure strength, and a more detailed component weight accounting. A large portion of the mirror module's weight is attributable to the hub and truss support structure. This fact indicates that an alternate method of supporting the ring may provide a lower weight and cost alternative to the pedestal-type drive.

TABLE 2.0-2 STRETCHED MEMBRANE MIRROR MODULE WEIGHT

DESCRIPTION	KILOGRAMS	POUNDS
FRONT MEMBRANE	94.2	207.7
RING FRAME	491.6	1083.8
AMPLIFIER	.5	1.0
POWER SUPPLY	.9	2.0
BACK MEMBRANE	94.2	207.7
REFLECTIVE FILM	21.4	47.2
MIRROR MOUNTING TRUNION	47.0	103.5
TRUSS/MIRROR MTG GUSSET	46.5	102.6
DOUBLER PLATE	17.0	37.5
MIRROR MOUNTING HARDWARE	7.3	16.0
TRUSS TUBES - 3 INCH	249.0	548.9
TRUSS TUBES - 4 INCH	196.1	432.4
TRUSS WIRE - 1/2 INCH	344.8	760.1
HUB TUBE - 3 INCH	85.3	188.0
HUB TUBE - 4 INCH	27.9	61.4
HUB TUBE - 11 INCH	35.0	77.1
HUB TOP PENTAGON JOINT	48.4	106.6
HUB BOTTOM PENTAGON JOINT	76.5	168.7
HUB LIFT FLANGE	4.6	10.2
HUB OUTER PIVOT FLANGE	13.1	28.8
HUB INNER PIVOT FLANGE	9.4	20.6
FOCUS PAD INNER HONEYCOMB SANDWICH	10.0	22.1
FOCUS PAD OUTEST HONEYCOMB SANDWICH	10.0	22.1
FOCUS PAD INNER RING	11.5	25.4
FOCUS PAD OUTER RING	8.1	17.8
INNER PAD BOLT PLATE	22.3	49.2
OUTER PAD BOLT PLATE	22.3	49.2
ACTUATOR	15.9	35.0
ACTUATOR MTG BLOCK	1.2	2.6
ACTUATOR MTG GUSSET	.84	1.8
ACTUATOR STIFFENING GUSSET	9.1	20.1
DAMPER VALVE & FLANGE	3.2	7.0
VALVE MTG SPOOL	5.6	12.3
PINS/TRUSS BASE TO HUB	2.9	6.4
CONTROL BOX	34.0	75.0
TOTAL WEIGHT:	2072	4559

3.0 DESIGN CRITERIA FOR THE MIRROR MODULE

The major goals of the design improvement program were to improve the optical quality, reliability, and fabrication processes for the advanced mirror module. In order to do this close attention had to be paid to the planarity of the ring while considering both manufacturing tolerances and out-of-plane deflection under wind load. To control the out-of-plane deflection of the ring, the out-of-plane stiffness per unit weight had to be optimized. This stiffness is increased by the flange effects of the tensioned membranes attached to the ring.

In order to quantify the allowable optical errors attributable to various components of the mirror module, a set of design criteria for the mirror module was established before proceeding with the design. A summary of the design criteria for the commercial-size mirror module is shown in Table 3.0-1. The complete design criteria document is included as Appendix A.

A total optical error budget was first established based on optical requirements of heliostats for central receiver applications. The maximum allowable error due to each of the individual error sources was then allocated. The allowable errors shown were selected based on contact with manufacturers of rolled steel rings to determine achievable tolerances and on analysis of the effects of out-of-plane deformation of the ring on optical quality. This information was subsequently used with a finite element model to size various components of the system. The design criteria were also supplied to vendors to define allowable tolerances on heliostat ring manufacture and were used in the selection of the optimum number of support trusses for the module. Other considerations in ring selection were suitability for in-plane rigid attachment of membranes, manufacturability, and adequate in-plane and torsional stability.

To determine the relationship between out-of-plane deformations and optical error, an equation that relates the number of ring supports and the maximum ring deflection to optical error was utilized. The simplest form of this equation is shown below.

Table 3.0-1 Design Criteria For The Mirror Module

TOLERANCES

Total optical error budget for the mirror module structure:

Commercial Design - 1.0 mRad RMS Slope Error
 Prototype Design - 1.2 mRad

The allowable component error breakdown for 12.1 m/s (27 mph) wind is as follows:

	<u>Commercial Design</u>		<u>Prototype Design</u>	
	<u>Slope</u>	<u>Equivalent</u>	<u>Slope</u>	<u>Equivalent</u>
	<u>Error</u>	<u>Deflection</u>	<u>Error</u>	<u>Deflection</u>
Truss-Hub Assembly Tip Deflection	0 mRad	(.44 inch)	0 mRad	(.25 inch)
Maximum Deflection Variation Between Any Two Truss Tips	0.16 mRad	(.044 inch)	0.16 mRad	(.025 inch)
Amplified Ring Out-of-Plane Manufacturing Error (N = 2)	0.227 mRad	(.0885 inch)	0.401 mRad	(.0885 inch)
(Approximate Non-Amplified)		(.0625 inch)		(.0625 inch)
Ring Out-of-Round Error (Radius Tolerance)	.01 mRad	(.44 inch)	.01 mRad	(.25 inch)
Wind Load Deflection Error (N = 5) (5 Supports)	.60 mRad	(.148 inch)	.60 mRad	(.083 inch)

Survival Wind Load 22.4 m/s (50 mph) Maximum Stress:

- Limit Stress to 60% Yield Stress
- Limit Compressive Stress in Web to $\frac{1}{2}$ The Local Buckling Stress
- Limit Membrane Tension to Less Than $\frac{1}{2}$ Out-Of-Plane Ring Buckling Critical Tension

$$\beta = \frac{D}{R} \sqrt{N}$$

where, B = slope error (radians)

D = maximum ring deflection (mm)

N = number of trusses

R = ring radius (meters)

The derivation of this equation is shown in Appendix B. A more precise estimate of the optical error can be calculated by determining the ring's out-of-plane displacements around the perimeter from the finite element model, then fitting an equation to the data. The equation is then used with another form of the above equation to determine the overall slope error. Note that the error calculated does not include the effect of reflective surface specularity, but only the effect of ring in-plane and out-of-plane deformations on surface slope error.

By using an iterative process with the finite element model and the optical model, the ring's dimensions and manufacturing tolerances that meet the design criteria without the use of excess material or unnecessarily tight manufacturing tolerances are determined.

The mirror module must be capable of providing the optical accuracy shown in Table 3.0-1, up to a wind speed of 12.1 m/s (27 mph). From 12.1 m/s to 22.4m/s (27 to 50 mph), the mirror module must be able to survive (without operation) in any orientation. The mirror module must survive a 40.5 m/s (90 mph) wind in the stow position. Ultimately, from the design process, it was found that the load case that governed the design of the ring and membranes was the strength criterion at 22.4 m/s (50 mph) wind, rather than the optical accuracy (stiffness) criterion at 12.1 m/s (27 mph) wind. Therefore, the design is strength limited so that the stiffness of the mirror module is actually higher than required to meet the optical design criterion.

4.0 TRADE STUDIES FOR THE COMMERCIAL MIRROR MODULE

Trade studies were performed in several key areas in order to determine the design changes necessary for second-generation as compared to the first-generation mirror modules. A summary of these trade studies is given in this section.

4.1 Material Selection

Materials for the membrane other than the stainless steels were not considered because stainless steel was specifically identified in the statement of work (SOW), and because good success was achieved with stainless in the first-generation design effort.

The factors considered in selecting the stainless steel type, hardness, and thickness were

- 1) Suitability for prestressing to 89.6 MPa (13,000 psi),
- 2) Weldability of membrane material,
- 3) Handleability of membrane material,
- 4) Flatness of manufactured coil stock,
- 5) Adequate yield strength to survive the 22.4 m/s (50 mph) wind loading condition in any orientation,
- 6) Adequate margin between yield strength and ultimate strength,
- 7) Cost.

The membrane material options considered were

- 1) Type 304 stainless steel-annealed, .0762-mm (.003-inch) thickness, yield strength equal to 275.8 MPa (40 ksi),
- 2) Type 304L stainless steel-annealed, .0762-mm (.003-inch) thickness, yield strength equal to 275.8 MPa (40 ksi),
- 3) Type 304L stainless steel-annealed, .1270-mm (.005-inch) thickness, yield strength equal to 275.8 MPa (40 ksi),
- 4) Type 304L stainless steel-half-hard, .0762-mm (.003-inch) thickness, yield strength equal to 827.4 MPa (120 ksi).

Ultimately, 304L annealed stainless steel with a thickness of .0762 mm (.003 in) was selected for the front membrane, and 304L half-hard stainless steel with a thickness of .0762 mm (.003 in) was selected for the back membrane. The "L"

designation in the stainless steel type signifies a low carbon content. The low-carbon stainless steel was preferred in order to reduce the potential for chromium-carbide precipitation in both the membrane-to-membrane seam welds and the membrane-to-ring attachment welds. The cost of the low-carbon stainless steel was no more than for the standard stainless steel. The half-hardened stainless steel for the back membrane was selected in order to avoid yielding around the focus actuator pad where high stress concentrations can occur. Welding tests were done with all the materials listed above in order to ascertain that good quality welds were achievable. The use of the .1720-mm (.005-in thick) annealed stainless steel for both the front and the back membrane was also considered as an option to avoid yielding in the back membrane. This thickness of stainless steel showed some increase in handleability and avoidance of creases. However, the .0762-mm (.003-in) thickness stainless steel was selected based on the significantly lower cost of this option.

Recently, our stainless steel supplier has identified some low alloy Series 200 stainless steels that should have the same characteristics as Type 304 for this application and reduce cost by up to 25%. We are currently experimenting with this material for future applications.

Manufacturers of stainless steel foil were surveyed to locate a supplier with a capability to flatten the stainless coil stock before delivery. Flattening is necessary to eliminate the "lasagna noodle" wavy edges that are found on most stainless steel foils. One manufacturer, Allegheny Ludlum, recently installed a state-of-the-art flattening process for foil stock in which a series of rollers and tensioning devices flatten the foil. This stainless steel can also be ordered with various levels of surface finish.

The materials considered for fabrication of the ring for the mirror module were

- 1) A500 carbon steel,
- 2) A500-B carbon steel,
- 3) stainless steel,
- 4) aluminum,
- 5) stainless steel clad carbon steel.

The A500 carbon steel was the lowest cost option, but the A500-B carbon steel had a significantly higher yield strength with only a little increase in cost.

Although stainless steel would be the preferred ring material from a fabrication point of view due to its membrane welding compatibility and matching thermal expansion coefficient, the cost of stainless steel is prohibitive for this application. Aluminum was rejected due to its non-compatibility with the welding process and its much higher thermal expansion coefficient as compared to the stainless steel membranes. The stainless-steel-clad carbon steel first appeared to be an attractive option, but it was discovered that the technology for cladding and rolling in the beam sizes required for the commercial size design is not currently available. The cladding process is currently used for structural shapes such as those used for handrails and decorative structures. Development of cladding technology for large structural shapes may make this an attractive option in the future.

Based on cost, weldability, and strength considerations, A500-B carbon steel was selected as the preferred material for fabrication of the ring. This material selection resulted in a low ring cost, but required development of welding technology dissimilar metals for and investigation of the effects of the different thermal expansion coefficients of the membrane and ring. These studies were carried out as part of this program and are reflected in the final design of the mirror module.

4.2 Selection of the Ring Type

Considerations in selecting the type of cross-section for the ring included:

- 1) maximizing out-of-plane stiffness per unit weight,
- 2) providing a surface for in-plane rigid attachment of the membranes,
- 3) using conventional beam forming and ring rolling techniques to achieve the required tolerance,
- 4) providing adequate in-plane buckling and torsional stability.

As shown in Appendix A, additional criteria included limiting the tensile stress to one-third of the yield stress and limiting the compressive stress in the web to one-half the local buckling stress.

The type of ring cross-sections considered were square tube, rectangular tube, I-beam, channel, round tube, and nested channels. In order to form a basis

of comparison, a unit of measurement termed specific stiffness (stiffness per unit weight) was used to compare the in-plane, out-of-plane, and torsional stiffness of these various shapes. A summary of this comparison is shown in Table 4.2-1. The values shown in the table are for standard structural shapes with approximately equivalent cross sectional areas. The wall thicknesses available in these standard shapes vary with the type of cross section. The minimal wall thickness available was used for all shapes in order to minimize the ring weight and cost, and maximize the membrane spacing, which increases module stiffness. The manufacturer's minimum wall thicknesses are based on avoidance of local wall buckling for beams in compression. Therefore, the standard wall thicknesses were used as the basis of comparison rather than a constant wall thickness for all shapes. The effects of this comparison can be seen by comparing the out-of-plane specific stiffness of a rectangular tube with an aspect ratio of three-to-one to the specific stiffness for a channel. Even though the channel shape has an inherently higher out-of-plane moment of inertia, the manufacturers recommend a thicker wall for a channel to avoid local wall buckling as compared to a rectangular tube.

The I-beam shape had the highest out-of-plane specific stiffness, with a value of 3.52. However, I-beams cannot be formed from flat coiled stock at the field assembly site. Also, the very low torsional stiffness of I-beams implies that resistance to torsional loads must be carried almost completely by the membranes. A channel cross section and a rectangular tube with an aspect ratio of three-to-one were chosen as the two best candidates for the ring design. The rectangular tube was ultimately chosen because of concerns about the buckling stability of the channel flanges when the membrane tension was applied.

4.3 Effects of Thermal Expansion

The stainless steel membrane material has a coefficient of thermal expansion of 16.6×10^{-6} cm/cm-°C (9.2×10^{-6} in/in-°F), as compared with the carbon steel ring material with a coefficient of 14.8×10^{-6} cm/cm-°C (8.2×10^{-6} in/in-°F). The higher coefficient of thermal expansion for the stainless steel results in an increase in membrane tension as the operating ambient temperature decreases

Table 4.2-1. Ring Cross-Section Comparison - Specific Stiffness
(Stiffness/Unit Weight)

CROSS-SECTION SHAPE	OUT-OF-PLANE	IN-PLANE	TORSIONAL
	$\frac{I_x E}{C_x \rho A} \times 10^{-8}$	$\frac{I_y E}{C_y \rho A} \times 10^{-8}$	$\frac{J E}{C_T \rho A} \times 10^{-8}$
* SQUARE TUBE	2.67	2.67	4.09
* RECTANGULAR TUBE			
ASPECT RATIO 1.5:1	2.81	2.23	2.13
2.0:1	2.92	1.80	1.64
3.0:1	3.00	1.60	.982
6.0:1	3.14	.905	.291
** I-BEAM	3.52	.399	.008
** CHANNEL	2.84	.238	.013
*** ROUND TUBE (SAIC)	2.61	2.61	5.21
*** ALUMINUM RECTANGLE (SKI)	2.80	1.24	.577

- * BASED UPON MINIMUM AVAILABLE WALL THICKNESS OF .188 INCHES
- ** BASED ON MINIMUM WALL THICKNESSES AVAILABLE
- *** DIMENSIONS FROM ORIGINAL COMMERCIAL RING DESIGNS

from the manufacturing temperature and in a reduction in membrane tension as the ambient temperature increases above the manufacturing temperature.

A finite element model was used early in the program to determine the effects of the dissimilar thermal expansion coefficients. The selected minimum operating tension of the membranes was 68.9 MPa (10,000 psi) at the maximum specified operating temperature of 50°C (122°F). The required membrane stress at the time of fabrication (assuming a temperature of 21°C (70°F)) was then determined to be 89.6 MPa (13,000 psi). At the minimum specified operating temperature of -7.8°C (18°F), the membrane tension is increased to 103.42 MPa (15,000 psi). These values were calculated by using the thermal stress option of the finite element model.

The results of the analyses are shown in Figures 4.3-1 and 4.3-2. The variation of the membrane tension as a function of temperature is shown in Figure 4.3-1. The variation in ring compressive stress as a function of ambient temperature is shown in Figure 4.3-2. The variation in ring and membrane stresses as a function of ambient temperature is sufficiently small so that the variation in thermal expansion coefficients is not a problem. The selection of a membrane's operating stress is somewhat arbitrary anyway, and adequate performance can be achieved over a fairly wide range of operating stress. The membrane's operating stress selected need only be low enough to avoid membrane failure and ring buckling under survival wind loads, and high enough to achieve the desired optical quality.

4.4 Trade Study of Ring Support Points

In the first development program for a stretched-membrane mirror module SAIC selected four truss supports radiating from the central hub to support the ring at equidistant points. Solar Kinetics, Inc., elected to use six trusses to support the ring. In the mirror module design improvement program, SAIC performed a trade study to determine the optimum number of support points for the ring. The problem was approached from two different points of view. The first was to determine the total weight and cost of the mirror module for designs utilizing three through six support points. The second approach was to study the effects of the number of support points on the ring deformation mode shape.

THERMAL RESPONSE OF HELIOSTAT MEMBRANE

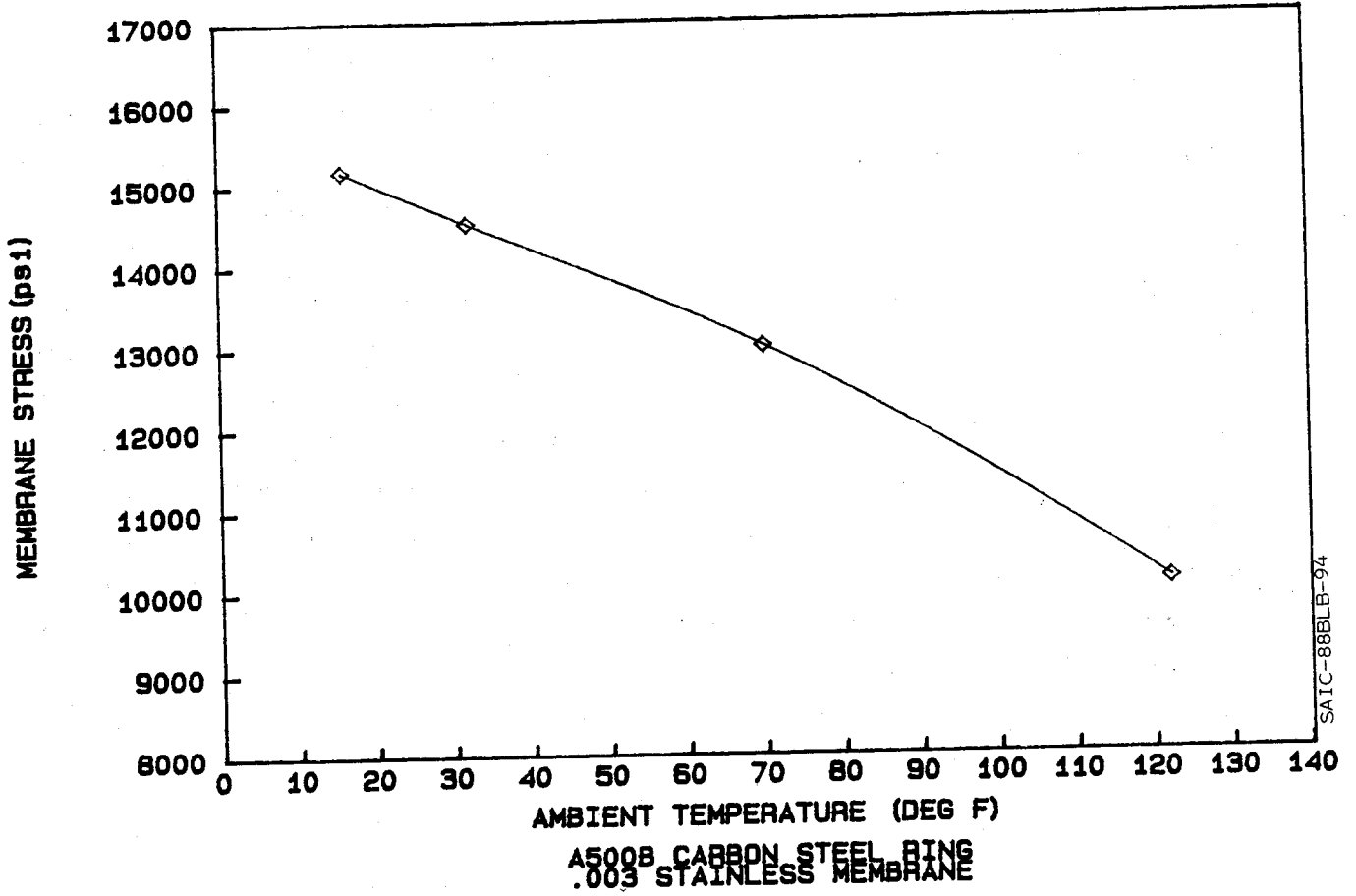


Figure 4.3-1. Thermal Response of Heliostat Membrane

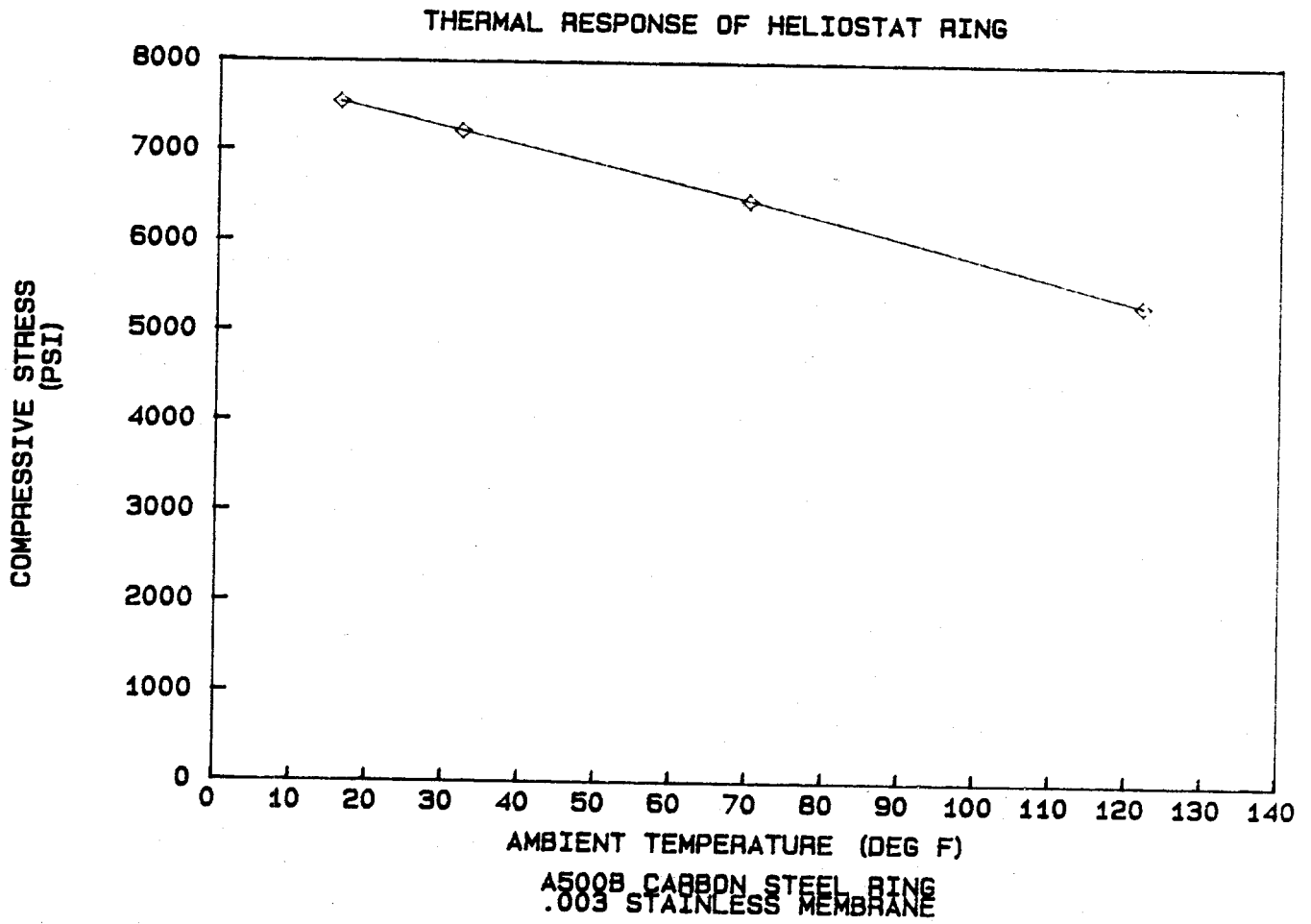


Figure 4.3-2. Thermal Response of Heliostat Ring

To determine the optimum number of trusses from a cost standpoint, preliminary designs for the mirror module were generated with three, four, five, and six truss supports. As a basis of comparison, the optical error under a 12.1 m/s (27 mph) wind load was maintained equal for all four cases. A ring was chosen for each design by determining the maximum allowable ring deflection for each case using the method outlined in Appendix B to calculate the relationship between ring deflection, number of supports, and optical slope error. Truss sizes were selected from a two-dimensional truss design catalog supplied by a truss manufacturer. The truss tip deflection was held equal for all four cases. Later in the program a custom triangular tapered truss was incorporated in the final design.

The total weight of the ring, trusses, and central hub for each of the four cases is plotted in Figure 4.4-1. As shown, the lowest weight mirror module used the design incorporating six support trusses. The total cost of material and labor for fabricating the ring, trusses, and hub for each case is shown in Figure 4.4-2. This is not necessarily the lowest cost design. The five and six support truss designs showed nearly equal costs in this analysis. This trend occurred because of the increased cost of fabricating six trusses instead of five, and of fabricating a more complex hub structure.

As stated earlier, the second approach to determining the optimum number of support trusses involved determining the ring deflection mode shape under wind loading for various numbers of trusses. The mode shape refers to the number of high points in the deflected ring shape. For example, a mode shape of $N=2$ is the familiar "potato-chip" shape. The objective in designing mirror modules is to limit the major mode shape to as high a value as possible. The minimum membrane tension at which ring buckling can occur increases dramatically with the mode shape number. The minimum mode shape number for a given number of trusses is determined by the integer values by which the number of trusses is divisible. For example, if the number of trusses equals six, a mode shape of $N=2$ and $N=3$ is possible. (The mode shape of $N=1$ is simply a rotation of the entire in-plane ring and does not affect the buckling calculations.)

Based on the above analysis, five trusses were selected for the support of the mirror module. Because five is a prime number, the minimum major mode shape

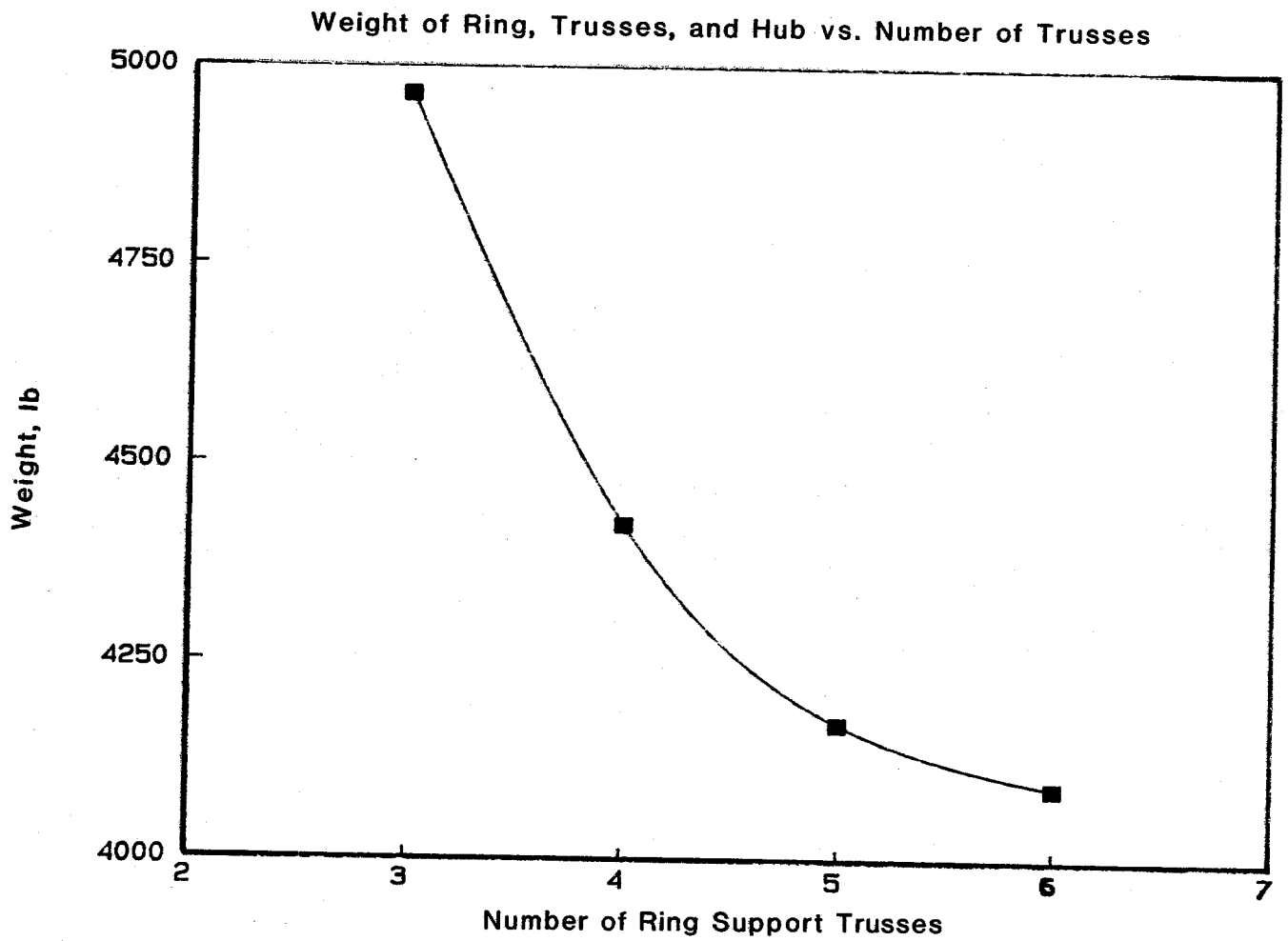


Figure 4.4-1. Weight of Ring, Trusses, and Hub Versus Number of Trusses

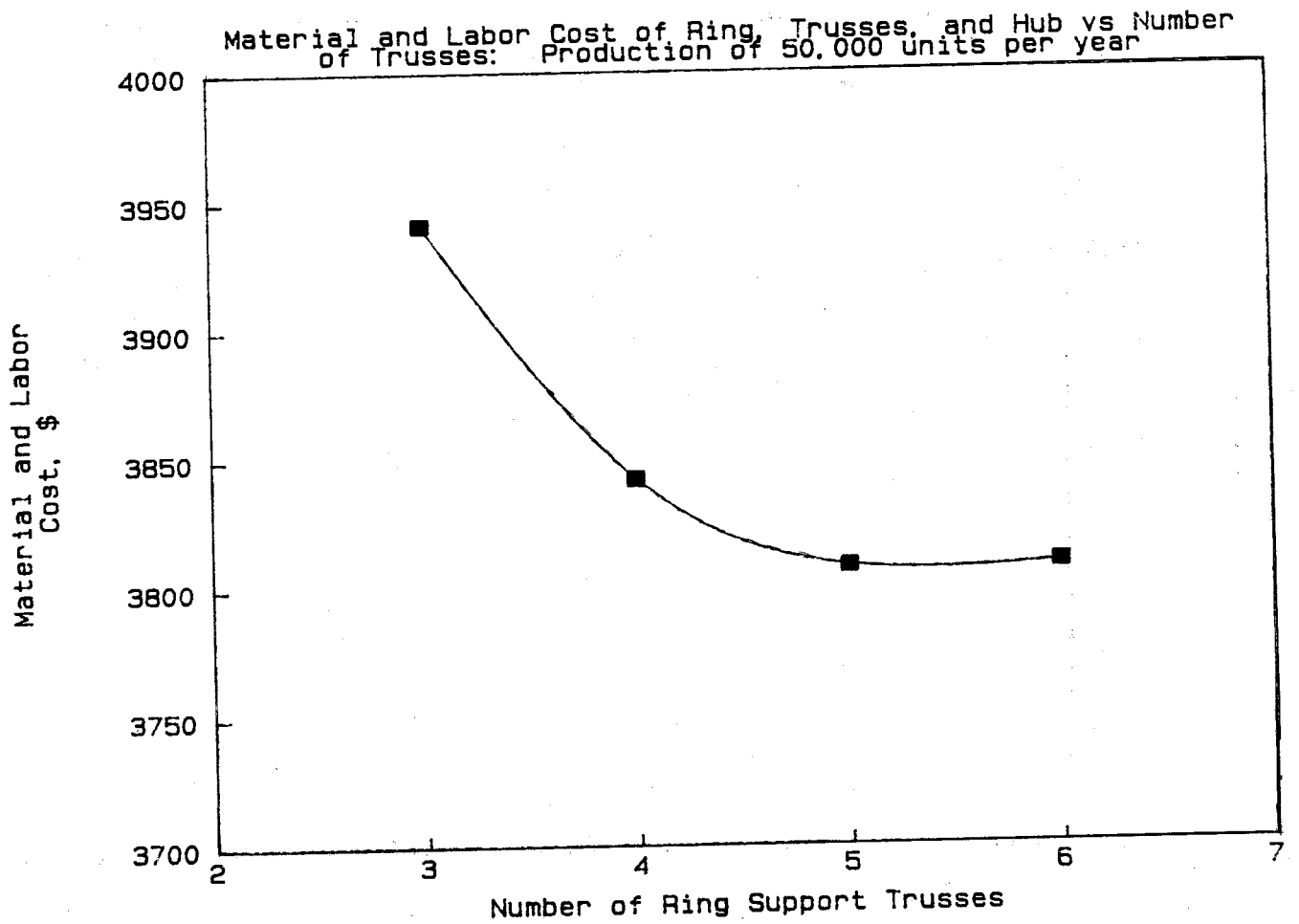


Figure 4.4-2. Material and Labor Cost of Ring, Trusses, and Hub Versus Number of Trusses

possible for a wind-deflected ring is $N=5$. The membrane tension at which ring buckling can occur with an $N=5$ mode shape is quite high, (89.3 kN/m, 510 lb/in). Therefore, the possibility of ring buckling is reduced by the use of five trusses. (See Section 5.5 for further discussion of ring buckling.) In addition, as shown earlier, there is no cost advantage in using more than five trusses.

5.0 STRUCTURAL ANALYSIS OF THE COMMERCIAL MIRROR MODULE

Structural analysis of the mirror module was performed using the personal-computer-based finite-element analysis system, Supersap, by ALGOR Interactive Systems. Figure 5.0-1 shows the finite-element model of the mirror module. The complete mirror module system including the stainless steel membranes, support ring, and trusses was modeled. Finite-element analysis results were validated using classical analytical methods. Large deflection results obtained from ALGOR Supersap were also validated using NASTRAN, a fully non-linear finite-element analysis system run on a DEC VAX computer. Out-of-plane and local wall buckling analysis of the support ring was performed using analytical methods.

The performance requirements (Appendix A) state that the mirror module must maintain focus under 12-m/s (27-mph) wind, and maintain structural integrity in a non-operational state at any orientation in a 22-m/s (50-mph) wind. Survival in the horizontal stow position in a 40-m/s (90-mph) wind is also required. The worst loading from a structural and operational standpoint occurs with the wind perpendicular to the membrane surface and the front membrane downwind. Analyses were performed with this wind loading applied to examine optical performance under 12-m/s (27-mph) wind and structural integrity under 22-m/s (50-mph) wind. The results of these analyses are summarized in Table 5.0-1.

5.1 Description of the Wind Load Model

In order to properly analyze the system and design so as to avoid failure, a worst case load scenario was developed. It was determined that the worst wind loading condition would occur with the heliostat in the vertical position and with the air flow direction perpendicular to the membrane surface. A wind velocity profile was then determined from the following relation (from Appendix A):

$$V_H = V_1(H/H_1)^{0.15}$$

where, H_1 = Reference Height = 9.1 m (30 ft)

V_1 = Reference Wind Velocity

H = Local Height

V_H = Local Wind Velocity

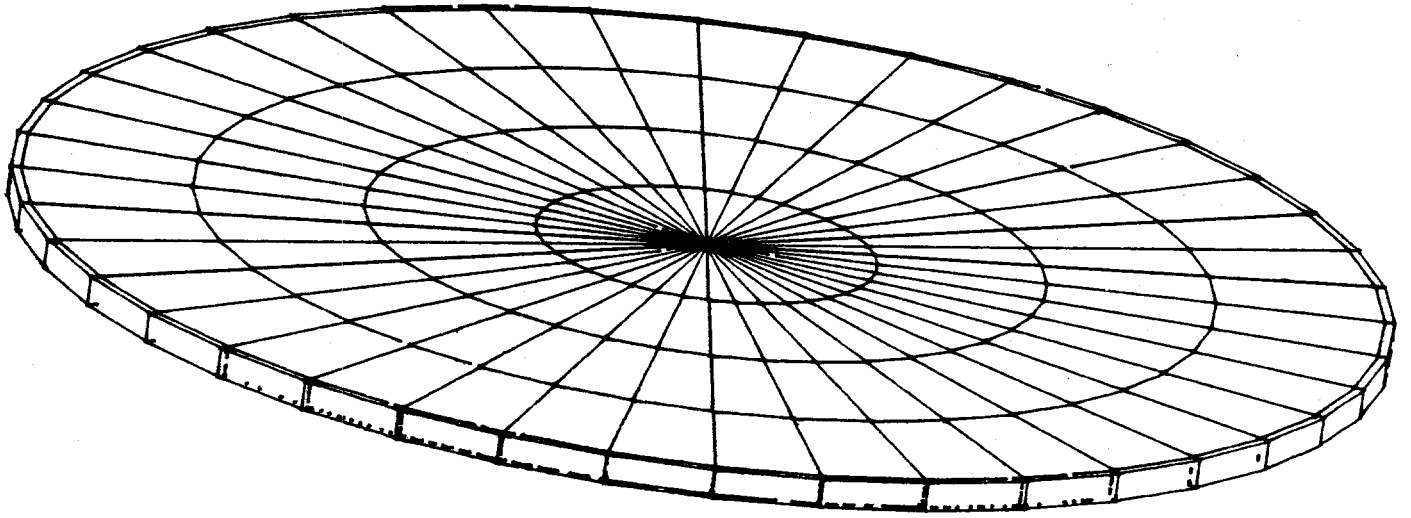


Figure 5.0-1. Mirror Module Finite Element Model

Table 5.0-1. Analysis Results for the Commercial Design

●	OPERATING CONDITION: 27 MPH WIND	
-	MAXIMUM RING DEFLECTION BETWEEN TRUSS SUPPORTS	0.089 IN.
-	MAXIMUM RING STRESS	18995 PSI
-	MAXIMUM OUT-OF-PLANE TRUSS TIP DEFLECTION	0.384 IN
-	MINIMUM OUT-OF-PLANE TRUSS TIP DEFLECTION	0.265 IN
-	MAXIMUM DEFLECTION VARIATION BETWEEN ANY TWO TRUSS TIPS	0.119 IN
-	MAXIMUM FRONT MEMBRANE STRESS	19141 PSI
-	MINIMUM FRONT MEMBRANE STRESS	13000 PSI
-	MAXIMUM REAR MEMBRANE STRESS (OPERATION AT 120°F)	71600 PSI
●	SURVIVAL CONDITION: 50 MPH WIND	
-	MAXIMUM RING DEFLECTION BETWEEN TRUSS SUPPORTS	0.216 IN
-	MAXIMUM RING STRESS	26373 PSI
-	MAXIMUM OUT-OF-PLANE TRUSS TIP DEFLECTION	1.29 IN
-	MAXIMUM TRUSS STRESS	24050 PSI
-	MAXIMUM REAR MEMBRANE STRESS	93120 PSI

The velocity profiles for three reference wind velocities, 12 m/s (27 mph), 16 m/s (35 mph), 22 m/s (50 mph), are shown in Figure 5.1-1. The total wind drag versus height profiles as determined from the velocity profiles shown, and the drag coefficients in Appendix A, are shown in Figure 5.1-2. The wind pressure distribution between the front and back membranes is shown in Figure 5.1-3. The proportion of wind forces on the windward side and leeward side were taken from Reference 16. The plenum pressures required to maintain the front membrane position under the assumed wind loads are shown. Under the assumption that the front membrane remains flat ($f = \infty$) under all wind load conditions (a conservative assumption from a structural analysis standpoint), the load on the back membrane due to the positive plenum pressure and wind suctional forces on the leeward side is equivalent to the total wind load on the heliostat. The resultant load on the front membrane is zero (pressure due to wind = plenum pressure). Therefore, the back membrane carries the total wind load. Wind loads are then applied to the back membrane in accordance with the above velocity profile and a drag coefficient of 1.12 (Appendix A), and the resulting deformation and stress state are analyzed.

5.2 Membrane Finite Element Model

In order to use the Supersap finite-element analysis system to analyze the membranes, it was necessary to use a Supersap feature called Advance, which allows good approximations of large deflection problems by sequentially updating nodal coordinates during the analysis procedure. This quasi-non-linear technique is required to simulate the large deflection analysis of thin, flat membranes with this system.

The stainless steel membranes were modeled using thin plate/shell elements. The membranes were attached to the ring at the nodal points around the perimeter to satisfy boundary compatibility constraints. Due to its very low out-of-plane stiffness, the membrane is able to initially withstand only a small fraction of the total wind load. As the membrane deforms, membrane stresses dominate and bending stresses become negligible. The membrane will deflect an unrealistically large amount if the full wind load, which is many orders of magnitude greater than the membrane out-of-plane stiffness, is applied to the flat membrane in the

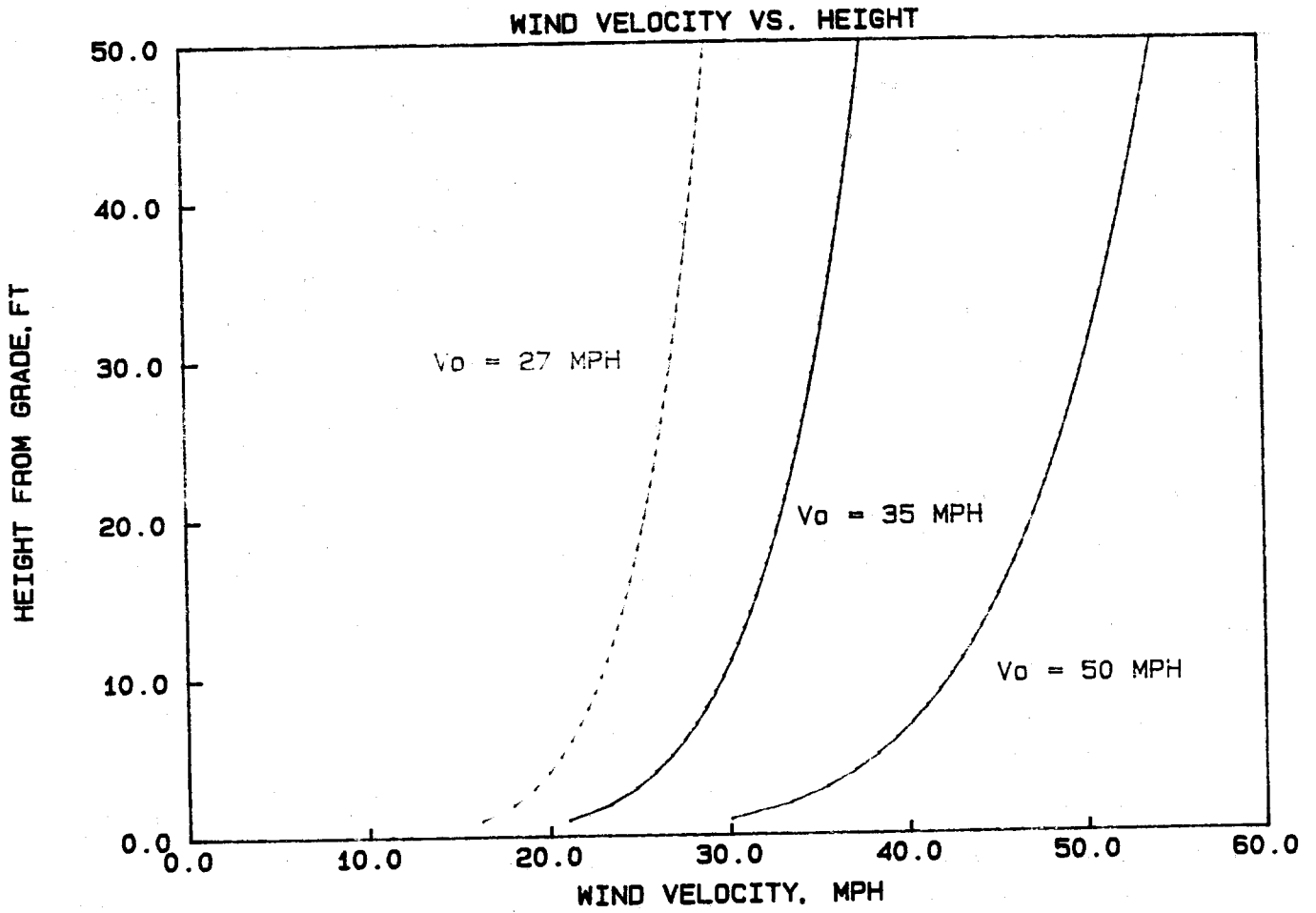


Figure 5.1-1. Wind Velocity Profiles

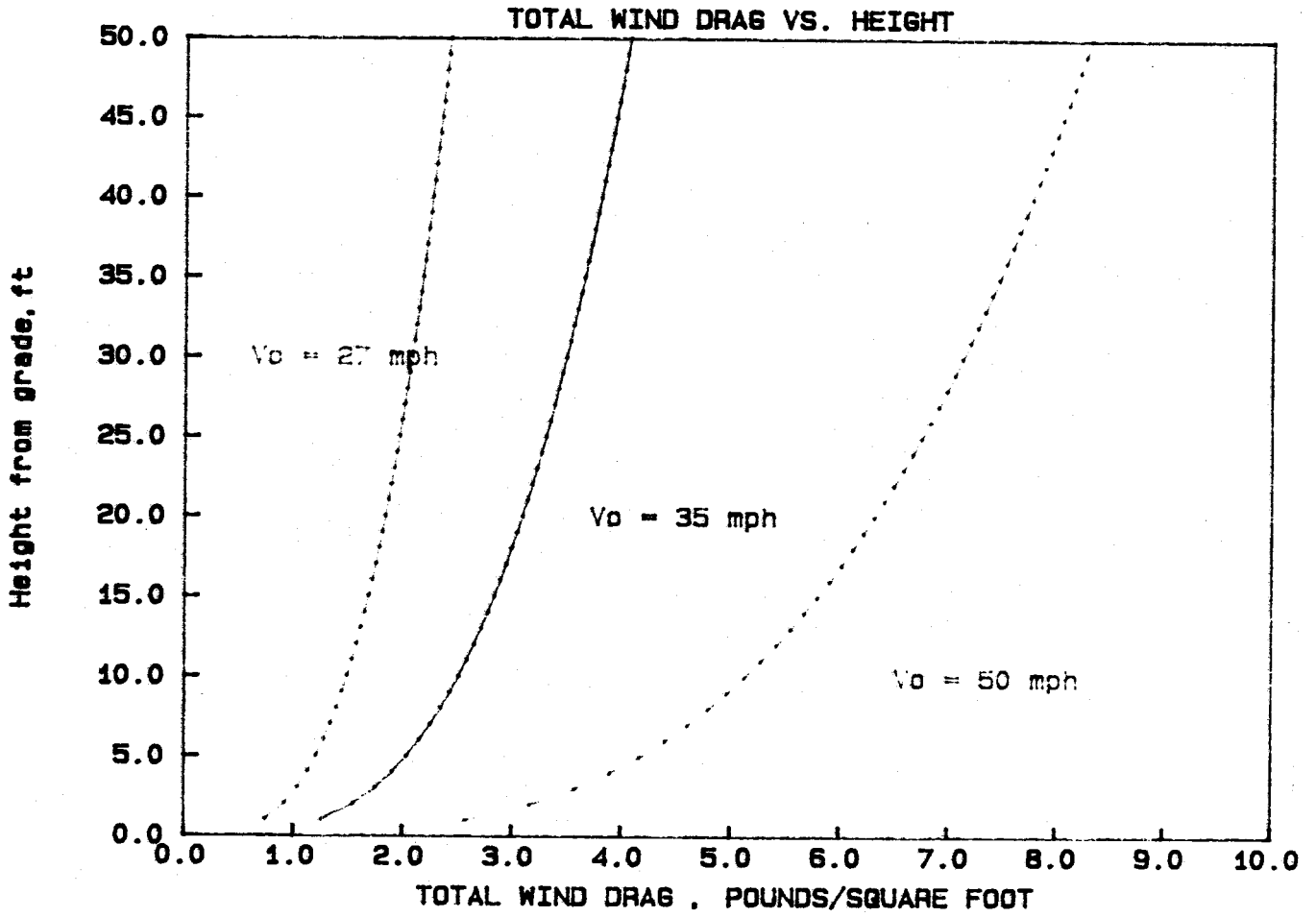
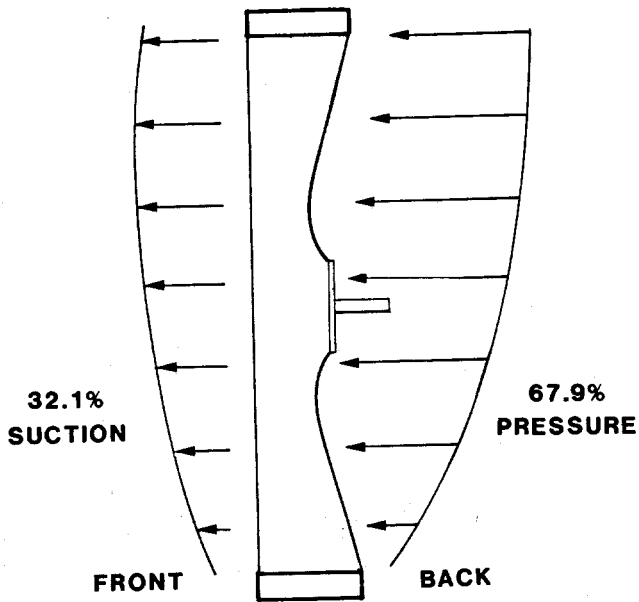


Figure 5.1-2. Wind Drag Profiles

FRONT MEMBRANE DOWNWIND

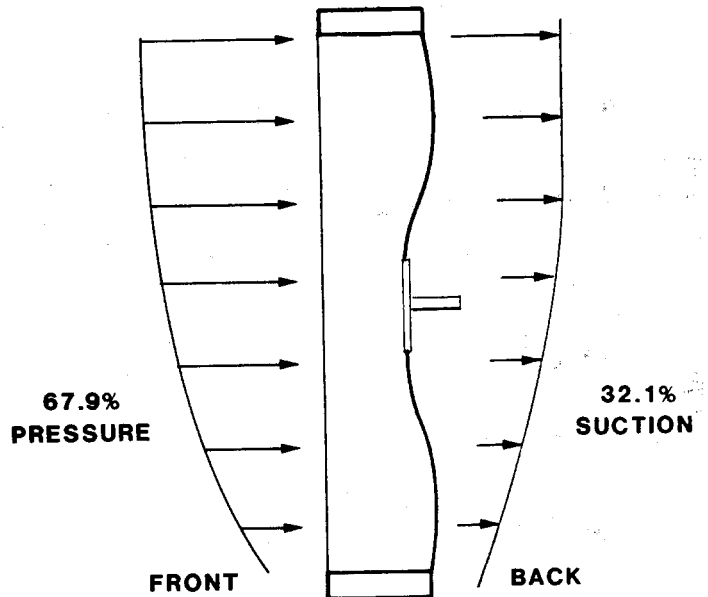


PLENUM PRESSURE

AT 27mph = -.00434 psig

AT 50mph = -.0149 psig

FRONT MEMBRANE UPWIND



PLENUM PRESSURE

AT 27mph = .00918

AT 50mph = .0315 psig

Figure 5.1-3. Heliostat Wind Loading

finite-element analysis. Therefore, it is necessary to apply only a very small fraction of the wind load on the membrane and to slowly increase the wind load until it deforms into a shape in which the membrane stresses will dominate and be able to withstand the full wind load. In the real world this procedure is instantaneous; the laws of physics and the properties of the materials would not allow an infinite deflection. In the finite-element analysis, it is necessary to perform this stepwise loading to prevent erroneous results.

The results of the above procedure were compared with an equivalent analysis performed using NASTRAN, a non-linear finite-element analysis program. The analysis was carried out on the prototype mirror module under 43-km/hr (27-mph) wind. The results showed agreement to within 8% in the ring stresses and 5% in the membrane stresses. The NASTRAN analysis is described in more detail in Section 11 - Structural Analysis of the Prototype Mirror Module.

During the membrane tensioning procedure, the membranes were prestressed to 90 MPa (13,000 psi). This pre-tension was adequately modeled in the finite-element analysis by imposing a temperature variation of -35.6°C (-32°F) between the membranes and the support ring. The two materials did not experience the same thermal strain, due to the different thermal expansion coefficients of the stainless steel membranes and the carbon steel ring. It was determined by iteration that a thermal variation of -35.6°C (-32°F) between the ring and membranes would result in membrane stresses of 90 MPa (13,000 psi).

Figure 5.2-1 shows the rear membrane deflected shape from an analysis with 12-m/s (27-mph) wind and a center deflection of 21.1 cm (8.3 in). The 21.1-cm (8.3-in) deflection was caused by the 1.83-m (72-in) focus pad pulling on the back membrane to create the proper front membrane deflection for focus. The wind loading on the back membrane, coupled with the internal plenum pressure, caused the membrane curvature, which can be seen in the figure. Figure 5.2-2 shows stress shading of the back membrane under these conditions. This figure shows lower stress around the outer edges of the membrane with a high stress concentration of 494 MPa (71,600 psi) around the perimeter of the focus pad. This high stress concentration led to the use of half-hard stainless steel for the back membrane. The results of this analysis are shown in Table 5.0-1.



27 MPH WIND, 20X
MAXIMUM DISPLACEMENT = 8.02 IN.

Figure 5.2-1. Commercial Design Rear Membrane - Deformed Shape

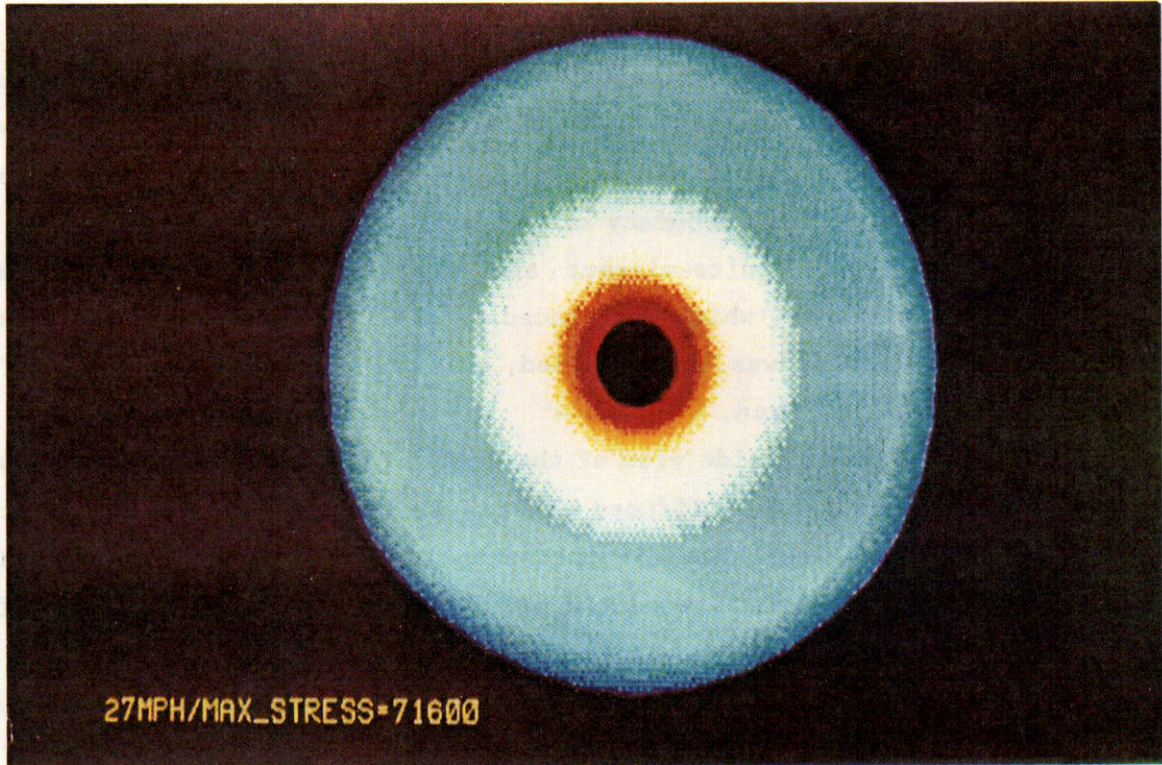


Figure 5.2-2. Rear Membrane Stress Shading

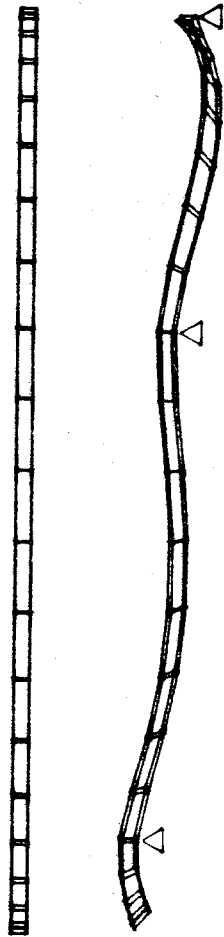
5.3 Finite-Element Model of the Ring

The finite-element model of the support ring was created using three-dimensional plate/shell elements. These elements made up the ring walls and were connected to form the rectangular cross section of the ring. The ring response to applied loading was examined both with and without the stainless steel membranes attached. Ring roll and out-of-plane deflections were quantified to obtain the required optical accuracy of the mirror module.

Results from the finite-element analysis of the trusses produced an effective truss stiffness, which was placed on the ring at the truss attachment locations. Wind loading was then applied, and the structural response of the complete system was analyzed.

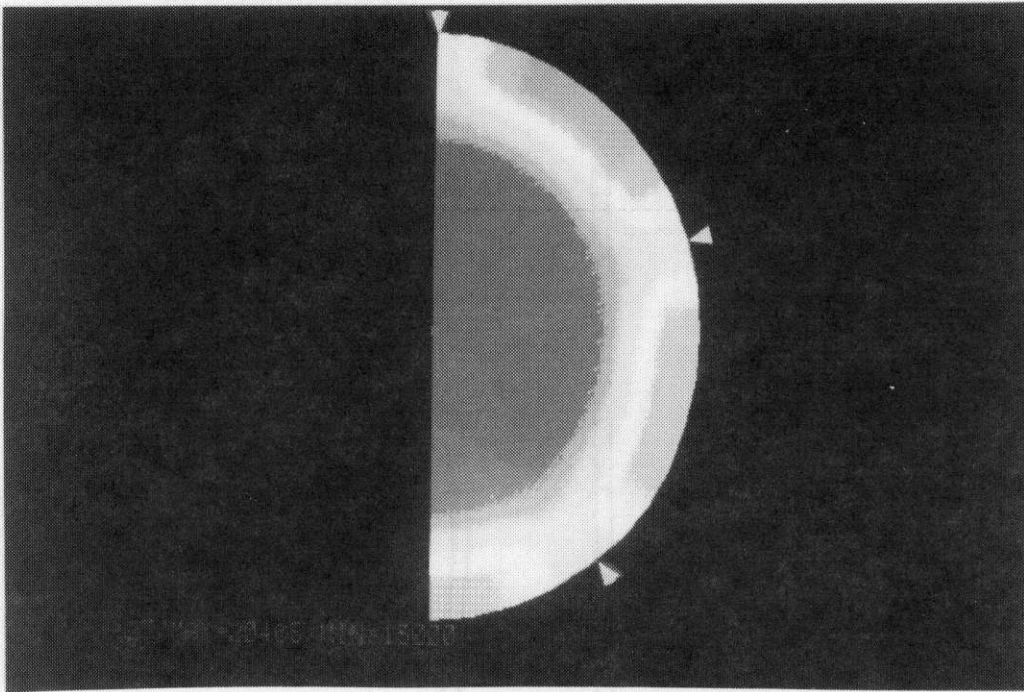
Figure 5.3-1 shows a side view of the 22-m/s (50-mph) wind-deflected shape of the ring with the truss stiffness effects included in the analysis at the location of the triangles. The displacements in the figure are magnified 250 times. The maximum ring displacement was 0.549 cm (0.216 in) at the top of the mirror module.

A trade study was performed with the finite-element model of the ring to determine the best mounting location (in the out-of-plane direction) for the attachment of the truss to the ring. The results showed a significant difference in the module response due to attachment location relative to the front and back of the mirror module. Attachments were modeled that allowed rotation about the axis tangent to the ring. The effect of allowing radial translation at the attachment points was also examined. Attachment locations both at the front of the ring and back of the ring were examined. The results of the analysis showed that radial translation of the attachment point is counter-productive in terms of maintaining uniform front membrane stress and ring planarity. Attachment at the front of the ring caused significant distortion and non-uniform stress of the front membrane during wind loading. Attachment at the back of the ring gave considerably more uniform stress in the front membrane under wind loading, but allowed slightly greater deflection of the ring between trusses. As a compromise between uniform stress and minimum ring deflection, the attachment location was chosen to be one-third of the distance from the back of the ring. Figure 5.3-2 shows stress shading of the front membrane with both front truss attachment

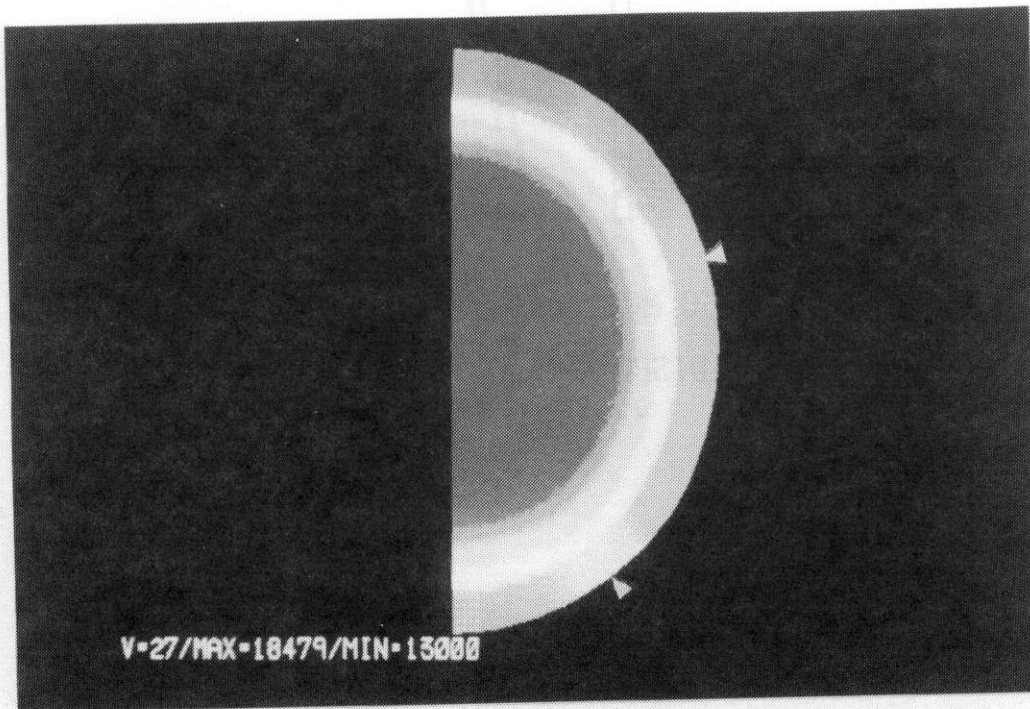


50 MPH WIND, 250X
MAXIMUM DISPLACEMENT = 0.216 IN.

Figure 5.3-1. Commercial Design Deformed Ring



Front Truss Attachment
27 mph Wind
Maximum Stress = 20465 psi, Minimum Stress = 13000 psi



Rear Truss Attachment
27 mph Wind
Maximum Stress = 18479 psi, Minimum Stress = 13000 psi

Figure 5.3-2. Front Membrane Stress Shading For Front and Rear Truss Attachment

and back truss attachment. As can be seen in Figure 5.3-2, the rear truss attachment produces a much more uniform stress distribution on the front membrane. The rear truss attachment allows more inward ring roll at the location of the trusses than the front truss attachment. This produces more uniform ring roll and therefore results in a more uniform stress distribution.

5.4 Finite-Element Model of the Truss

The finite-element model of the truss was composed of three-dimensional elastic beam elements. Beam element properties were determined from reference manuals. The end loading applied to the truss was determined from the finite element analysis of the ring/membrane system. The resultant reaction forces were determined at each of the truss tip attachment points. The loading was then applied to the truss tip to examine the truss response to wind loading. Stresses and deflections were examined to determine if the design met the strength and stiffness requirements for structural stability and optical accuracy.

Figure 5.4-1 shows the finite-element model of the truss. Figure 5.4-2 shows the truss deformations (magnified 500 times) due to the applied loading from a 22-m/s (50-mph) wind. Forces in the radial, tangential, and out-of-plane directions were also applied individually to examine the response of the truss and to optimize the chord and web size and spacing for various loading conditions. Figures 5.4-3 and 5.4-4 show highly magnified deflections for out-of-plane and tangential loading, respectively.

Flat roof-type trusses were used in the first-generation design and were also analyzed for use in this application. The roof truss model (Figure 5.4-5) was composed of three-dimensional elastic beam elements. Forces in the ring out-of-plane and tangential directions were applied to the model. This type of truss is designed to support loading over its entire span and, therefore, is not optimized for end loading in a cantilever-type application. This can be seen in Figure 5.4-6, which shows an out-of-plane deflected shape magnified 500 times; the bending is much greater in the first quarter of the truss. Comparing this to Figure 5.4-3, which also shows an out-of-plane deflected shape magnified 500 times, it can be seen that the tapered three-dimensional truss distributes the bending much more evenly.

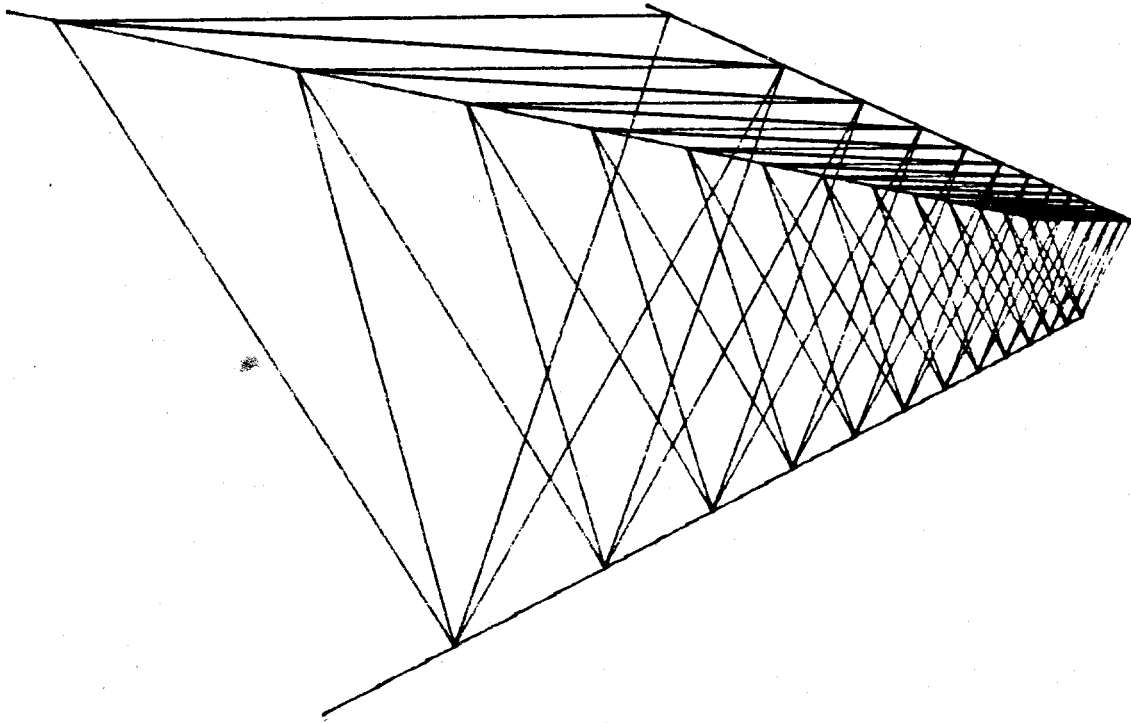
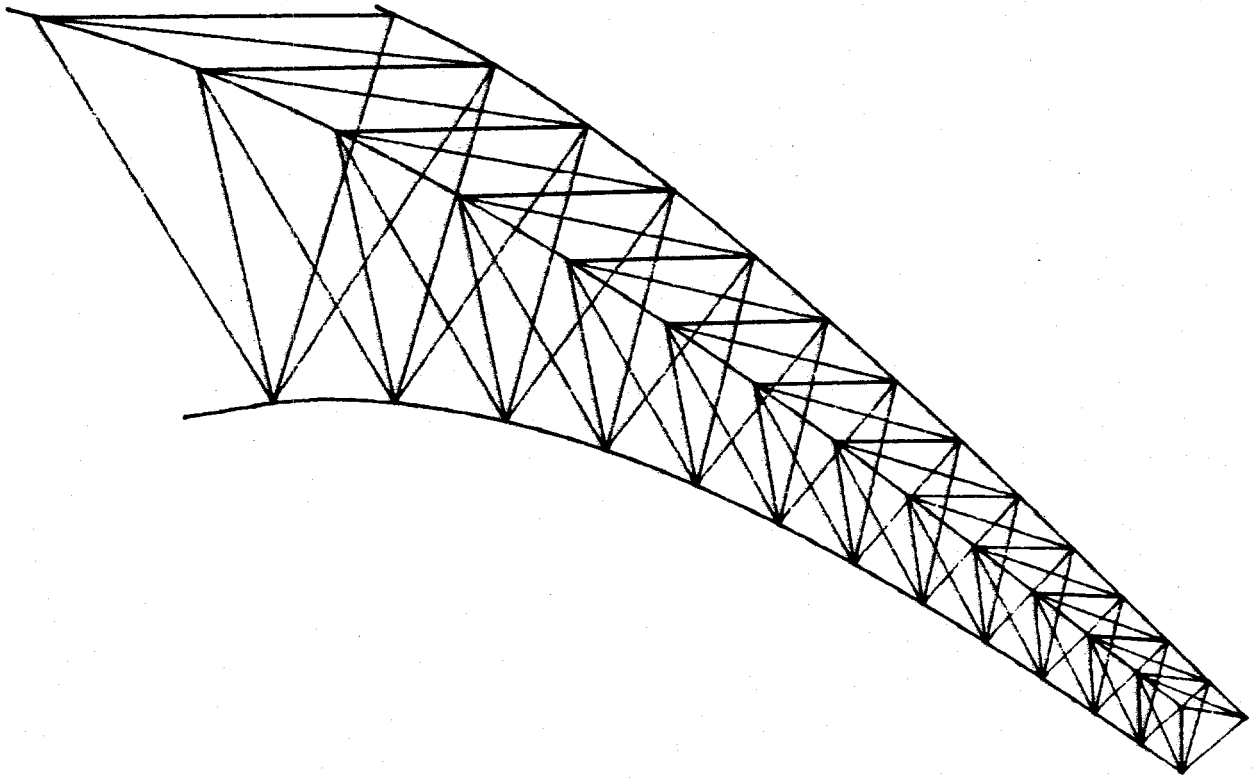
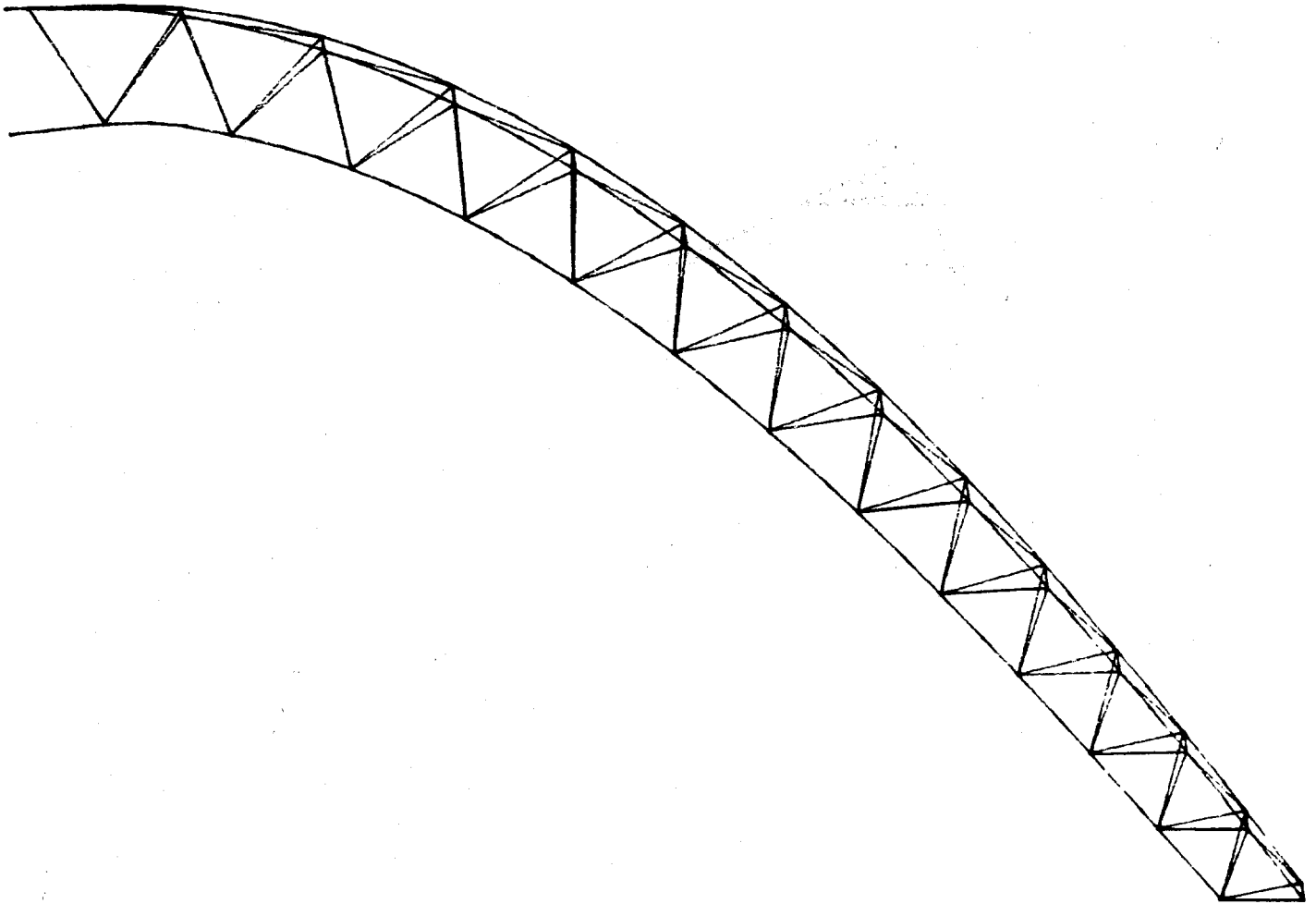


Figure 5.4-1. Commercial Design Triangular Truss Finite Element Model



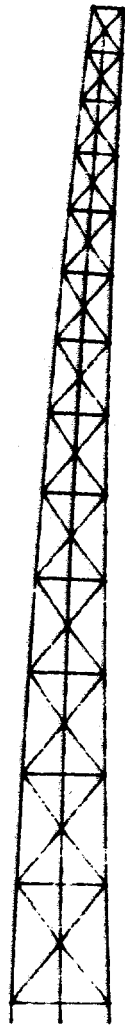
500X

Figure 5.4-2. Commercial Design Deformed Triangular Truss



500X

Figure 5.4-3. Commercial Design Deformed Triangular Truss



25X

Figure 5.4-4. Commercial Design Side Loaded Triangular Truss

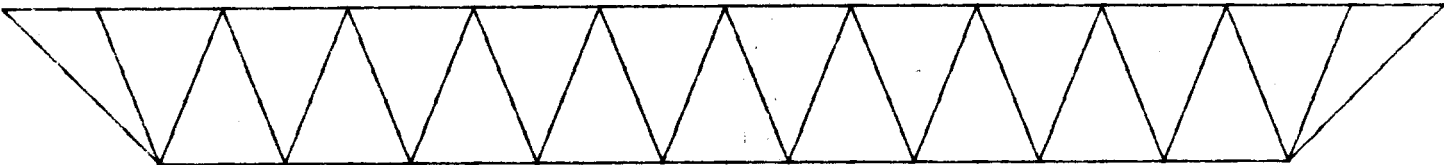
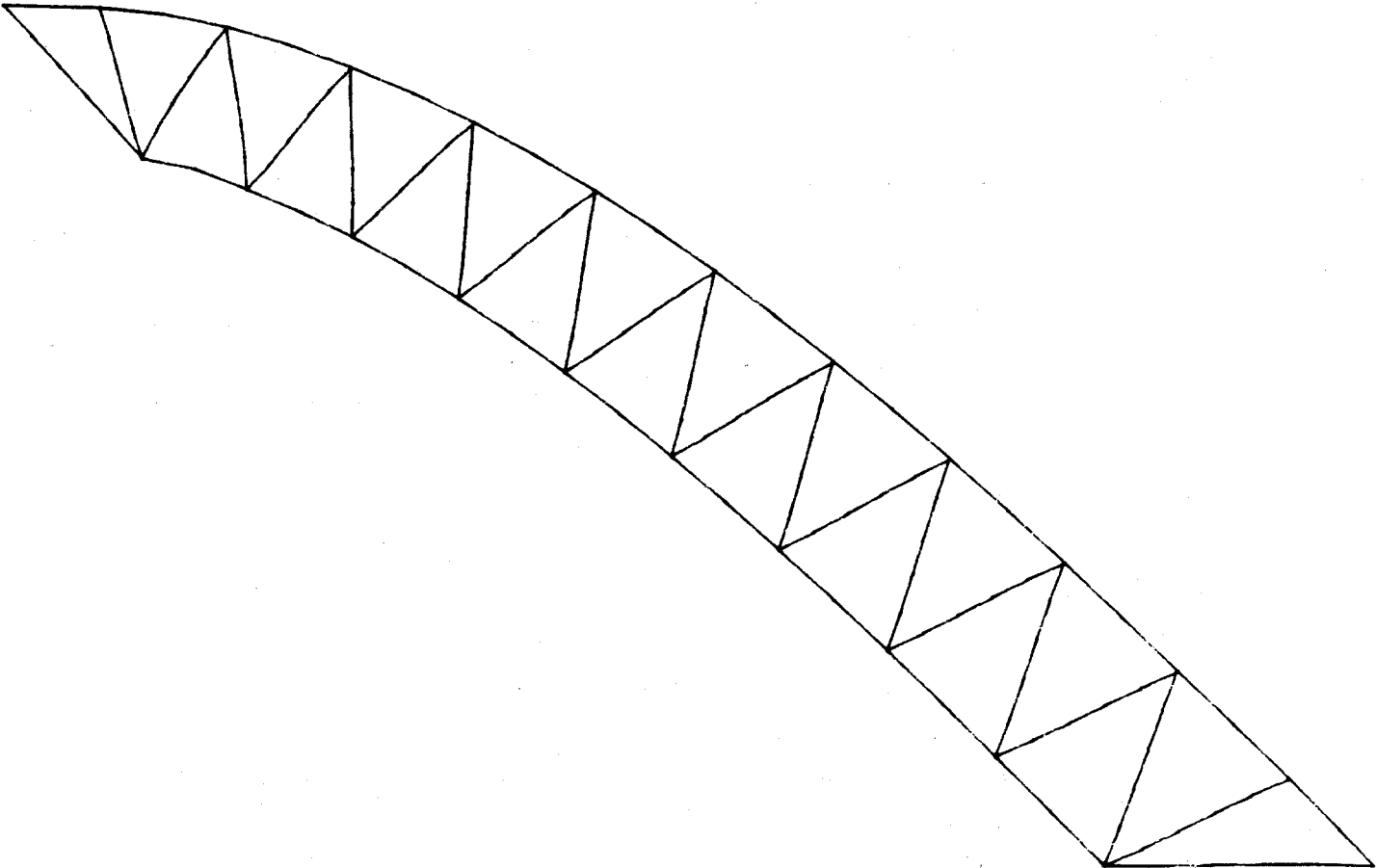


Figure 5.4-5. Roof Truss Finite Element Model



500X

Figure 5.4-6. Deformed Roof Truss 500X

The roof truss is not designed to withstand lateral loading, and analysis of the truss under a side load showed that it would be necessary to laterally support these trusses using inter-truss bridging to provide the tangential stiffness requirements of the mirror module. Inter-truss bridging was not required of the triangular tapered trusses, due to their relatively high lateral stiffness. The amount of steel required for the "flat truss with bridging" design versus the triangular tapered truss design is roughly equal. However, the triangular design has superior structural performance and results in less field assembly time.

Optimum material placement in the triangular tapered truss design provides a stiffness-and-weight-optimized structure capable of withstanding all loading requirements of this application.

5.5 Out-of-Plane Buckling of the Ring

Optical accuracy is of primary importance in the design of the mirror module. It was determined that for satisfactory optical performance, the maximum error caused by wind-load deflections is 0.60 mRad RMS slope error. This optical error translates into a maximum ring deflection of 3.75 mm (0.148 in). The ring stiffness and planarity tolerances achievable by conventional manufacturing methods dictate the out-of-plane ring distortion prior to installation of the mirror module. Once the heliostat is installed, wind loads on it exert additional out-of-plane distortions on the ring. It is therefore necessary to design the ring/membrane system with sufficient out-of-plane stiffness to limit the ring deflection under wind load to this value.

Attaching tensioned membranes to the ring causes a magnification of any out-of-plane ring deflections resulting from the manufacturing process. This magnification can be represented by a magnification factor that is multiplied by the ring deflection without the membrane attached to obtain the actual deflection the ring experiences due to the effect of the tensioned membranes.

Figure 5.5-1 shows the relation of the rectangular tube's aspect ratio to the magnification factor with the membranes tensioned to approximately 17.5 kN/m (100 lb/in). The results shown were obtained from a computer program based on structural research at SERI [17-20] and written by Dan-Ka Products. It can be

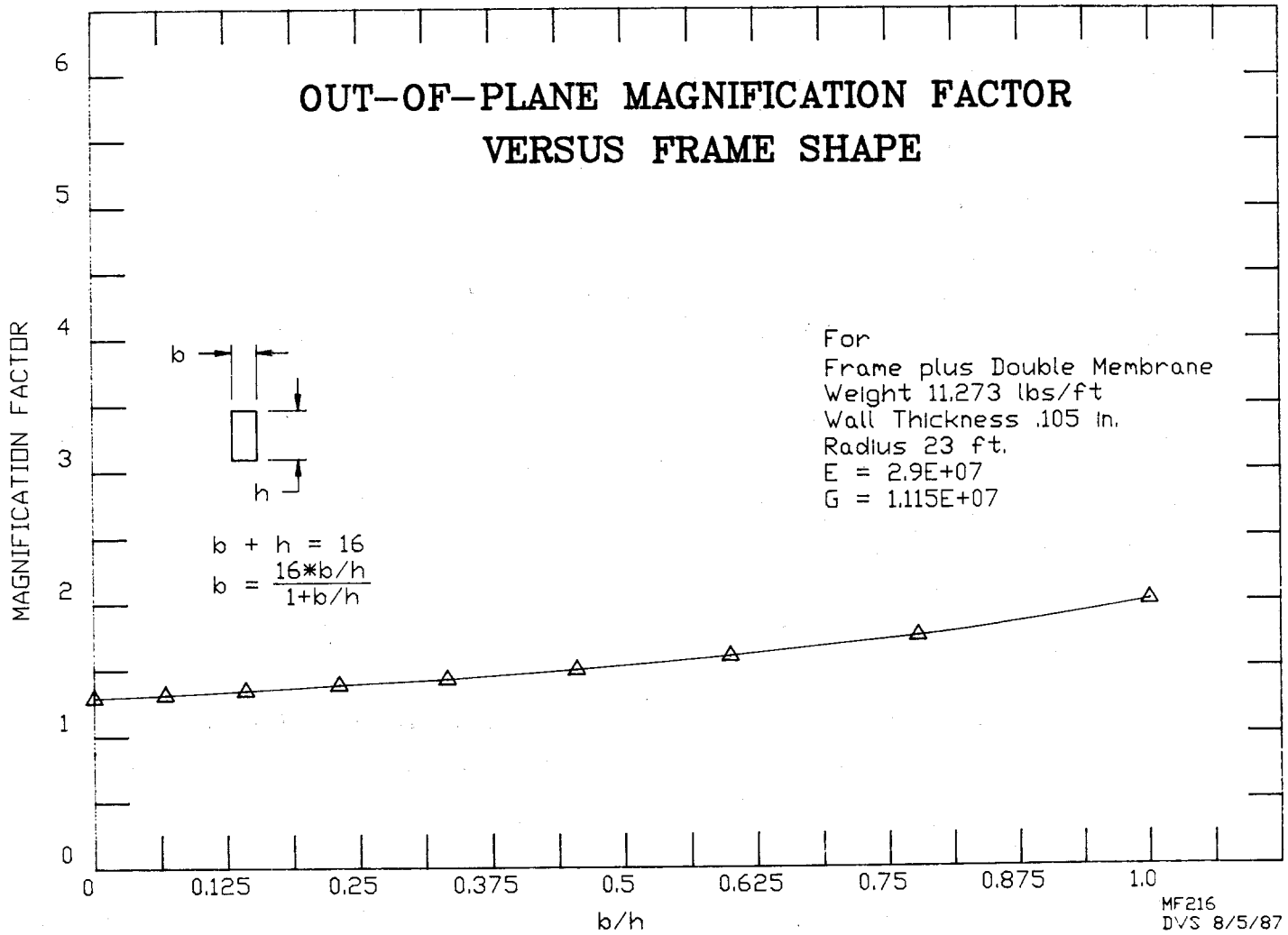


Figure 5.5-1. Rectangular Tube Aspect Ratio Versus Magnification Factor

seen from this figure that the magnification factor increases slightly with increasing aspect ratio. The figure shows a minimum magnification factor of approximately 1.3 at an aspect ratio of 0.0 (single plate) up to a factor of approximately 2.0 at an aspect ratio of 1.0. Both the ring deflection results from the finite-element wind load analysis and the calculated amplified ring out-of-plane manufacturing errors were considered in sizing the support ring to prevent excessive out-of-plane deflections.

For a five-truss support system, an N=5 ring deformation mode shape is the lowest major mode shape possible, since 5 is a prime number. Out-of-plane buckling analysis (Reference 4) has shown that for a mode shape of N=5, which simulates a wind-deflected ring shape, the critical buckling tension for out-of-plane buckling is 89.3 kN/m (510 lb/in) per membrane and the deflection amplification factor is 1.09. For a tensioned mirror module under 22.4-m/s (50-mph) wind loads and a stress level of 290 MPa (42,000 psi), $T/T_{cr} = 0.25$ (where T is the actual membrane tension and T_{cr} is the critical buckling tension). The design criteria initially established require $T/T_{cr} < 0.5$. Therefore, out-of-plane buckling should not be a problem.

5.6 Local Buckling of the Ring Wall

Local buckling analysis for the ring wall is performed using the following relation from References 21 and 22 for a rectangular plate under linearly varying compression across the plate:

$$\sigma' = K \frac{E}{1 - \nu^2} \left[\frac{t}{b} \right]^2$$

where,

σ' = Critical Local Buckling Stress

K = Geometric Constant = 23.9

E = Modulus of Elasticity = 207 GPa (30E+06 psi)

ν = Poisson's Ratio = 0.3

t = Plate Thickness = 2.3 mm (0.09 inches)

b = Ring Height = 22.9 cm (9 inches)

This relation indicates a critical local buckling stress of 543 MPa (78,800 psi). The maximum ring stress determined from the finite-element analysis is 182 MPa (26,373 psi), well below the critical stress value.

6.0 DESIGN OF THE FOCUS-CONTROL SYSTEM

The focus-control system detects the position of the front reflective membrane and compensates for any changes in its position due to wind load changes by adjusting the pressure of the internal plenum behind it. The focus-control system is a critical component of the overall design. Even if the mirror module is structurally and optically sound, failure to accurately sense the position of the front membrane and to compensate for any changes in its position can result in a non-functional heliostat design. The focus-control system can be divided into three subsystems:

1. Plenum pressure adjustment subsystem,
2. Front membrane position measurement subsystem,
3. Electronic control subsystem.

6.1 Description of the Plenum Pressure Adjustment Subsystem

The system used for implementing changes in plenum pressure in the first-generation mirror module design consisted of a pressure and vacuum blower coupled with a series of valves for evacuating and pressurizing the plenum. This system had a very slow response to variations in wind velocity.

A unique adjustment system for the mirror module's plenum pressure is used in the improved design. An isometric view of the system is shown in Figure 6.1-1, and its functional operation is shown in Figure 6.1-2. A linear actuator is used to move the back membrane in and out in order to change the plenum pressure. An LVDT position detector mounted inside the plenum senses the position of the front membrane, which is relayed to a microprocessor base control system. This system controls the linear actuator. The theory of operation of the pressure control system is that an increase in plenum volume will result in a decrease in plenum pressure. This is shown below in the second form of the Ideal Gas Law.

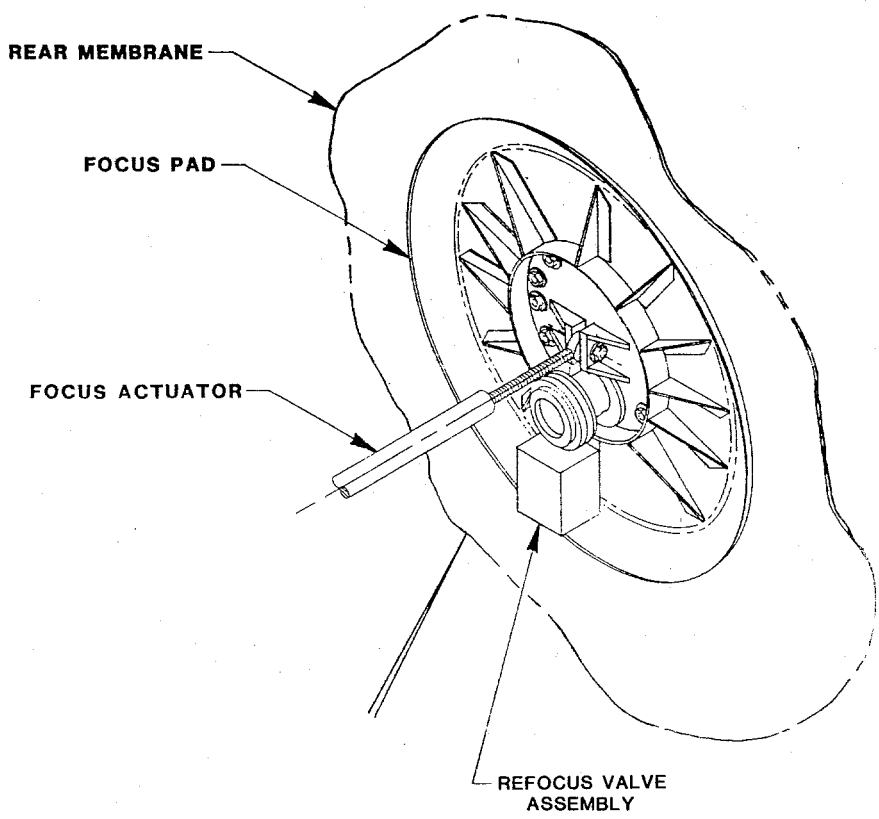


Figure 6.1-1. Focus Control System Isometric View

MEMBRANE MODULATION SYSTEM WORST CASE OPERATING CONDITIONS

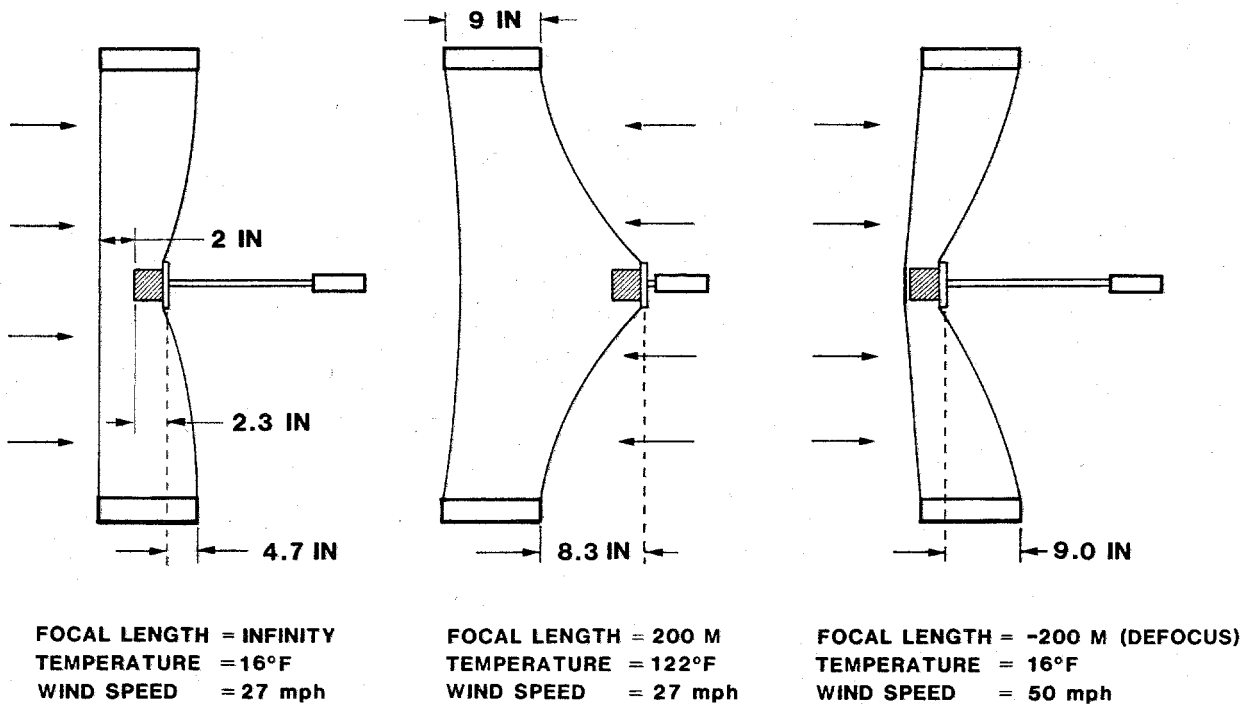


Figure 6.1-2. Membrane Modulation System Worst Case Operating Conditions

$$\frac{P_1 V_1}{T_1} = \frac{P_2 V_2}{T_2}$$

where, P = Pressure
V = Volume
T = Temperature

The process is assumed to be isothermal, so that the temperatures drop out of the equation, resulting in a simple relationship between plenum pressure and volume. The main advantage of the system is that rapid changes in plenum volume can be implemented in a short time, resulting in rapid changes in plenum pressure. This fact makes the system effective in compensating for rapid changes in wind velocity on the mirror module.

A diagram of the complete focus-control system is shown in Figure 6.1-3. Beginning in the upper left-hand corner of the diagram, the LVDT front membrane position indicator is energized by a 12-volt power supply and outputs a minus 6 to plus 6 volt signal proportional to the position of the front membrane. This signal is sent to the microprocessor base control board, which converts the signal to a digital signal, and together with operational parameters received via the RS-422 data link from the control tower computer console, the desired position of the rear membrane linear actuator is determined. A refocus valve (vent valve) is included in the system in the upper right-hand corner of the diagram. The purpose of this valve is to periodically compensate for leaks in the mirror module. This is accomplished by opening the valve and fully extending the linear actuator to expel excess air in the plenum after the linear actuator has reached its full retraction position. Once the air is expelled, the vent valve is closed and the linear actuator assumes normal operation. If techniques for completely sealing the mirror module plenum can be developed, this vent valve may be eliminated.

Defocusing of the mirror module is necessary in emergency conditions in order to remove the flux quickly from the receiver. For example, failure of the receiver circulation pump would result in a loss of coolant to the receiver and would require a rapid removal of heat flux from the receiver in order to avoid damaging the receiver tubes. Defocusing of the stretched-membrane mirror module

FOCUS CONTROL SYSTEM DIAGRAM

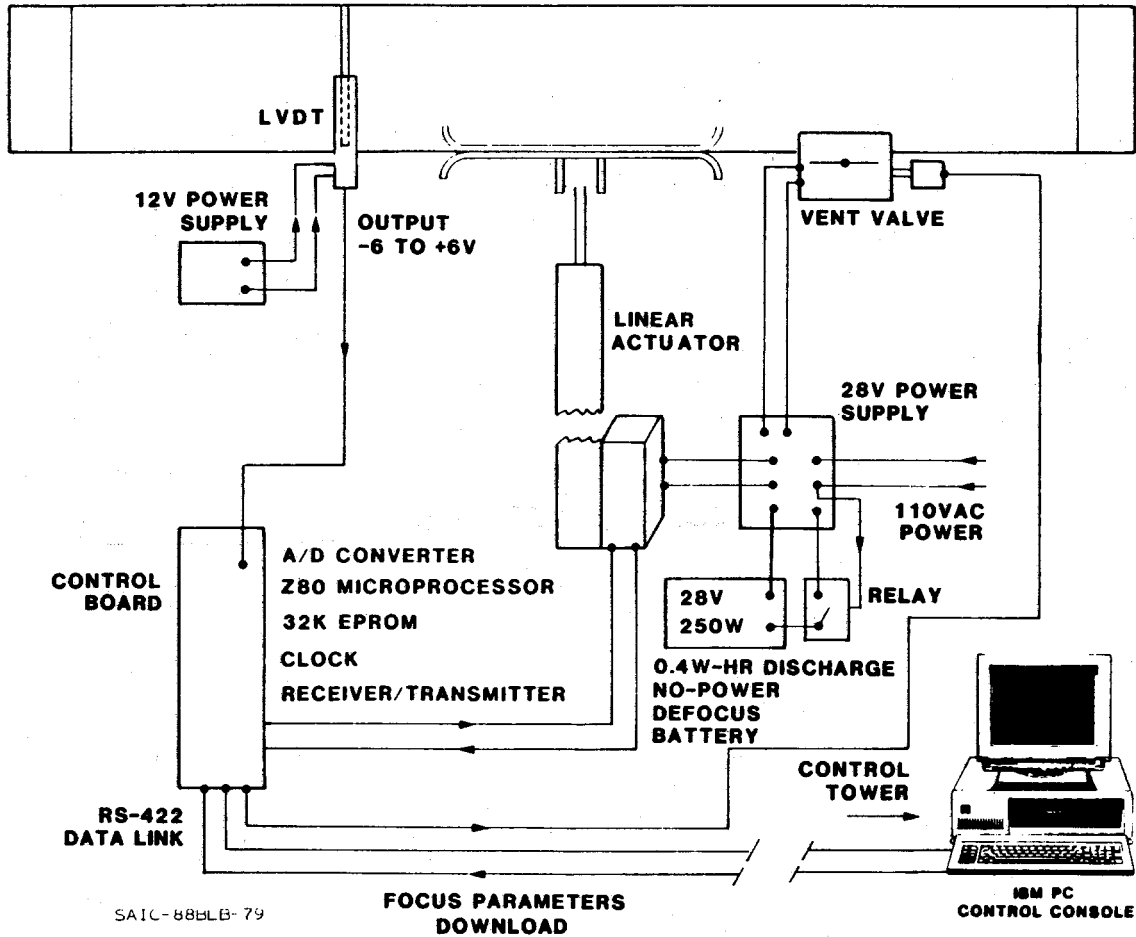


Figure 6.1-3. Focus Control System Diagram

is accomplished by extension of the linear actuator to increase the plenum pressure, which produces a concave surface on the reflective side of the mirror module. If a wind load exceeding 8.05 m/s (18 mph) is present on the front membrane of the mirror module, the inner defocus pad actually touches the front membrane and pushes the center of the front membrane out in order to accomplish defocus.

In the event that there is a total loss of power, the linear actuator will not have line power to accomplish defocus. Therefore, a battery back-up power supply is included in the system. A battery is practical for this application because very little energy is required to accomplish defocus. The linear actuator requires a maximum of 7 amps at 28 volts for about 3 seconds to accomplish defocus. As shown in Figure 6.1-3, a small lead-acid gel cell battery is connected to a relay system, which trips shut on loss of power. The linear actuator is driven in until it reaches the internal mechanical limit switch. Therefore, defocus can be accomplished with no external power.

The linear actuator is attached to a 1.8-m (6-ft) diameter plate that is used to distribute the stress caused by modulating the membrane. The membrane stress concentration around the plate was calculated to be 642 MPa (93,120 psi), at the maximum required linear actuator deflection of 23.1 cm (9.1 in). Due to this high stress, half-hard 304L stainless steel with a minimum yield strength of 820 MPa (120,000 psi) is used for the back membrane, while annealed 304L stainless steel with a minimum yield strength of 241 MPa (35,000 psi) is used for the front membrane. Between 1/3 and 2/3 of the heliostat wind load is transferred directly to the pedestal drive from the linear actuator when the system is operating. Therefore, a reduction in truss tip and ring deflection is possible with this system.

Attachment of the focus pad to the membrane is shown in Figure 6.1-4. A dish-shaped circular plate is positioned on either side of the back membrane as shown. A hole in the center of the back membrane allows clearance for the bolts to attach the inner pad to the outer pad. The holes are reinforced with stainless steel flat rings welded to the membrane.

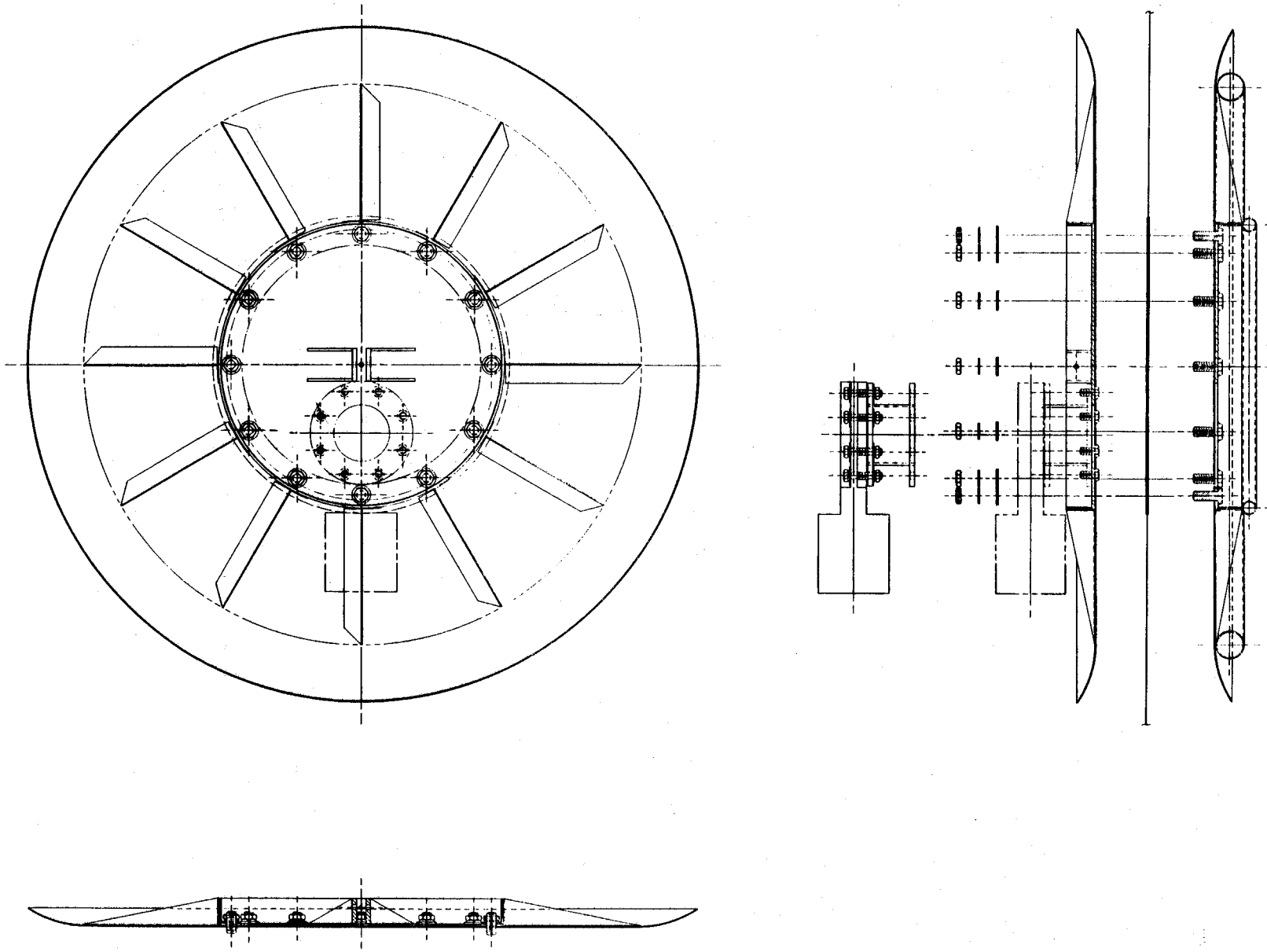


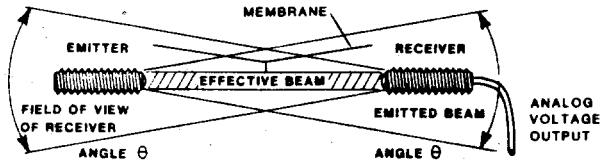
Figure 6.1-4. Focus Pad Assembly

6.2 Selection of the Front Membrane Position Measurement Subsystem

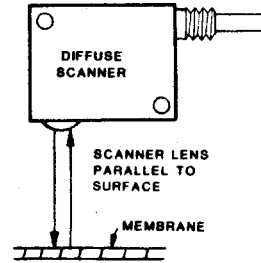
The focus-control system used in the first-generation stretched-membrane mirror module design consisted of a visible light emitter/receiver mounted on the ring ID between the two membranes that projected a beam of visible light to a diametrically opposed retro-reflector, which returned the light signal to the receiver. A strip of metal was attached to the center of the front membrane, which interfered with the return of the reflected beam to a degree proportional to the amount of light blocked. The receiver produced an analog signal proportional to the amount of light returned to the receiver. Problems were incurred in getting the system to operate properly because of erroneous signals due to light scatter and internal reflections in the plenum of the mirror module.

Five alternate methods were proposed for detection of membrane position in the improved mirror module design. These five methods are shown in Figure 6.2-1. The system in the upper left consists of an infrared emitter and an opposed receiver, which produces an analog voltage output proportional to the amount of light received. A metal strip is attached to the front membrane and is used to block the effective beam of the emitter to a degree proportional to the position of the membrane. In the technique shown in the top right, an infrared diffuse scanner produces a light beam perpendicular to the surface of the front membrane, and the amount of light reflected and returned to this scanner produces an analog voltage signal. This system had the lowest cost for components; however, the accuracy of the membrane position measurement was not adequate. A laser coupled with a silicon position sensor strip is shown in the middle left of the figure. The laser beam is intercepted by the one-dimensional position-sensitive detector, and an analog voltage signal is produced based on the position of the incident light on the strip. The system has the potential to be very accurate; however, the cost is considered to be prohibitive for this application. A system similar to that used in the first prototype is shown in the middle right of the figure. However, this system uses infrared light instead of visible light and is an off-the-shelf unit. This system was rejected because of its similarity to the first-generation system and because of concerns about the signal strength produced after the emitted light has to travel some 28 m (92 ft) before hitting the receiver. The system shown in the bottom consists of a mechanical LVDT (linear

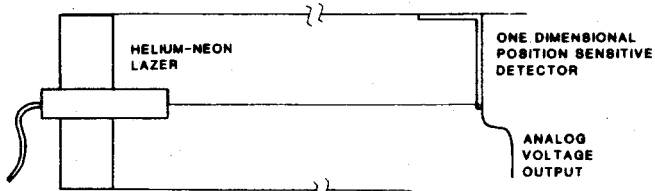
FOCUS CONTROL - MEMBRANE POSITION MEASUREMENT OPTIONS



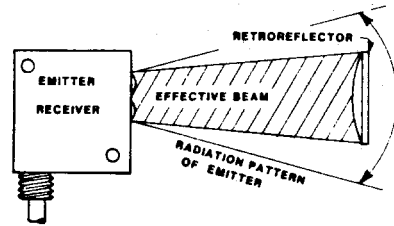
INFRARED LED - APPOSED MODE



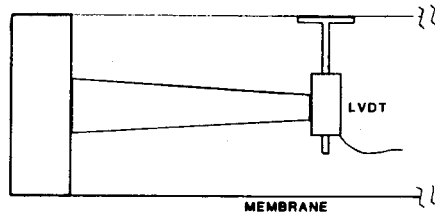
VISIBLE LED DISTANCE MEASURING SCANNER



LASER/SILICON PSD SYSTEM



INFRARED LED - RETROREFLECTIVE MODE



MECHANICAL LVDT SYSTEM

SAIC-87BLB-101

Figure 6.2-1. Focus Control - Membrane Position Measurement Options

varying distance transducer), which is in physical contact with the front membrane. As the front membrane moves, the LVDT produces an analog voltage signal proportional to the front membrane's position.

The two preferred concepts were determined to be the infrared LED in the opposed mode and the mechanical LVDT system. Operation of the infrared LED in the opposed mode was evaluated by testing the emitter and receiver at a distance of 14 m (46 ft) apart, mounted between two 61.0-cm (24-in) wide strips of stainless steel. Although this system worked satisfactorily, some problems were incurred in eliminating erroneous signals coming from infrared light reflected off the membrane rather than being projected directly to the receiver. Tests with the LVDT system showed very reliable operation and a good feedback signal proportional to the membrane position. Therefore, this system was selected for implementation in the commercial-size mirror module design and in the prototype design. In both these designs the LVDT is mounted on a lower truss at a distance 1.22 m to 1.83 m (4 to 6 ft) from the tip and penetrates the back membrane to touch the front membrane. Mounting the LVDT to the truss rather than on an arm projecting from the ring was shown to have less error due to structural deflection.

6.3 Fluid Dynamic Analysis of the Mirror Module

In order to assure that the rear-membrane-modulation focus-control system would operate properly, it was essential to determine the relationship between external wind loads, plenum air temperature, rear membrane deflected shape, and the effects these parameters would have on the required position of the linear actuator in order to accomplish the desired focus. A computer program was written to simulate the hydraulics of the system. Plenum air temperature, external wind speeds, wind direction, and membrane shape deformation were considered in the simulation. The program was written in Microsoft Fortran for use on IBM-PC compatible computers. The program assumes a sealed plenum and a back-membrane modulation-type pressure control system. However, the external and internal pressures, and front membrane deflections calculated are valid for any type of pressure control system.

The solution for the deflected shape of the rear membrane caused by modulation of the linear actuator is based on the variational closed-form modeling approach given in Reference 20. This approach was modified to predict the shape of the deflected rear membrane. An accurate prediction of this shape was necessary in order to determine the volumetric change that results from modulation of the back membrane from the center linear actuator's attachment location.

A sample output from the program is shown in Table 6.3-1. Inputs to the program are the heliostat diameter, ring depth, membrane thickness, membrane initial tension in pounds per inch, wind speed, wind direction, (front or back side), and desired focal length. The program calculates the required actuator position and plenum volumetric change for a range of ambient temperatures (the internal plenum temperature is assumed to be equal to the ambient temperature). The effect of plenum air temperature on the internal plenum pressure is based on the Ideal Gas Law. The net volumetric change is calculated by subtracting the plenum volume loss due to front membrane focusing from the plenum volume increase due to retraction of the linear actuator and subsequent rear membrane deformation. As shown at the bottom of Table 6.3-1 several other pressures and deflections are calculated to complete the analysis.

Results from the focus-control simulation program are shown graphically in Figure 6.3-1. The required actuator travel for three cases is plotted against ambient temperature. As shown by a comparison of the top two curves, very little actuator travel is required to compensate for a wind speed change from 0 to 12.1 m/s (0 to 27 mph) at a given focal length. The top and bottom curves of the graph define the envelope of normal operating conditions.

A second computer program was written as a post-processor to the focus-control simulation program in order to determine the response time to changes in wind loads on the mirror module. Information on linear actuator force versus extension speed was obtained from the manufacturer. This information was then used with the results of the previous simulation to determine the response time versus wind speed. The resulting curve is shown in Figure 6.3-2. The predicted response time to a wind speed gust from one velocity to another can be determined using this graph. As shown, a wind speed change from 0 to 12.1 m/s (0 to 27 mph) can be compensated for in less than two seconds. The extremely rapid response

Table 6.3-1. Program Focus - Focus Control Simulation Program

HELIOSTAT DIAMETER (FT) = 46.00 RING DEPTH (IN) = 9.00
 MEMBRANE THICKNESS = .0030 INITIAL TENSION = 39.0
 WIND SPEED (MPH) = 50.0 NSIDE = 2
 FOCAL LENGTH (FT) = 636.

AMBIENT TEMPERATURE (F)	ACTUATOR POSITION	VOLUME CHANGE (IN ³)
.0	3.018	-281773.8
5.0	3.273	-261429.8
10.0	3.528	-241085.8
15.0	3.783	-220741.9
20.0	4.038	-200397.9
25.0	4.293	-180053.9
30.0	4.548	-159709.9
35.0	4.803	-139366.0
40.0	5.058	-119022.0
45.0	5.313	-98678.0
50.0	5.568	-78334.1
55.0	5.823	-57990.1
60.0	6.079	-37646.1
65.0	6.334	-17302.1
70.0	6.589	3041.8
75.0	6.844	23385.8
80.0	7.099	43729.8
85.0	7.354	64073.8
90.0	7.609	84417.7
95.0	7.864	104761.7
100.0	8.119	125105.7
105.0	8.374	145449.6
110.0	8.629	165793.6
115.0	8.884	186137.6
120.0	9.139	206481.6
125.0	9.395	226825.5

FRONT MEMBRANE CENTER DEFLECTION (IN) = 2.4953

PLENUM PRESSURE (psig) = -.02073

DELTA PRESSURE-FRONT MEMBRANE (psi) = .00585

DELTA PRESSURE-BACK MEMBRANE (psi) = .05221

MAX MEMBRANE DEFLECTION BEFORE YIELD (IN) = 10.059

MAX MEMBRANE DELTA PRESSURE BEFORE YIELD (IN) = .0693

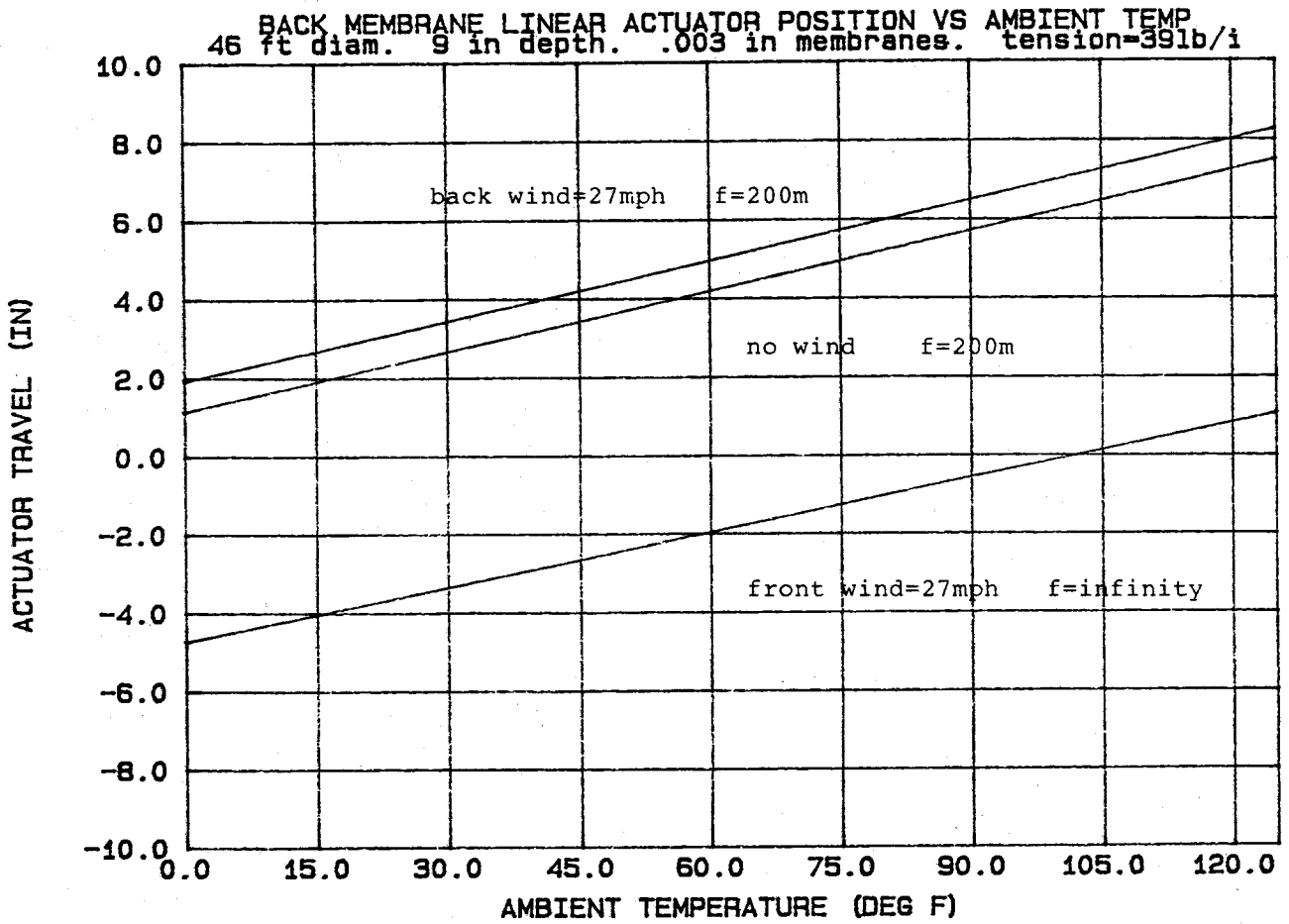


Figure 6.3-1. Linear Actuator Position Versus Ambient Temperature

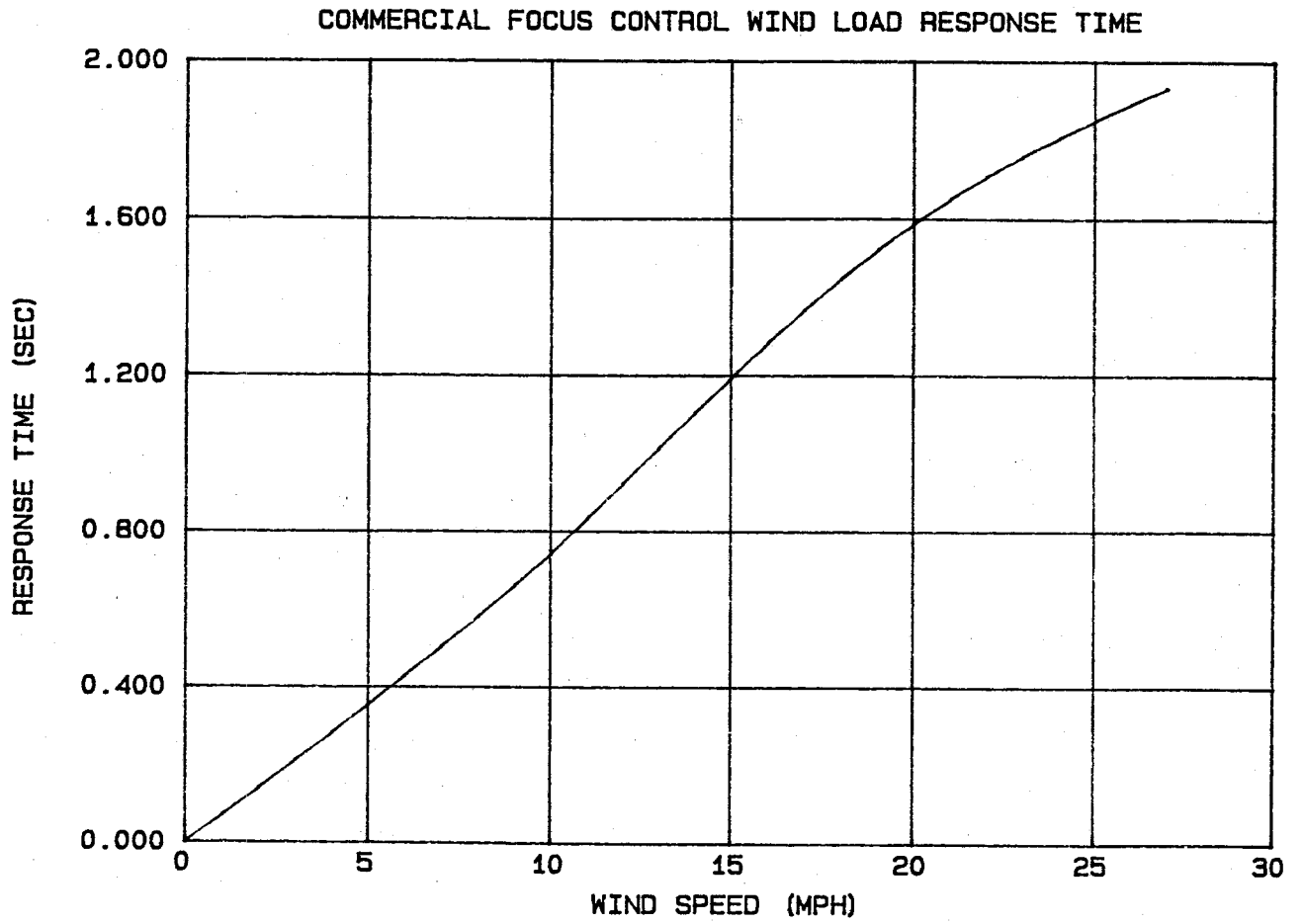


Figure 6.3-2. Commercial Heliostat Predicted Focus-Control Wind Load Response Time

time to wind load changes is the main advantage of the rear-membrane-modulation focus-control system.

Another major advantage of this type of system is the reduced parasitic power requirements. The actuator draws a maximum of 7 amps at 28 volts when operating. The total power consumed by the actuator when operating is 196 watts. The duty cycle of the linear actuator was estimated to be about 5%, resulting in an average power requirement of 9.8 watts. Initial evaluations of the prototype mirror module indicated that the duty cycle of the linear actuator might be even less than the 5% predicted. A small amount of additional power is required for the focus-control electronics and LVDT position indicator.

6.4 Focus Control Logic

Because the rear-membrane-modulation focus-control system encompasses a completely new approach to controlling the focus, a new approach to the system's operational logic was also required. The focus-control logic diagram is shown in Figure 6.4-1. A series of inputs is down-loaded from the control computer in the control tower. These inputs contain information about the front membrane's set point and dead band, signal processing parameters, and linear actuator reference positions. Interrupt signals from the control computer are also available for defocusing and stowing the mirror module. The various reference positions referred to in Figure 6.4-1 are defined in Figure 6.4-2. The reference positions are translated to the reference plane shown when they are called out in the focus-control logic.

The focus-control electronics for the improved mirror module are completely self-contained and autonomous. The control system is based on a Z-80 microprocessor and a EPROM (erasable programmable memory). The control logic was developed in detail in the Turbo Pascal programming language and transferred to the EPROM on the control board. Changes in the software can be made fairly easily by making changes on the IBM-PC control computer and then reprogramming the EPROM chip. Once the operational focus parameters have been down-loaded from the control computer to the heliostat control board, the heliostat operates autonomously with no inputs required from the control computer. However, the control board on the heliostat can be interrogated from the control computer to

FOCUS CONTROL LOGIC

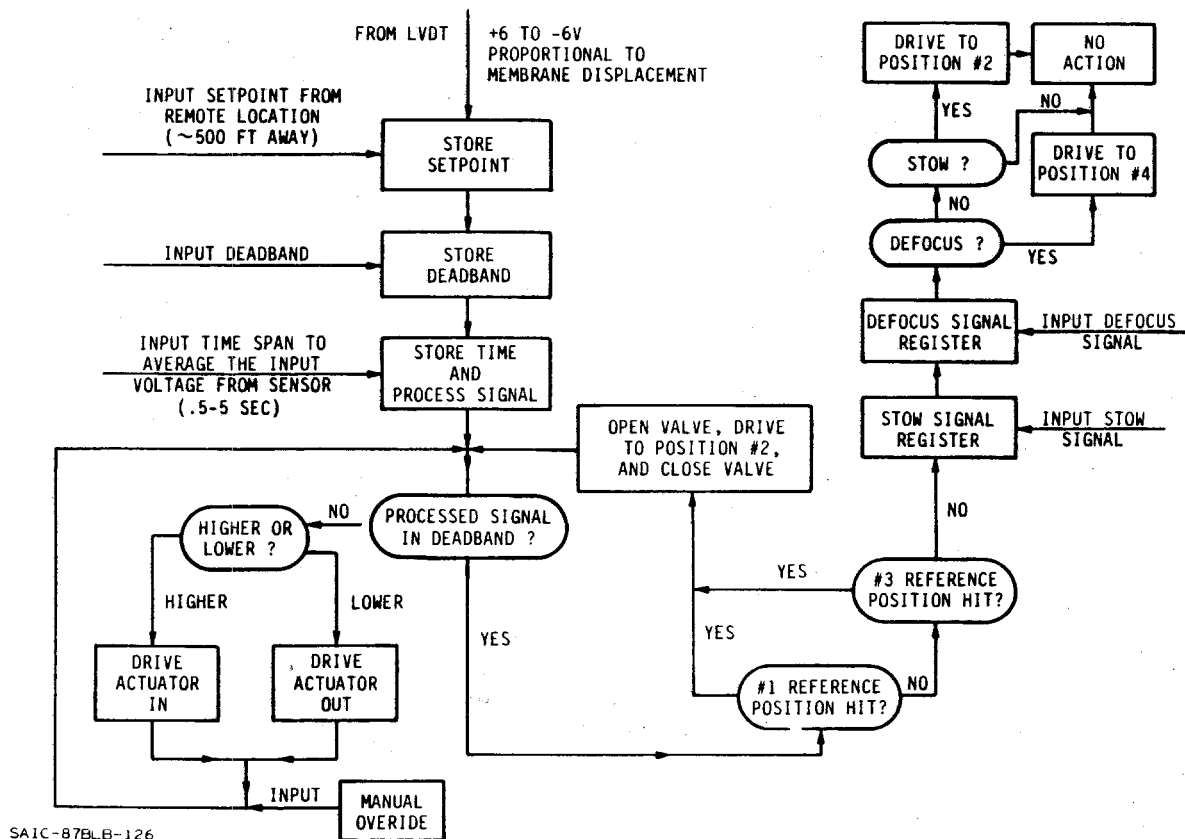


Figure 6.4-1. Focus Control Logic

FOCUS CONTROL LINEAR ACTUATOR REFERENCE POSITIONS

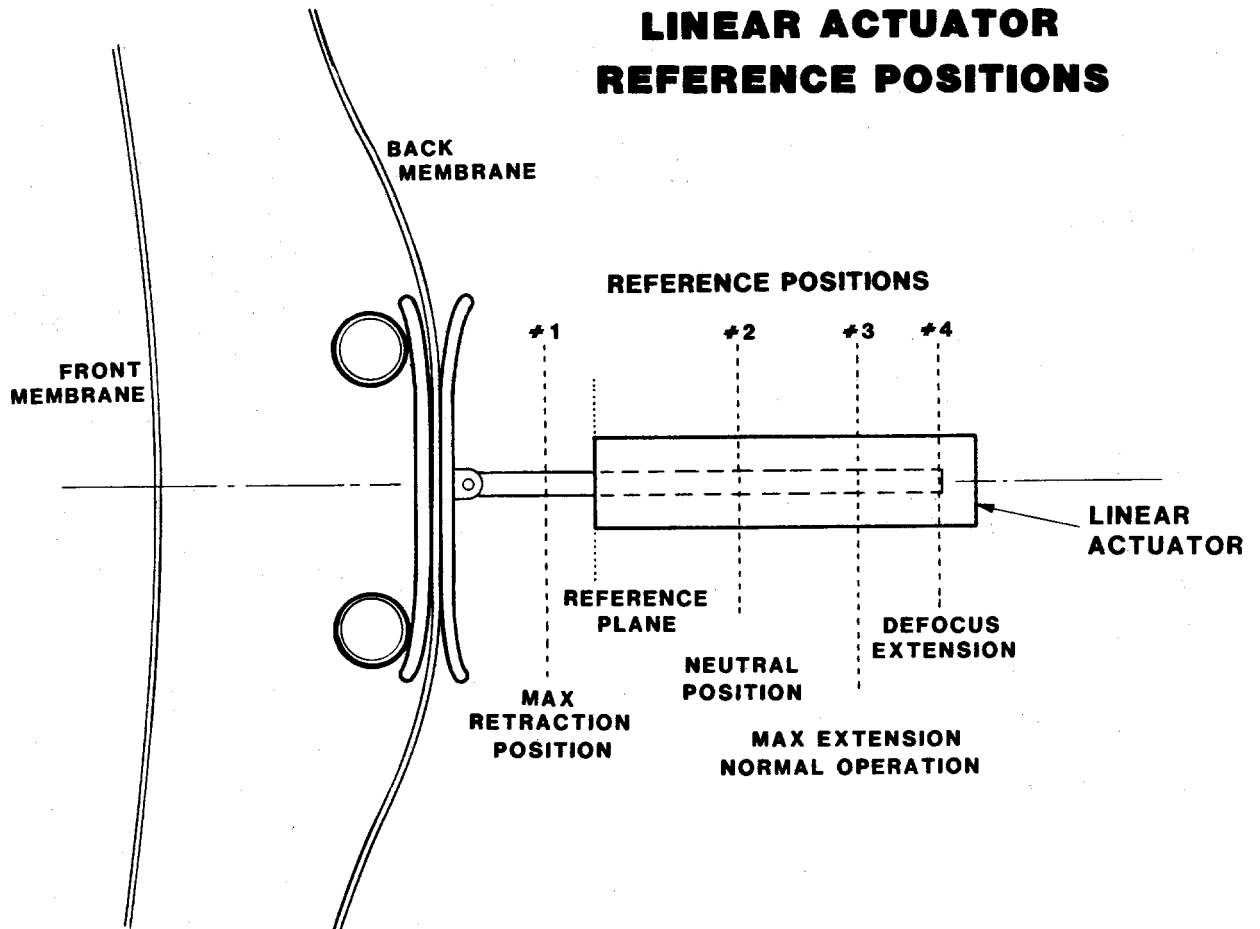


Figure 6.4-2. Reference Positions for the Focus Control Linear Actuator

determine the actuator and LVDT positions at any point in time. Table 6.4-1 is a printout of the interactive control screen for the focus-control computer. The options for heliostat control are shown in the left column. The options for set points for various parameters are shown in the right column. Numbers can be input between 1 and 255 to set each of the parameters. These values represent computer bits and have no engineering units associated with them.

Table 6.4-1 Computer Menu for Focus Control

SAIC Energy Projects Division Stretched-Membrane Mirror Module

	VALUE
	SetPoint CP := 153
	SetPoint DP := 2
	SetPoint DM := 2
	SPerBurst := 10
	DBetweenS := 4
	DBetweenB := 1
	BPAverage := 1
	not used := 1
	SPArmAve := 10
	ArmMinPos := 170
	ArmMaxPos := 221
	StowPos := 190
	DefocusPos := 220
	EqualPos := 190
	not used := 1
* Focus Controller/Host Communications *	
1: Load Parameter Block to Remote Controller	
2: Obtain and Display Remote Parameter Block	
3: Locally Change Parameter Values	
4: Not available	
5: Equalize Membrane	
6: Defocus Membrane	
7: Stow Unit	
8: Exit Stow or Defocus Mode	
9: Obtain Arm and Front Membrane Positions	
0: Return to MS-DOS	

Please Make Your Selection:

7.0 COMMERCIAL MANUFACTURING SCENARIO

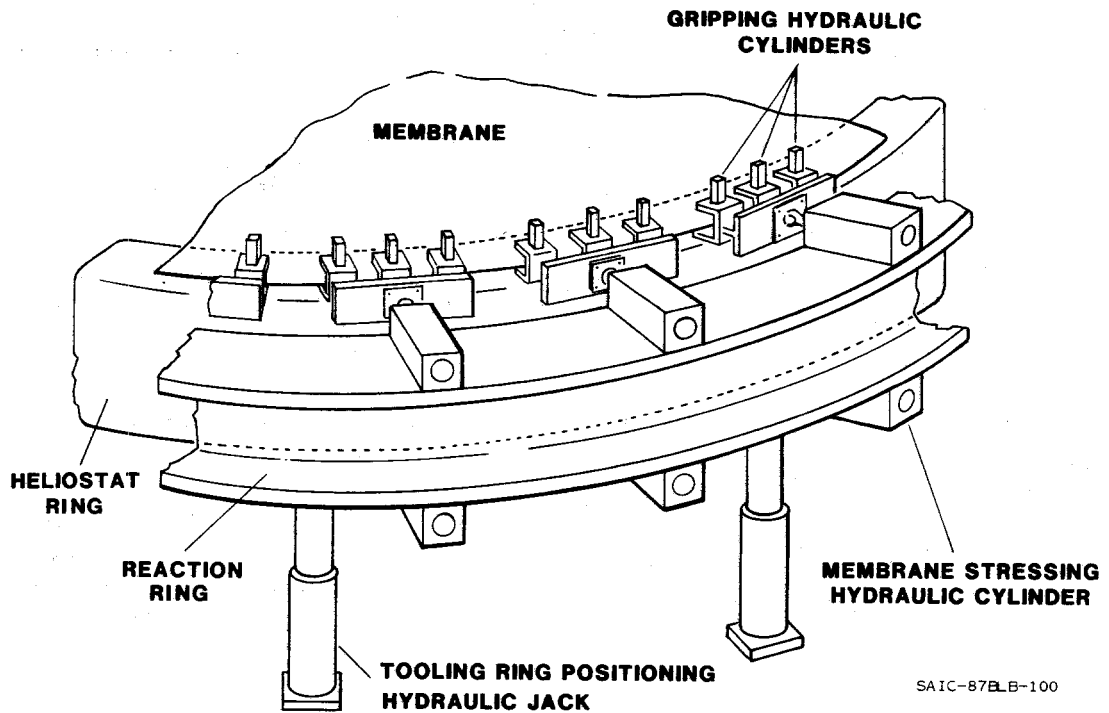
An extensive effort to define a scenario for commercial manufacturing was a part of the first stretched-membrane mirror module development program. In this design improvement program, only scenario adjustments due to design changes were defined. These areas of departure from the first program are described below. The reader is referred to Reference 1 for more detailed information on the manufacturing scenario.

7.1 Assembly of the Mirror Module

The membranes will be welded from coiled stainless steel foil at the central manufacturing facility using a roll-resistance welding process. The reflective film will be laminated to the foil before to welding. Tensioning the membranes at the field site in a commercial manufacturing scenario will be accomplished with a hydraulic tensioning tool as shown in Figure 7.1-1. The reaction ring will be located outside the heliostat ring and is equipped with hydraulic actuators that grip the membranes and tension them to the desired level while simultaneously compressing the heliostat ring. Once the membranes are tensioned, a roll resistance welder will be used to weld the membranes to the ring. A more detailed description of this process is given below.

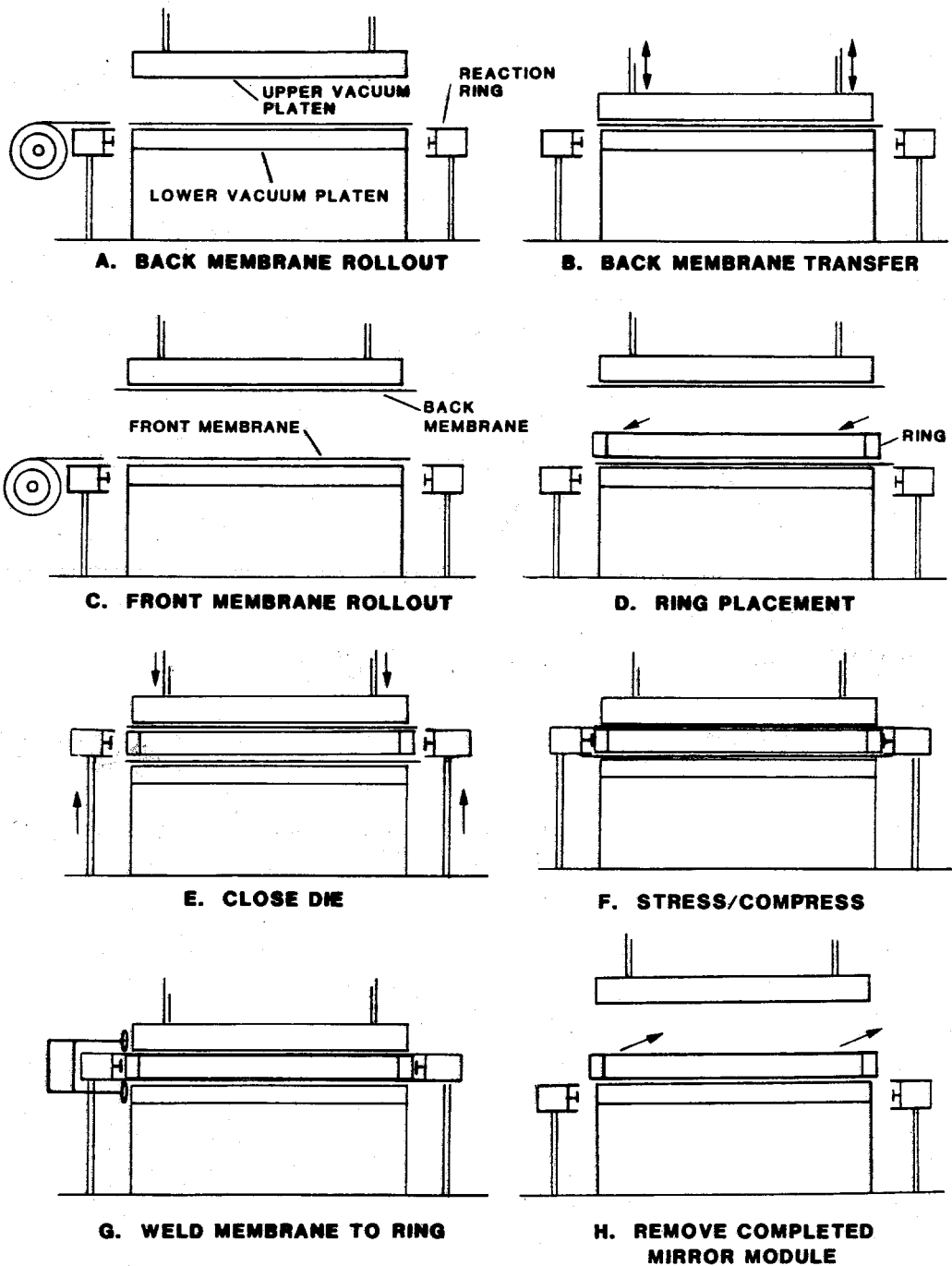
The schematic layout of the tooling and fixturing for the on-site production facility is shown in Figure 7.1-2. The membrane material will be initially stored on large cylindrical rolls. At the central manufacturing facility, the membrane is cut into circular sheets and then taped together at tangent points to facilitate sequential membrane removal from the roll. The reflective membranes will be laminated with ECP-300 silvered polymer film except within 2 in of the outer edge, which is bare stainless steel for welding to the ring. The front and back membranes will be spooled onto separate rolls adjacent to a flat vacuum table. The membranes will be 50 mm (1.97 in) larger in diameter than the outside of the ring on which they will be attached. This space is required for the hydraulic clamps to grip the outside edge of the membrane for pretensioning before to welding.

Once a membrane is positioned and centered on the table, the air vacuum will be drawn. An upper vacuum platen then descends to "kiss" the membrane from above. The upper platen vacuum is activated and the lower platen is switched



SAIC-87LB-100

Figure 7.1-1. Commercial Tooling Concept For Ring Compression and Membrane Tensioning



SAIC-87BLB+102

Figure 7.1-2. Commercial Mirror Module Assembly

off, thus transferring the membrane from the bottom to top platen (Figure 7.1-2B). The upper platen moves up and a second reflectorized membrane is positioned and held using the air vacuum system of the lower platen (Figure 7.1-2C). A ring is now moved in and centered on the lower platen, on top of the front membrane (Figure 7.1-2D). The top platen is lowered to bring the back membrane to rest on the ring (Figure 7.1-2E). At the same time, the reaction ring moves up into position (Figure 7.1-2F).

Next, the ring compression hydraulic cylinders extend to make contact with the ring, and the membrane tensioning hydraulic cylinders extend and the jaws open. When the membrane stressing cylinders are fully extended, the hydraulic jaws close, gripping the membrane. Pre-tension will be applied as the cylinders begin to retract. With the ring constrained in plane by the ring pre-compression cylinders, the membrane vacuum is released. The roll resistance welder then circumnavigates the ring twice, first with a solid-state weld to attach the membrane to the ring. The membrane tension is then released. Next a fusion weld is used to form a continuous joint under no tension (Figure 7.1-2G). Both membranes are welded at the same time.

The tension/compression fixture is then released and lowered to its standby position with all hydraulic cylinders retracted. The excess membrane will be trimmed off and air pressure applied to the lower platen to protect the reflector surface as the completed mirror module is removed from the stressing machine.

The tooling and fixturing for stressing and positioning the membranes must be compatible with the membrane-to-ring welding equipment so that the two can work together to efficiently fabricate a mirror module. Once the mirror module has been fabricated, the tooling and fixturing will be prepared for the next mirror module, while the finished mirror module is transported to another part of the factory for finishing and fitting to the truss support arms and drive mechanism for subsequent installation.

The rings will be manufactured from coil stock. The coil stock is run through a roll bending machine, which rolls and bends the coil stock into a tubular box beam. This tubular box beam has a seam on the center of a long side, which will be roll-resistance welded continuously to close the box beam. From this forming station, a continuous box-beam is fed into a three-point rolling system, which bends the tube into a circle continuously. Rings will be added

to the bottom of what looks like a coil spring. Rings will be cut off of the top, displaced and welded together to form the membrane support rings. The continuous process and tight manufacturing quality control maintains ring circularity and planarity.

7.2 Bench-Scale Model of Membrane Tensioning

A bench-scale model of the commercial tensioning system has been built and tested. A diagram of the commercial tensioning device is shown in Figure 7.2-1. The model consists of a hydraulic power unit that is connected through a series of manual control valves and hydraulic lines to hydraulic cylinders, which grip and tension the membrane while simultaneously compressing the ring. The control valves allow control of pressure, flow rate, and flow direction. A check valve was placed in the path of the grippers to prevent backflow, which could cause the membrane to slip out. The cylinders are attached to a 61-cm (24-in) segment of I-beam, which represents the reaction ring used in the commercial manufacturing scenario. The bench-scale model is shown in Figures 7.2-2 and 7.2-3. Figure 7.2-4 shows a membrane sample under tension in the bench-scale tensioner. The rectangular tube closest to the grippers represents the mirror module ring. The other rectangular tube is part of the fixture to allow one piece of membrane to be wrapped around both the upper and lower grippers. In effect this tube simulates tensioning a small section of a complete mirror module. For the short segment tested, the system proved to be a fast, efficient, and easily controllable method for membrane tensioning. A description of the operating procedure is given in Appendix C.

7.3 Fabrication of the Support Truss

Originally, the support arms for the heliostat were to be shipped prefabricated from the supplier to the field site. The revised design calls for the trusses to be fabricated at the field site. Shipping costs will be reduced due to more compact packing. Two identical and parallel process lines will be used. The truss tubes will be manufactured from coiled low-carbon steel stock. The stock will be leveled, cleaned and sheared to length. The stock will then

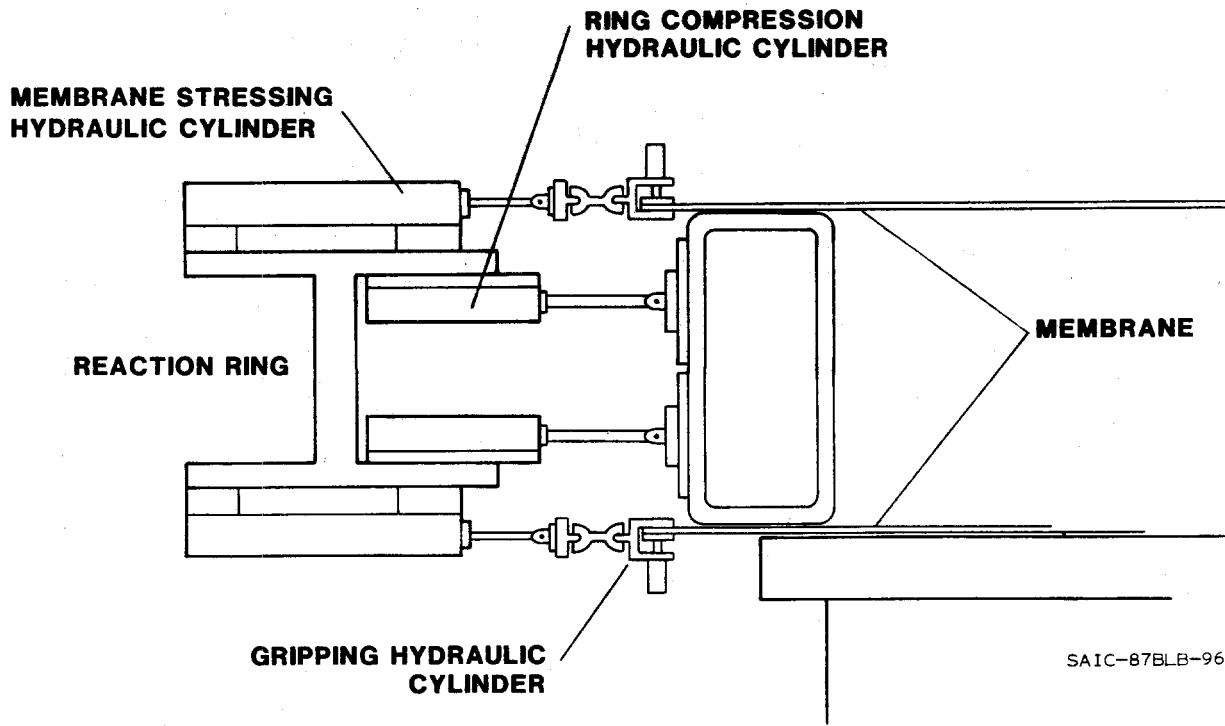


Figure 7.2-1. Commercial Membrane Tensioning System

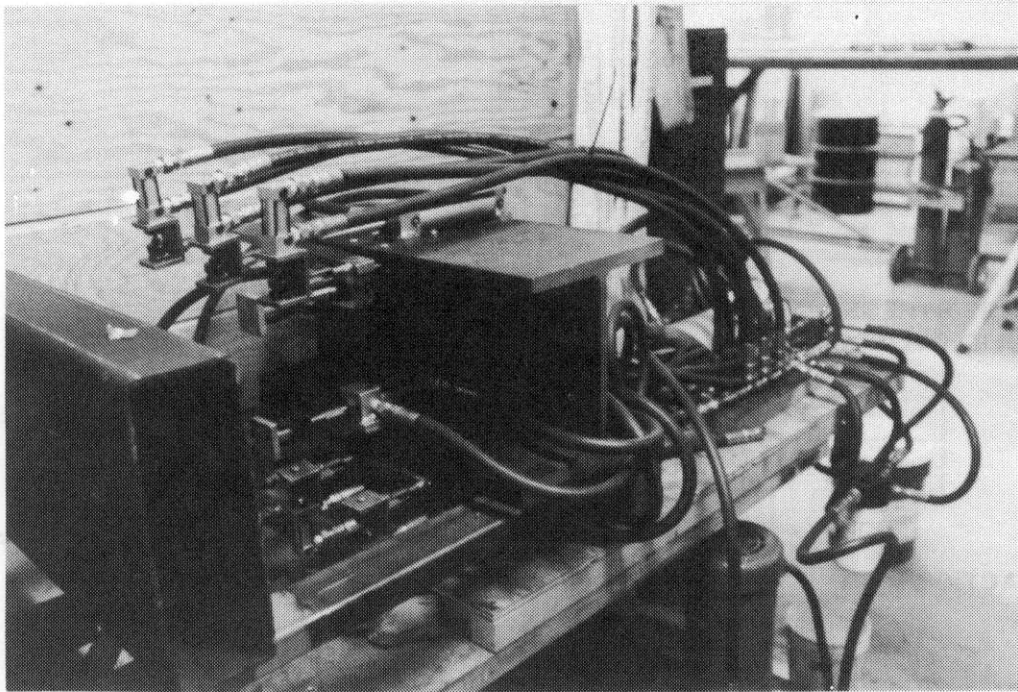


Figure 7.2-2. Hydraulic Tensioning Tool Bench Scale Experiment (View 1)

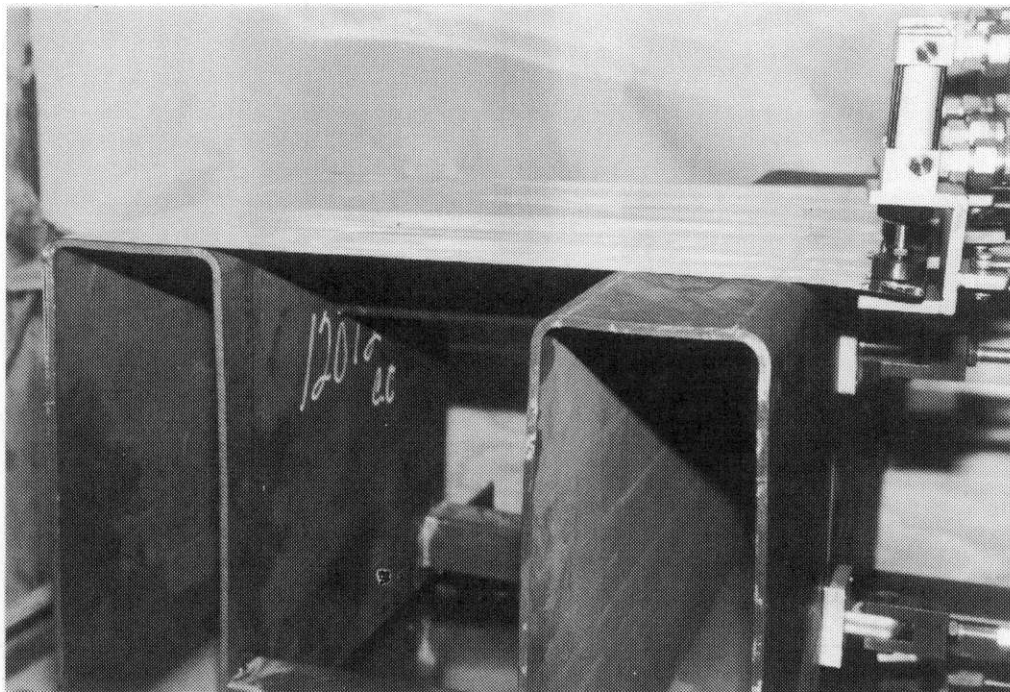


Figure 7.2-3. Hydraulic Tensioning Tool Bench Scale Experiment (View 2)

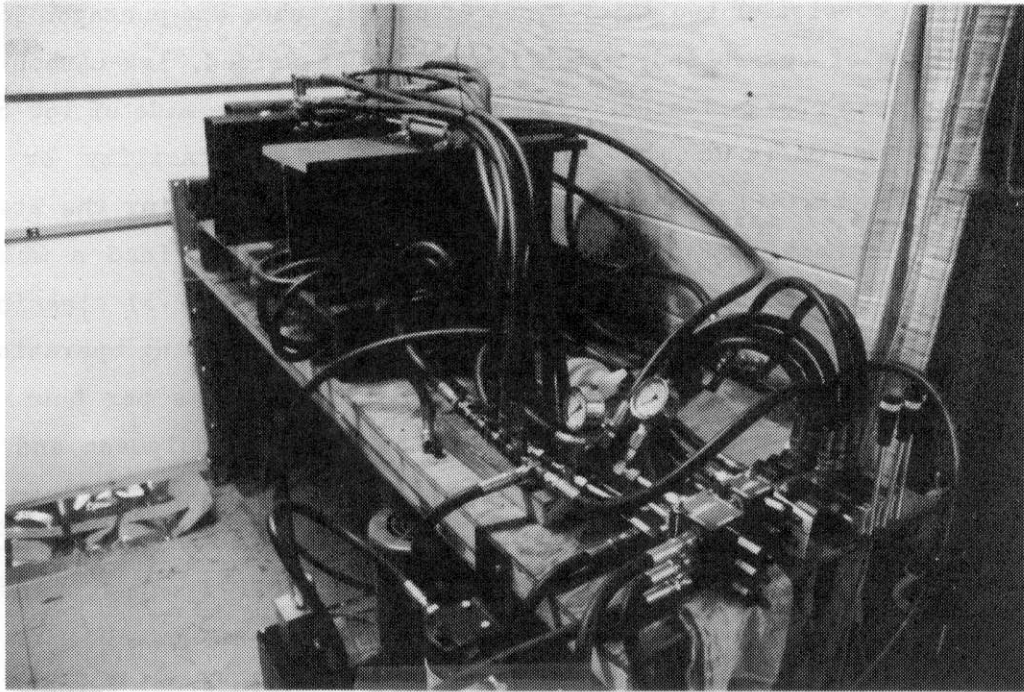


Figure 7.2-4. Membrane Tensioning Tool

be rolled into 3- and 4-in diameter tubes. The truss webbing will be manufactured from low-carbon steel $\frac{1}{2}$ -in wire, which will be bent, positioned and then welded to the tubes by a gang spot welder.

7.4 Hub Production

The hub will consist of two major types of parts; tubes and pentagon joints. The tubes are made of hot-rolled, electric-resistance-welded, low-carbon-steel and will be purchased prefabricated. The pentagon joints are made of low-carbon steel and will be cast at the central manufacturing facility or by a subcontractor. The casting process has several steps; 1) melting the steel in an electric arc furnace (EAF), 2) pouring the molten metal into a mold, 3) solidifying the metal, 4) shaking the casting out of the mold, 5) cleaning the casting, and 6) treating with heat. If only one shift of melting operations is considered, then the EAF must be capable of melting 3.3 tons per hour. The installed capital cost of the EAF with pollution control equipment and water cooling will be approximately \$600,000 [23].

Heat treating will be accomplished using hot isostatic pressing (HIP) to assure the greatest strength of the casting. In the HIP process, parts are subjected to high pressures and temperatures in a pressure vessel. An inert gas is the pressurizing medium, and heat is applied by an internal furnace. The HIP process collapses voids and porosity by creep or plastic deformation. It also diffusion bonds the surfaces of the collapsed areas, creating a casting with a fully dense, homogeneous microstructure [24].

Fabrication of the hub weldment will be accomplished using three welding fixtures; one each for the upper pentagon weldment and the bottom pentagon weldment, and a third for final assembly of the two weldments into one.

Assembly of the tubes and castings is facilitated by the design of the castings, which are basically hollow spheres with short hollow sleeves and solid truss mounting flanges projecting off their surface. The hollow aspect allows the interconnecting tubes to be slid through the sleeves and into the sphere and then back out and into the next casting. The center actuator tube (CAT) has pre-bored tube mounting holes and a large enough I.D. to allow interconnecting tubes to withdraw into its center before final positioning and welding.

The upper pentagon weldment can be fabricated in parallel to the bottom one, since it has its own fixture. First the interconnecting tubes are slid into the upper corner castings (UCC) and the truss mounting flanges are clamped to the fixture and the assembly is welded.

The bottom pentagon weldment is fabricated on a fixture capable of rotating 180° in the horizontal axis and is accomplished by the following steps:

1. Position CAT on welding fixture.
2. Slide bottom spoke tubes through CAT walls.
3. Slide bottom pentagon tubes into bottom corner castings (BCC).
4. Clamp BCWs to welding fixture using truss mounting flanges.
5. Slide bottom spoke tubes into BCWs.
6. Slide inner down tubes through CAT walls and into BCWs.
7. Weld tubes and castings.
8. Position and weld actuator mounting gussets inside CAT.
9. Slide inner up tubes through CAT walls.
10. Slide outer tubes into BCCs.
11. Position and clamp upper pentagon weldment to the bottom pentagon weldment using truss mounting flanges.
12. Rotate weldment fixture 180°.
13. Re-position inner and outer tubes into UCCs and weld.
14. Position and align drum pivot mounting flanges in relation to drum lift pivot flange, clamp and then weld.

7.5 Focus/Defocus Pad Production

The focus/defocus pad was not used in the original design. The required parts will be fabricated out of five thicknesses of low-carbon steel sheets and plates. The smaller mounting and stiffening gussets will be stamped in-house. The larger mounting blocks will also be stamped, but because of their size, the stamping will be done outside. Several fabrication processes were considered for the defocus dishes. The first, a plasma arc cutter, was rejected because the high-quality cutting was not felt to be necessary, and therefore this technology was considered to be too expensive. The second option was an automated oxy-acetylene torch, a large gantry-type two-axis machine on a table.

The third option considered was a two-stage stamping process. In the first stage, holes are punched and the perimeter cut, and in the second stage the plate spins and angles the edges. The stamping option was determined to be the most cost-effective, and it was decided these parts would be purchased prefabricated. An alternate design utilizes honeycomb sandwich material for the pads.

To fabricate the defocus rings, carbon steel coil stock will be cut to size, fed into a roll former, welded and then fed into a second roll former to make two half-rings of the tubing, which will be welded together.

7.6 Focus-Control System

The original design used an optical detector system to provide signals for the actuation of a pressure vacuum pump system. The revised design uses an LVDT membrane-position detection system to drive an actuator that moves the back membrane in and out. The mounting of the detection system is on one of the lower trusses, 4 ft from the ring. The revised design requires manufacture of a control logic board, which will be done at the central manufacturing facility. Assembly of the logic board and the power supply into the control box will also take place at the central manufacturing facility. The control box will be purchased prefabricated. The actuator and motor will be mounted inside the hub at the site.

7.7 Finishing

All of the exposed parts of the heliostat, except the stainless steel membrane, must be finished. Most of the metal part surfaces will be contaminated with lubricating oils, greases and waxes, metal particles, or casting sand, in addition to general dirt from the workplace. In addition, there may be burrs, laps, flash, and other surface defects present. Several surface preparation techniques could be used. Mechanical methods can be used to remove unwanted metal. Mass finishing, probably barrel finishing, of the small parts will be done. For larger and more complex parts, brushing and grinding are two techniques that will be used. If the part is to be painted, oils and greases from other fabrication processes will be removed using solvent cleaning. If

plating is to be done, alkaline soak cleaners in addition to acid dipping will be used. If it is a cast part, chemical descaling will also be used. To accomplish this, larger parts will be automatically dipped using an overhead conveyer with fixtures.

Once the metal surfaces have been cleaned and prepared, the coating or plating will be done. For parts to be painted, electrostatic spraying or electropainting will be used to apply the paint. Electrostatic spraying is especially useful for complex parts because it is not line-of-site limited. The parts are moved from the surface preparation area on the conveyer to the surface modification area. The parts to be coated must be heated above the melting point of the powder to fuse the paint to the surface of the workpiece. This can be done by preheating the substrate prior to spraying or by heating the coated part after spraying. Finally, the parts are stripped from the fixtures.

For electropainting, in which charged molecules in solution are moved along a voltage gradient toward the substrate to be coated, discharged, and incorporated into the coating, the parts are moved through rectangular steel tanks automatically with the overhead conveyer system. The electropainting bath consists of the solvent, the organic group, inorganic solids and an organic pigment. The parts are stripped from the fixtures after coating and rinsing.

For electroplating, parts will be placed in plating tanks automatically, using programmed overhead conveyers carrying fixtures for larger parts and barrels, which are agitated to separate the parts, for smaller parts.

Transformer/rectifier sets will be used to supply the low-voltage direct current needed. Parts will be dipped in a rinse tank following the plating tank and then stripped from the fixtures [25]. A third method, hot dipping, can also be used to provide corrosion resistance. Parts can be processed in batch or, for the wire, continuously. Again, small parts may be coated in a barrel fixture and agitated and larger parts carried on an overhead conveyer system.

Depending on the location of the finishing facility (ies), both OSHA and EPA regulations will have to be considered. These regulations could present a problem for wet painting or for galvanizing. Location would also affect the decision as to whether the corrosion prevention work could be performed outside the heliostat manufacturing and assembling facilities. Location in an area where a significant amount of aerospace work is performed would make plating a viable

option, since this is often subcontracted out to jobshops in the aerospace industry. Location in an area where automotive production is significant would make subcontracting to a jobshop that uses spray-painting robots a viable alternative.

7.8 Transportation

Transportation to the site will still be by conventional tractor-trailer truck; however, the required number of trucks has changed because of the changes in the design. Table 7.8-1 shows the loading per truck for each part that was redesigned. The membranes, rings, and pedestal and drive loading will remain the same.

Based on the requirement to manufacture 16 units per day at each of 12 sites, the required number of trucks will be 40. In addition, at each site a truck is needed for moving trailers around, and therefore 12 additional trucks will be required, for a total of 52 trucks. For each truck on the road, three trailers are required so that at all times, one trailer is on the road, one trailer is being unloaded at the site, and one trailer is being loaded at the central facility.

7.9 Operation And Maintenance

Due primarily to the change in design of the focus-control system, the operation and maintenance requirements have changed. The number of motors remains at four, the two vacuum cleaner blower motors having been replaced by the two actuator motors (vent valve and linear actuator). The LVDT detection system replaces the optical detection system; however, both use standard electronic components. Again a spare package would be available at the site so that it could be interchanged for a unit requiring servicing.

The defocus bladder is no longer a part of the design, and therefore will not require servicing or replacement.

Table 7.8-1 Transportation

- o TRUSSES
 - 52,000 lbs of trusses per truck
 - 24 truss structures per truck load
 - 1.5 day supply per truck

- o HUBS
 - 52,000 lbs of castings/pipes
 - 77 hubs per truck load
 - 4.8 day supply per truck

- o FOCUS PAD/ACTUATOR
 - 52,000 lbs of focus pads/actuators per truck
 - 98 pad/actuators per truck load
 - 6.1 day supply per truck

The heliostat trucking load was revised as shown in Table 7.8-2.

Table 7.8-2 Heliostat Trucking Load

	TRUCKS/COMPONENT
MEMBRANES	0.016
RINGS	0.025
FOCUS PAD	0.01
TRUSS	0.042
PEDESTALS	0.100
HUBS	0.013
TOTAL TRUCKS/HELIOSTAT	0.206

8.0 COST OF THE COMMERCIAL HELIOSTAT

In the process of designing the improved commercial-size mirror module, a detailed parts list was developed. Vendors were then contacted to determine the cost of the components based on a production rate of 50,000 units per year. The material and labor cost data were then aggregated to determine the total cost of a 150-m² commercially manufactured heliostat. A summary of the cost analysis is shown in Table 8.0-1. A commercial-size mirror module was assumed to be mounted on a Peerless-Winsmith low-cost drive. Heliostat costs are shown in the table for two reflective film cost scenarios. The low-cost reflector data shown in the first column are for a reflective film cost of \$5.38/m² (\$.50/ft²). The high-cost reflector data shown in the second column are for a reflective film cost of \$16.14/m² (\$1.50/ft²). The costs shown do not reflect any film replacement that might be required throughout the life of the heliostat. All other costs for fabrication and installation of a complete heliostat, including profit/taxes, are included. The selling price of the installed heliostat based on the low-cost reflector is \$70.80 per m², and on the high-cost reflector, \$85.90 per m². A breakdown of the materials cost for the mirror module is shown in Table 8.0-2.

8.1 Cost Modifications

The cost of the installed heliostat has been affected by changes in design from the first-generation module, which required changes in capital equipment purchases, labor requirements and material cost.

Direct labor requirements were also affected by the change in design of the heliostat. Table 8.1-1 shows the new requirements for direct labor at the central manufacturing facility. The total number of personnel is 151. Changes to the direct labor requirements at the field site are shown in Table 8.1-2. The revised total personnel requirement is 50.

The total labor cost for the central manufacturing facility and all field sites is shown in Table 8.1-3. The total labor cost per heliostat is \$862.78, of which \$251.26 is for CMF labor and \$611.52 is for field site labor.

Table 8.0-1 150-m² Second-Generation Commercial Stretched
Membrane Heliostat Cost*

	Low Cost Reflector		High Cost Reflector	
	(\$)	(\$/m ²)	(\$)	(\$/m ²)
Mirror Module & Support				
Structure	5,146.45	34.31	7,034.02	46.89
Materials	4,357.33	29.05	6,244.90	41.63
Labor	611.52	3.97	611.52	3.97
Equipment (Including Interest)	157.66	1.02	157.66	1.02
Consumables	9.94	0.13	19.94	0.13
Drive & Pedestal	2,067.00	13.42	1,067.00	13.42
Drive Assembly	1,694.00	11.00	1,694.00	11.00
Pedestal	266.00	1.74	266.00	1.74
Assembly Drive/Pedestal /Electric	107.00	0.69	107.00	0.69
Foundation	934.00	6.06	934.00	6.06
Labor (Field Site)	251.26	1.63	251.26	1.63
Buildings (Including Interest)	16.95	0.11	16.95	0.11
Field Wiring	<u>434.00</u>	<u>2.82</u>	<u>434.00</u>	<u>2.82</u>
Total Heliostat Cost	8,849.66	59.00	10,737.23	71.58
ROI & Taxes @ 20%	<u>1,769.93</u>	<u>11.80</u>	<u>2,147.45</u>	<u>14.32</u>
Selling Price	10,620.00	70.80	12,885.00	85.90

*50,000 Units/Year, 12,500th Unit Produced, 1988\$

**Table 8.0-2 Commercial Stretched-Membrane Mirror Module
Cost Analysis**

DESCRIPTION	COST/UNIT (\$)	NO. OF UNITS	TOTAL COST (\$)
FRONT MEMBRANE (1)	2.242	236.47 LB	530.17
RING FRAME	0.265	1083.85 LB	287.22
LVDT		1	133.68
POWER SUPPLY	27.720	1	27.72
BACK MEMBRANE (1)	2.419	236.47 LB	572.03
MIRROR MOUNTING TRUNION	0.255	103.57 LB	26.41
TRUSS/MIRROR MTG GUSSET	0.255	102.6 LB	26.16
DOUBLER PLATE	0.255	37.5 LB	9.56
MOUNTING HARDWARE	0.255	16.0 LB	4.08
TRUSS TUBES - 3 INCH	1.400	230.0 FT	322.00
TRUSS TUBES - 4 INCH	1.900	115.0 FT	218.50
TRUSS WIRE - 1/2 INCH	0.220	850.87 LB	187.19
HUB TUBE - 3 INCH - 0.120 WALL	4.450	188.01 LB	836.64
HUB TUBE - 4 INCH - 0.120 WALL	8.350	13.27 LB	110.80
HUB TUBE - 4 INCH - 10GA	6.19	61.42 LB	380.19
HUB TUBE - 11 INCH	8.350	77.10 LB	643.74
HUB TOP PENTAGON JOINT	15.000	5	75.00
HUB BOTTOM PENTAGON JOINT	20.000	5	100.00
FOCUS PAD HONEYCOMB	0.477	30.67 LB	14.63
FOCUS PAD CENTER RING	0.265	18.68 LB	4.95
FOCUS PAD CENTER PAD	0.265	51.8 LB	13.73
FOCUS PAD INNER RING	0.277	17.88 LB	4.95
FOCUS PAD OUTER RING	0.284	25.43 LB	7.22
MEMBRANE/FOCUS INNER/OUTER RINGS	2.000	2	4.00
POD/FOCUS PAD STIFFENING GUSSETS	0.265	20.14 LB	5.34
POD DISH	0.277	130.67 LB	36.20
POD CENTER PAD	0.265	51.8 LB	13.73
POD CENTER RING	0.265	18.68 LB	4.95
ACTUATOR	350.000	1	350.00
ACTUATOR MOUNTING BLOCK	0.260	2.67 LB	0.69
ACTUATOR MOUNTING GUSSET	0.265	1.86 LB	0.49
ACTUATOR STIFFENING GUSSET	0.265	20.14 LB	5.34
DAMPER VALVE	74.280	1	74.28
VALVE MOUNTING SPOOL	0.265	12.34 LB	3.27
PINS/BASE OF TRUSS TO HUB	0.255	6.4 LB	1.63
CONTROL BOX	25.000	1	25.00
LOGIC CIRCUIT BOARD	71.57	1	71.57
CONTROL POWER SUPPLY	25.000	1	25.00
REFLECTOR (1)	1.500	603.33	904.99
TOTAL COST			6244.90

NOTE:

(1) ASSUMING 88% UTILIZATION OF MATERIAL

Table 8.1-1 Direct Labor Central Manufacturing Facility

Membrane Manufacture	-Production Manager	1
	Crew Chiefs	4
	Reflector Operators	5
	Seaming Operators	30
	Total	40
Actuator Assembly	-Production Manager	1
	Crew Chiefs	2
	Assembly Technicians	12
	Total	15
Control Logic Board	-Production Manager	1
	Section Heads	2
	Electronic Assemblers	11
	Total	14
Support Arm Hardware	-Production Manager	1
	Crew Chiefs	1
	Welders	3
	Assembly Technicians	3
	Total	7
Production Machining and Equipment Maintenance	-Production Manager	1
	Shop Foreman	1
	Maintenance Foreman	1
	Machinists	10
	Maintenance Specialists	10
	Total	23
Shipping and Receiving	-Transportation Manager	1
	Dispatcher	1
	Drivers	40
	Dock Men	5
	Warehouse Men	5
	Total	52
	GRAND TOTAL	151

Table 8.1-2 Direct Labor Field Site

Ring Rolling

Crew Chief	1
Rolling Technicians	3
Welding Technicians	2
Total	6

Membrane Attachment

Crew Chief	1
Membrane Handling Technicians	4
Handling Technicians	2
Total	7

Focus Control Installation

Technicians	8
Total	8

Support Arm Attachment and Checkout

Quality Engineer	1
Technicians	2
Inspectors	2
Module Handler	1
Total	6

Support Arm Bending and Welding

Crew Chief	1
Welding Technicians	2
Bending Technicians	2
Rolling Technicians	2
Total	7

Hub

Crew Chief	1
Welding Technicians	3
Casting Technicians	2
Total	6

Field Installation and Checkout

Field Engineer	1
Transportation Driver	1
Crane Operator	1
Mill Wrights	2
Electrical Technician	1
Mechanical Technicians	2
Alignment Technician	1
Checkout Engineer	1
Total	10

GRAND TOTAL 50

Table 8.1-3 Total Labor Per Heliostat

151 Staff CMF (Inc. Truckers)	\$40.00 Loaded Labor Hr @ 2080 Hours/year	12,563K
490 Staff Field Sites	\$30.00 Loaded Labor Hr	30,576K
TOTAL		43,139K
Labor/Heliostat @ 50,000 units/year		\$862.78

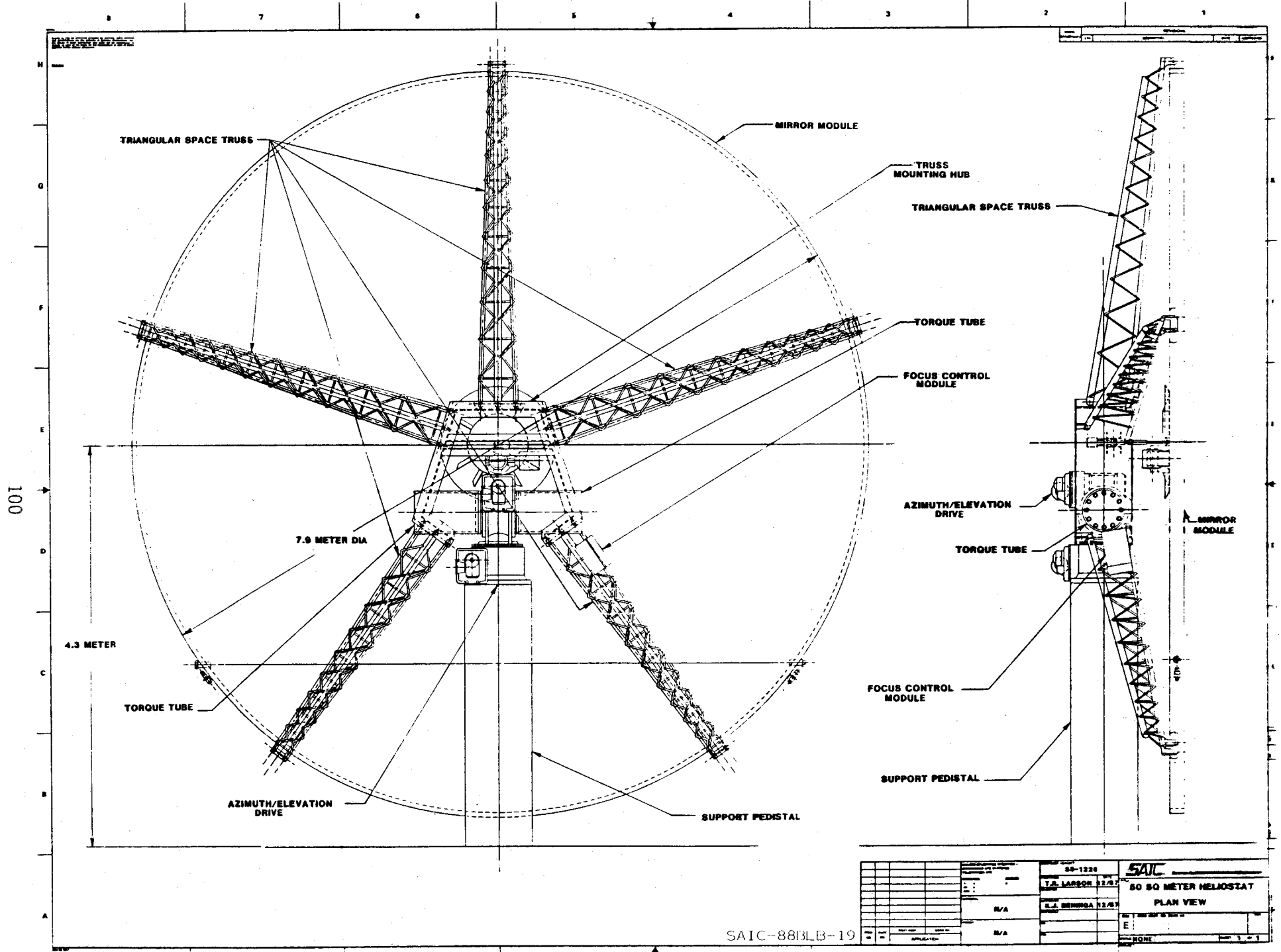
9.0 DESCRIPTION OF THE IMPROVED PROTOTYPE MIRROR MODULE

Following the design of the 150-m² commercial mirror module, a 50-m² prototype mirror module was designed and fabricated. A drawing of the prototype mirror module mounted on the Advanced Thermal Systems (ATS) torque tube drive is shown in Figure 9.0-1, and the specifications for the prototype mirror module are shown in Table 9.0-1. The prototype design replicates the commercial mirror module design to the extent that it is feasible. A photograph of the heliostat is shown in Figure 9.0-2.

The support ring for the prototype module has a 7.9-m (26.0-ft) inside diameter with cross-sectional dimensions of 5.10-cm by 15.2-cm (2-in by 6-in). The membranes are fabricated from 14 strips of 61.0-cm (24-in) wide 304 stainless steel, each of which is .0762 mm (.003 in) thick. ECP-300 reflective film is laminated to the front membrane of the module. Five support trusses radiate from a central hub for support of the ring, as shown in Figure 9.0-3. The support truss design incorporates a triangular cross-section to provide both in-plane and out-of-plane support for the ring. The prototype truss design is shown in Figure 9.0-4.

The prototype truss hub design deviates from the commercial design because the prototype hub must adapt to an ATS torque tube-type heliostat drive. Therefore, the prototype hub is considerably different in design. A drawing of the prototype hub design is shown in Figure 9.0-5. The hub is fabricated from 53.-cm (21-in) steel I-beam, which is welded together in an asymmetric pentagonal pattern. A truss is mounted to each side of the structure. Two sections of 10.2-cm (4-in) steel channel bisect the hub and are used for mounting the focus control linear actuator. Two sections of 25.4-cm (10-in) diameter tubing welded to 40.6-cm (16-in) diameter flanges on one end are used for adaptation of the hub to the ATS torque tube drive system.

The arrangement for mounting the base of the truss to the hub is shown in Figure 9.0-6. Mounting fasteners with free rotation in all directions were used for attaching the truss base to the hub. With this arrangement, adjustment of the position of the truss tip is possible in all directions, in order to attain good alignment with the truss-to-ring attachment brackets. The truss-to-hub mounting arrangement shown effectively produces a pinned connection at each



29-1224		SAIC	
T.A. LARSON 12/87		50 SQ METER HELIOSTAT	
E.A. BENNING 12/87		PLAN VIEW	
E:		E:	
NONE		NONE	

SAIC-88BLB-19

Figure 9.0-1. 50-m² Prototype Heliostat Plan View

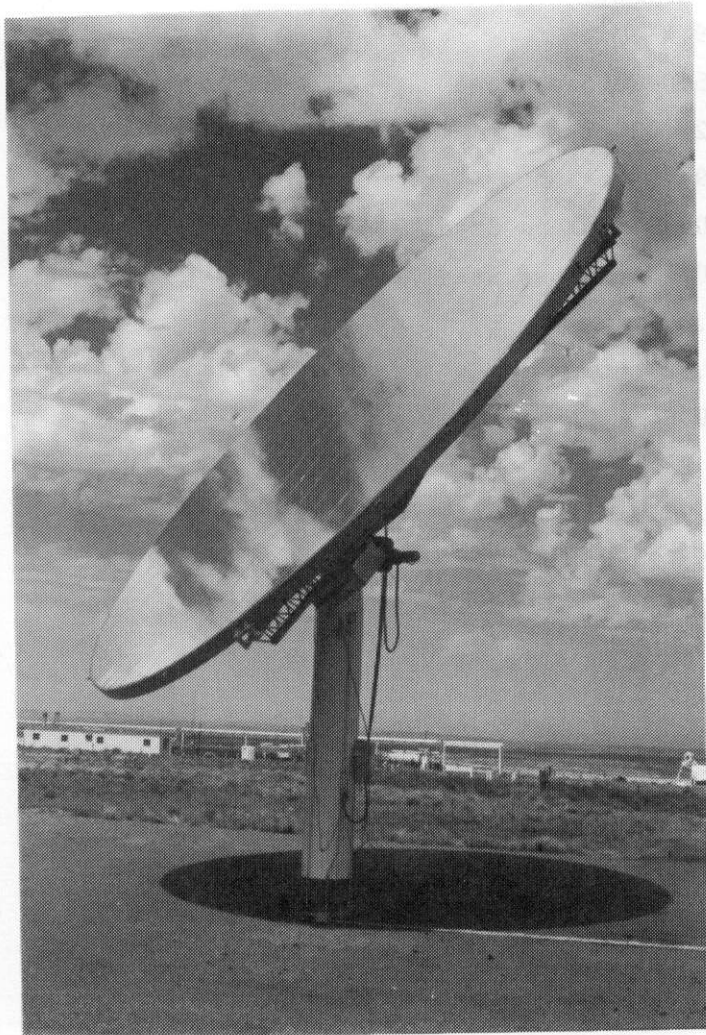


Figure 9.0-2. Prototype Heliostat
Front View

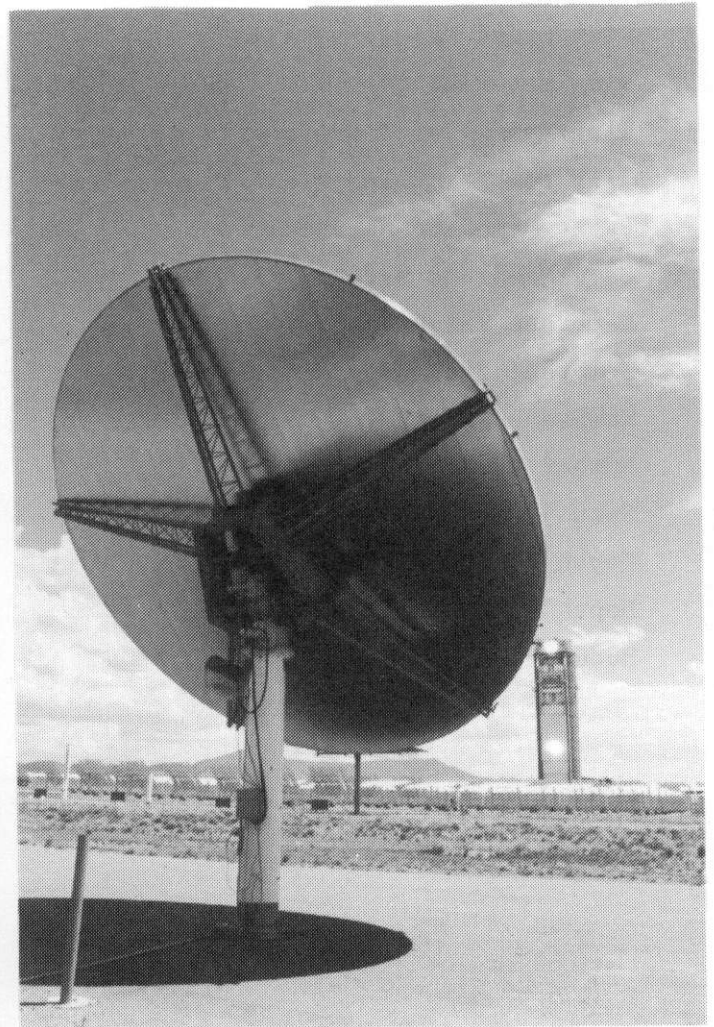


Figure 9.0-3. Prototype Heliostat
Back View

Table 9.0-1. Prototype Heliostat Specifications

Heliostat Diameter	7.92 m	(26 ft)
Area	49.3 m ²	(530.9 ft ²)
Reflective Area	47.74 m ²	(514 ft ²)
Support Ring Cross Section	5.08 cm x 15.24 cm	(2 in x 6 in)
Ring Wall Thickness	0.478	(0.188 in)
Ring Cross Sectional Area	19.4 cm ²	(3.00 in ²)
Ring Material	A500 Carbon Steel	A500 Carbon Steel
Ring Moment of Inertia - I _x	426.02 cm ⁴	(11.1 in ⁴)
Ring Moment of Inertia - I _y	79.08 cm ⁴	(1.90 in ⁴)
Front Membrane Material	304 Stainless Steel - Annealed	
Back Membrane Material	304 Stainless Steel - ½ Hard	
Membrane Thickness	0.008 cm	(0.003 in)
Membrane Preload	6.829 nt/mm	(39 lbs/in)
Membrane Stress	89.64 m Pa	(13000 psi)
Number of Ring Supports	5 Each	5 Each
Span	3.96 m	(13 ft)
Depth of Support at Hub	45.72 cm	(18 in)
Depth of Support at Ring	22.86 cm	(9 in)
Modulation Pad Diameter	1.22 m	(4 ft)

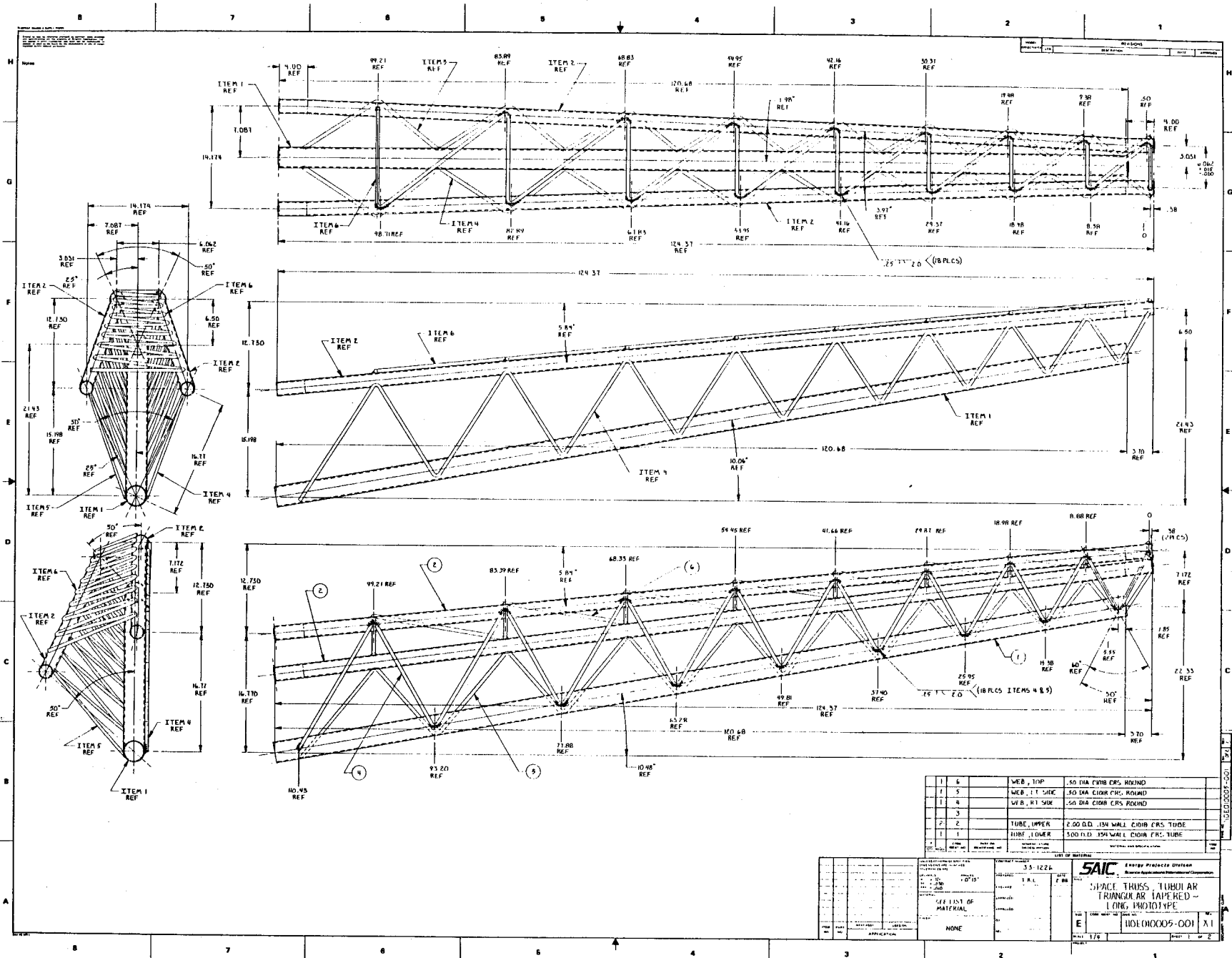
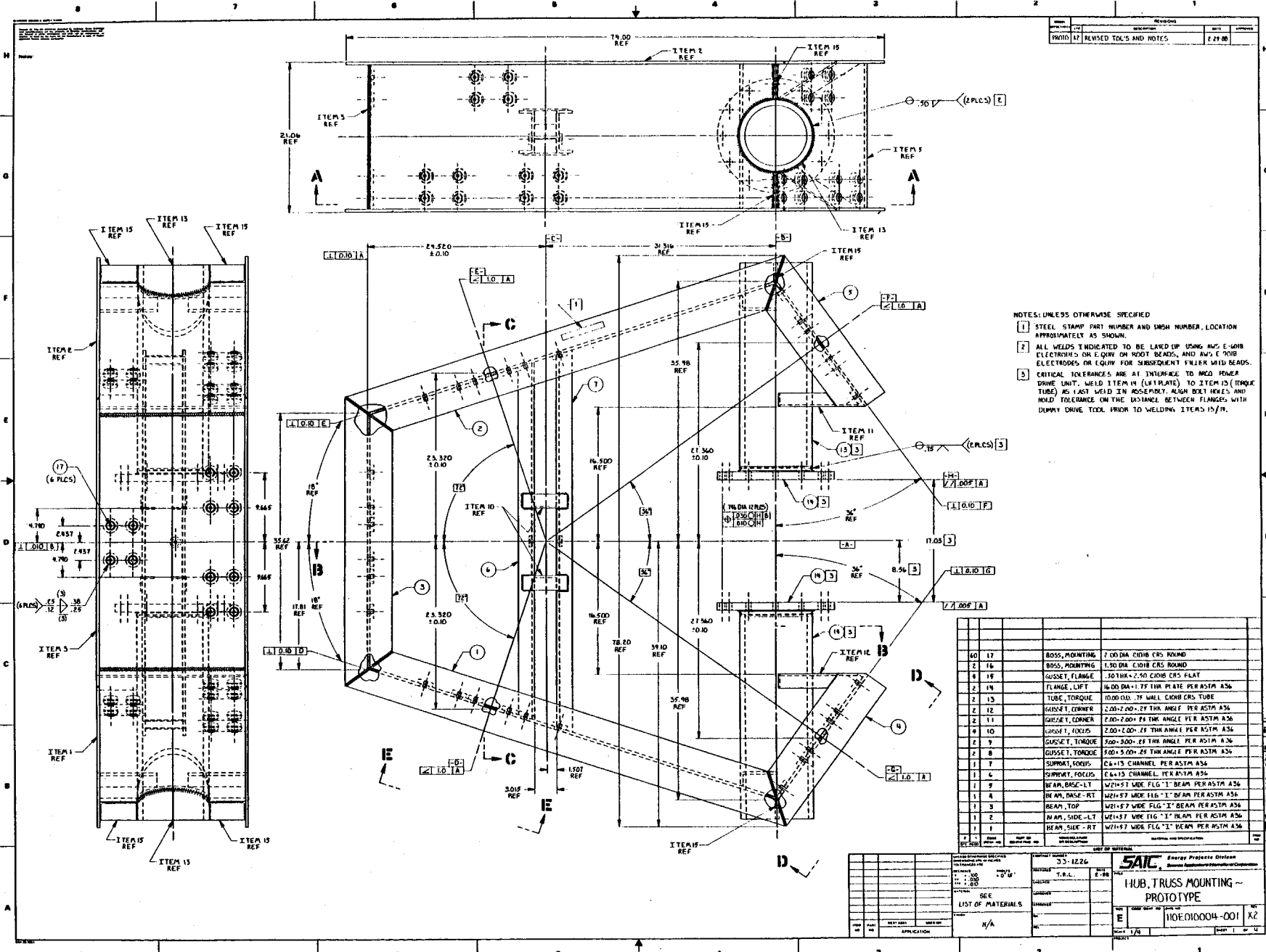


Figure 9.0-4. Prototype Triangular Tapered Space Truss



NOTES: UNLESS OTHERWISE SPECIFIED

- 1 STEEL STAMP PART NUMBER AND DIMS NUMBER, LOCATION APPROPRIATELY AS SHOWN.
- 2 ALL WELDS INDICATED TO BE LAID UP USING A/C E-7018 ELECTRODES OR E-7018 ON ROOT BEADS, AND A/C E-7018 ELECTRODES OR E-7018 FOR SUBSEQUENT FULLER WELD BEADS.
- 3 CRITICAL TOLERANCES ARE AT INTERFACE TO WELD POWER DRIVE UNIT. WELD ITEM 14 (LIFT PLATE) TO ITEM 12 (TORQUE TUBE) AS LAST WELD IN ASSEMBLY. ALIGN BOLT HOLES AND HOLE TOLERANCE ON THE DASHED BETWEEN FLANGES WITH DUMMY DRIVE TOOL PRIOR TO WELDING ITEMS 15/17.

ITEM	DESCRIPTION	QUANTITY	UNIT	REMARKS
10	17			BOSS, MOUNTING 7.00 DIA C1018 CRS ROUND
11	16			BOSS, MOUNTING 1.30 DIA C1018 CRS ROUND
12	18			GUSSET, FLANGE .30 THK x 2.50 C1018 CRS FLAT
13	14			FLANGE, LIFT 16.00 DIA x 1.75 THK PLATE PER ASTM A36
14	13			TUBE, TORQUE 10000 O.D. .75 WALL C1018 CRS TUBE
15	12			GUSSET, CORNER 2.00 x 2.00 x .25 THK ANGLE PER ASTM A36
16	11			GUSSET, CORNER 2.00 x 2.00 x .25 THK ANGLE PER ASTM A36
17	10			GUSSET, FOCUS 2.00 x 2.00 x .25 THK ANGLE PER ASTM A36
18	9			GUSSET, TORQUE 2.00 x 2.00 x .25 THK ANGLE PER ASTM A36
19	8			GUSSET, TORQUE 2.00 x 2.00 x .25 THK ANGLE PER ASTM A36
20	7			SUPPORT, FOCUS C x 15 CHANNEL PER ASTM A36
21	6			SUPPORT, FOCUS C x 15 CHANNEL PER ASTM A36
22	5			BEAM, BASE-LT W21 x 57 WIDE FLG 1" BEAM PER ASTM A36
23	4			BEAM, BASE-RT W21 x 57 WIDE FLG 1" BEAM PER ASTM A36
24	3			BEAM, TOP W16 x 57 WIDE FLG 1" BEAM PER ASTM A36
25	2			BEAM, SIDE-LT W16 x 57 WIDE FLG 1" BEAM PER ASTM A36
26	1			BEAM, SIDE-RT W16 x 57 WIDE FLG 1" BEAM PER ASTM A36

Figure 9.0-5. Prototype Truss Mounting Hub

attachment of the truss leg to the hub. The pinned connection to the hub was shown to have the same stiffness as a cantilever welded connection to the hub through finite-element analysis. This is possible because the three-point truss base support was used rather than a two-point base support, as with a planer truss. A photograph of the hub after installation of the mirror module is shown in Figure 9.0-7.

Also visible in Figure 9.0-7 is the round focus/defocus pad used for adjusting the focal length of the mirror module. The pad is attached to a linear actuator, which modulates the position of the pad and the center of the back membrane. A cross-sectional drawing of the arrangement of the pad attachment to the membrane is shown in Figure 9.0-8. The back membrane of the mirror module is sandwiched between two discs of aluminum honeycombed material. An aluminum ring is located around the perimeter of each of the aluminum honeycombed discs. The refocusing valve is mounted on the exterior of the rear focus pad and is attached to a 15.2-cm (6-in) PVC pipe, which penetrates the defocus pads and the membrane.

The focus-control electronics box is mounted on the lower left truss of the mirror module and contains the power supplies and electronic circuit boards for receiving the position signal from the LVDT and sending the control signal to the linear actuator. The LVDT is also mounted on the lower left truss, 1.22 m (4 ft) from the edge of the mirror module. The LVDT penetrates the back membrane and contacts the front membrane to determine the position and, therefore, focal length of the front membrane. The mirror module finite-element model was used to determine the error in the LVDT position signal, which is possible due to deflection of the tip of the truss. The analysis showed that the possible membrane position error was less than .25 mm (0.01 in) at a wind speed of 12.1 m/s (27 mph). A single 110-volt power line is required to power the focus-control system.

Focus-control parameters are downloaded from the main computer in the control tower to the on-board mirror module computer via an RS422 serial communications line. The logic for the closed-loop system is software-based so that parameters controlling the operating characteristics of the mirror module can be modified from the remote computer. This allows focus-control system

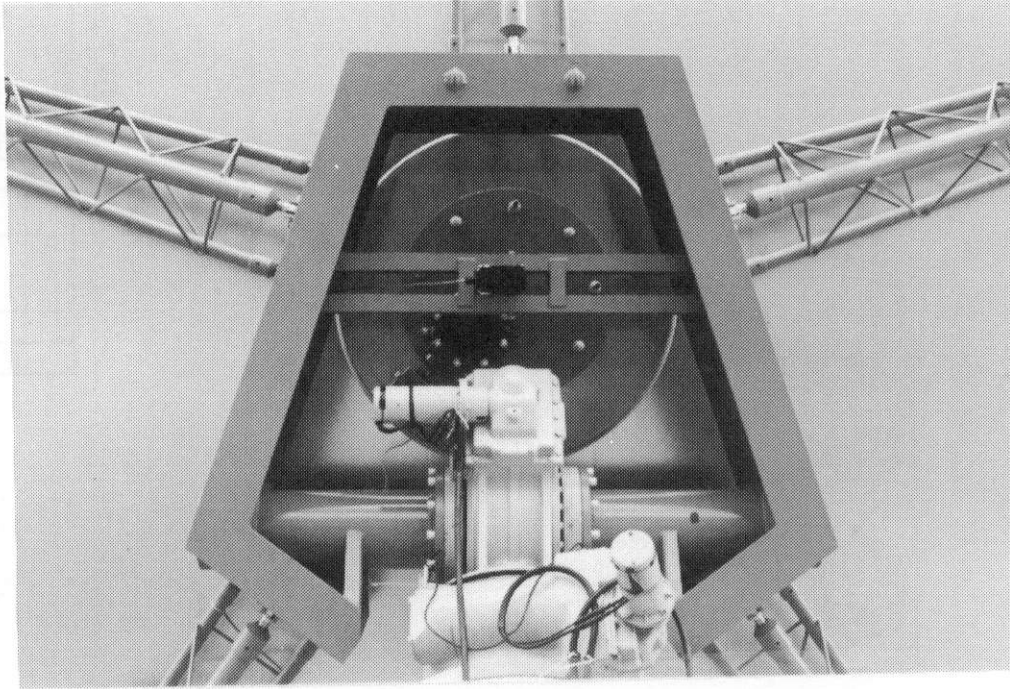
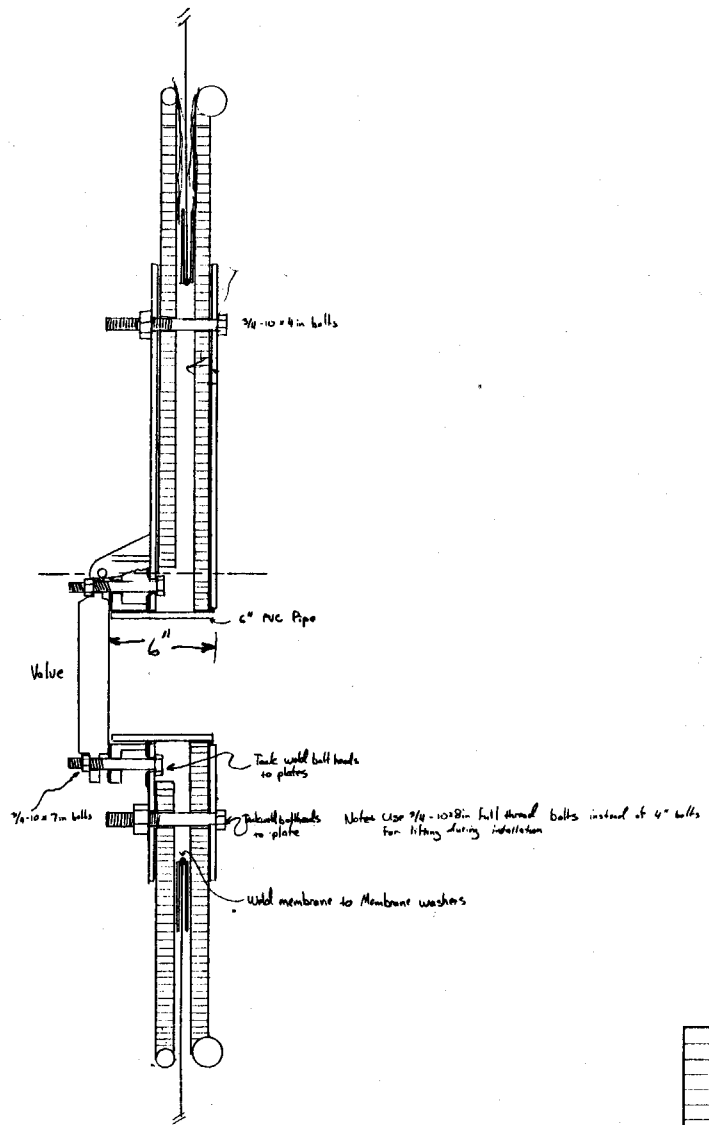


Figure 9.0-7. Installed Hub and Focus Pad

Check all dimensions against the drawing and make any necessary corrections. The drawing is the master and the model is the slave. The model must conform to the drawing.

MODEL EFFECTIVITY		REVISIONS			
REV	DATE	DESCRIPTION	DATE	APPROVED	



108

QTY	CODE	PART OR IDENTIFYING NO	NOMENCLATURE OR DESCRIPTION	MATERIAL AND SPECIFICATION	ITEM NO
LIST OF MATERIAL					
UNLESS OTHERWISE SPECIFIED DIMENSIONS ARE IN INCHES TOLERANCES ARE			CONTRACT NUMBER 33-1226		
DECIMALS	ANGLES		PREPARED K. Berings	DATE 3/12/68	TITLE FOCUS PAD ASSEMBLY
FRACTIONS			CHECKED		
MATERIAL:			APPROVED		
FINISH:			APPROVED		
APPLICATION:			OR		
ITEM NO	PART NO	HEAT ASBY	USED ON	SCALE 1/3	REV
APPLICATION			REL		

SAIC Energy Projects Division
Science Applications International Corporation

Figure 9.0-8. Prototype Focus Control Pad Assembly

optimization based on operational data and experience without requiring changes in hardware.

As with the commercial-size design, a set of design criteria was developed for the prototype design. These criteria included an additional safety factor in areas of uncertainty in the design. The design criteria for the prototype mirror module are shown in Appendix A. Considerable effort has been devoted to development of tooling to produce extremely flat membranes and mirror module rings. The stainless steel foil used for the prototype has been flattened with a proprietary process by the supplier. The ring circularity and out-of-plane tolerances were checked with a laser measurement system at the ring rollers facility prior to acceptance of the rings.

A finite-element model of the prototype mirror module was also developed to verify the design. The finite-element modeling techniques were the same as those used in the commercial mirror module analysis. The model was scaled down to reflect the prototype module size, and the prototype hub was modeled. The structural components of the mirror module were sized using this finite element analysis. A summary of the results of the prototype mirror module structural analysis is given in Section 11.0.

10.0 COMMERCIAL-PROTOTYPE MIRROR MODULE COMPARISON

A significant effort was devoted to designing the prototype mirror module to be a scaled-down version of the commercial-size mirror module. This effort was successful in most areas. However, there were a few areas in which deviation from the commercial design was necessary. A comparison of the specifications for the commercial and prototype mirror modules is shown in Table 10.0-1.

The most visibly obvious deviation in design is the central hub structure used for mounting the ring support trusses and adaptating of the mirror module to the drive system. This deviation was necessary in order to adapt to Advanced Thermal System's (ATS) torque-tube-type drive system, rather than the elevation jack-screw-type drive, which was assumed in the commercial design. The I-beam pentagonal structure used for the prototype provides a solid surface for mounting the hub to the torque tubes. An offset of the elevation drive from the center of the mirror module was necessary to allow clearance for the focus-control linear actuator, which had to be mounted directly in the center of the back membrane. In order to keep the drive unit in-plane with the support truss bases, it was necessary to design the truss/hub system with the two bottom trusses slightly shorter than the three top trusses. This design allows the center of gravity of the mirror module to be maintained close to the drive axis. Although the trusses are of two different lengths, the center lines of all the trusses converge at the exact center of the mirror module.

At the time the stainless steel foil was ordered for the prototype mirror module, Type 304L in half-hard condition was not available. Therefore, Type 304 stainless steel was substituted for the prototype design. The only difference between these two types is the L designation, which indicates a lower carbon content. Because a nickel electroplate is used between the membrane and ring, the higher carbon content of 304SS did not cause carbon precipitation.

The ring cross-sectional dimensions for the prototype of 5.1 cm by 15.2 cm (2 in by 6 in) maintain the same aspect ratio as the 7.62-cm by 22.9-cm (3-in by 9-in) ring for the commercial design. However, the minimum wall thickness found in rectangular tubing available commercially in the 5.1-cm by 15.2-cm (2-in by 6-in) size was 4.8 mm (0.188 in). This is considerably thicker than the 2.3-mm (0.09-in) wall thickness designated for the commercial design. The

Table 10.0-1. Heliostat Specifications

	<u>COMMERCIAL</u>	<u>PROTOTYPE</u>
HELIOSTAT DIAMETER	46 FT	26 FT
AREA	1661.9 FT ²	530.9 FT ²
REFLECTIVE AREA	1602.2 FT ²	514 FT ²
SUPPORT RING MATERIAL	A500B CARBON STEEL	A500B CARBON STEEL
SUPPORT RING CROSS SECTION	3 IN x 9 IN	2 IN x 6 IN
RING WALL THICKNESS	0.09 IN	0.188 IN
RING CROSS SECTIONAL AREA	2.16 SQ IN	3.00 SQ IN
RING MOMENT OF INERTIA - I _x	21.01 IN ⁴	11.1 IN ⁴
RING MOMENT OF INERTIA - I _y	3.77 IN ⁴	1.90 IN ⁴
MEMBRANE THICKNESS	0.003 IN	0.003 IN
MEMBRANE PRELOAD	39 LBS/IN	39 LBS/IN
MEMBRANE STRESS	13000 PSI	13000 PSI
NUMBER OF RING SUPPORTS	5	5
SPAN	23 FT	13 FT
DEPTH OF SUPPORT AT HUB	30 IN	18 IN
DEPTH OF SUPPORT AT OUTER RING	12 IN	9 IN
MODULATION PAD DIAMETER	6 FT	4 FT
*CENTER OF GRAVITY	22.3 IN	22.3 IN
FRONT MEMBRANE MATERIAL	304L STAINLESS STEEL - ANNEALED	304 STAINLESS STEEL - ANNEALED
BACK MEMBRANE MATERIAL	304L STAINLESS STEEL - 1/2 HARD	304 STAINLESS STEEL - 1/2 HARD

*NOTE: DISTANCE FROM FRONT MEMBRANE.

ring for the commercial design will be formed from flat coil stock, allowing thinner material to be used.

The capability to defocus the mirror module without external power is not currently implemented in the prototype design. The no-power defocus capability could be added to the improved prototype with a relatively minor effort.

The 15.2-cm (6-in) diameter plenum pressure equalization valve installed in the prototype is the same size valve used in the commercial design. The oversized valve was used in the prototype to mitigate any uncertainty about the operation of the rear membrane modulation focus-control system. The oversized valve allows the refocusing procedure to occur in a shorter time period than is actually required.

The maximum force required from the focus-control linear actuator was calculated to be 2.5 kN (560 lbs) for the prototype mirror module. However, this value was based on purely analytical predictions, and there is some uncertainty about the actual force required from the actuator. Therefore, an actuator with a force capability of 4.4 kN (1000 lbs) was selected for the prototype mirror module. Tests will be conducted with the prototype by measuring the current required for the actuator versus the actuator position. Using correlation curves from the manufacturer, the amount of force required versus actuator position can be determined. This information can be used to update the actuator requirements for the commercial design.

In order to reduce cost, the tooling and fabrication techniques used in production of the prototype mirror module were different than those envisioned for the commercial design. However, every effort was made to design the prototype tooling to simulate the operation of the commercial tooling. A description of the prototype fabrication tooling is not included here, but is discussed in Section 12.0, Fabrication of the Prototype Mirror Module.

11.0 STRUCTURAL ANALYSIS OF THE PROTOTYPE MIRROR MODULE

A complete finite-element analysis was performed on the prototype mirror module design. The methods used in the structural analysis of the commercial mirror module were duplicated for the prototype mirror module. The results of this analysis are summarized in Table 11.0-1. This table shows that the prototype design meets all design criteria, as stated in Appendix A.

The results of the prototype mirror module finite-element analysis were compared to an equivalent analysis performed using NASTRAN, a non-linear finite-element analysis program. The analysis was carried out on the prototype mirror module under 43-km/h (27-mph) wind. Figure 11.0-1 shows front and rear membrane deflection results from this analysis. As can be seen in the figure, a displacement was imposed on the rear membrane to represent the focus control pad pulling back on the rear membrane to focus the mirror module. Figure 11.0-2 shows front and rear membrane stress results. This plot shows a stress concentration around the focus pad of approximately 310 MPa (45,000 psi). These results agree with the Supersap quasi-non-linear results to within 2%.

A finite-element analysis was performed on the prototype hub design. The model was composed of three-dimensional elastic beam elements. Beam properties were determined from reference materials. The nodal degrees of freedom were fixed at the location of attachment to the drive. Reaction forces and moments at the truss-to-hub attachment locations under the worst loading conditions were extracted from the truss finite-element analysis and applied to the hub model. Figure 11.0-3 shows the deflected hub model (magnified 2000 times) superimposed on the undeflected model. Applied forces, moments and boundary conditions are also shown in Figure 11.0-3. The results of this analysis show a high stress in the hub of 67 MPa (9710 psi) and a maximum deflection of 0.64 mm (0.025 in).

Table 11.0-1. Analysis Results for the Prototype Design

●	OPERATING CONDITION: 27 MPH WIND	
-	MAXIMUM RING DEFLECTION BETWEEN TRUSS SUPPORTS	0.089 IN.
-	MAXIMUM RING STRESS	6078 PSI
-	MAXIMUM OUT-OF-PLANE TRUSS TIP DEFLECTION	0.0895 IN.
-	MINIMUM OUT-OF-PLANE TRUSS TIP DEFLECTION	0.0629 IN.
-	MAXIMUM DEFLECTION VARIATION BETWEEN ANY TWO TRUSS TIPS	0.027 IN.
-	MAXIMUM FRONT MEMBRANE STRESS	15541 PSI
-	MINIMUM FRONT MEMBRANE STRESS	13000 PSI
-	MAXIMUM REAR MEMBRANE STRESS (OPERATION AT 120°F)	44368 PSI
●	SURVIVAL CONDITION: 50 MPH WIND	
-	MAXIMUM RING DEFLECTION BETWEEN TRUSS SUPPORTS	0.020 IN.
-	MAXIMUM RING STRESS	6705 PSI
-	MAXIMUM OUT-OF-PLANE TRUSS TIP DEFLECTION	0.298 IN.
-	MAXIMUM TRUSS STRESS	6887 PSI
-	MAXIMUM REAR MEMBRANE STRESS	57703 PSI

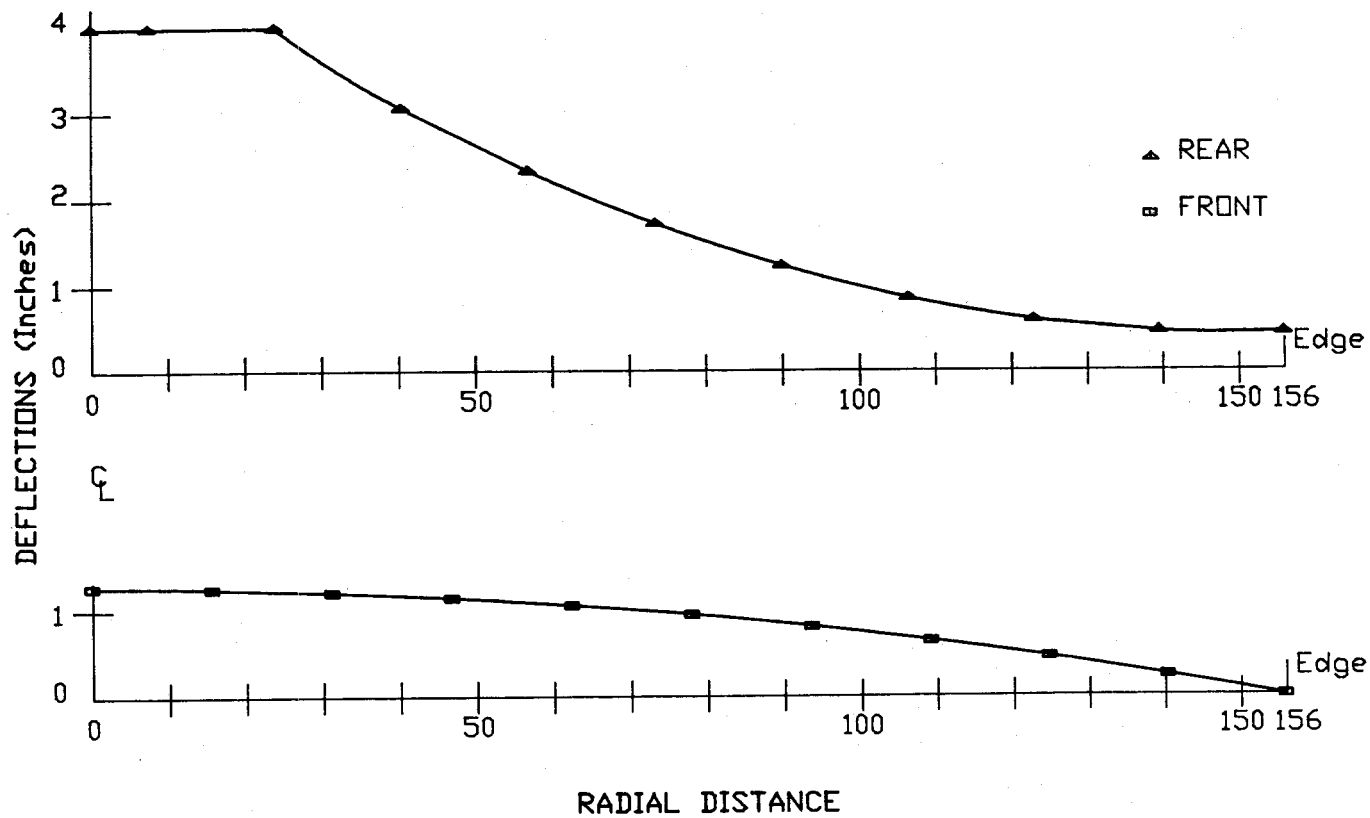
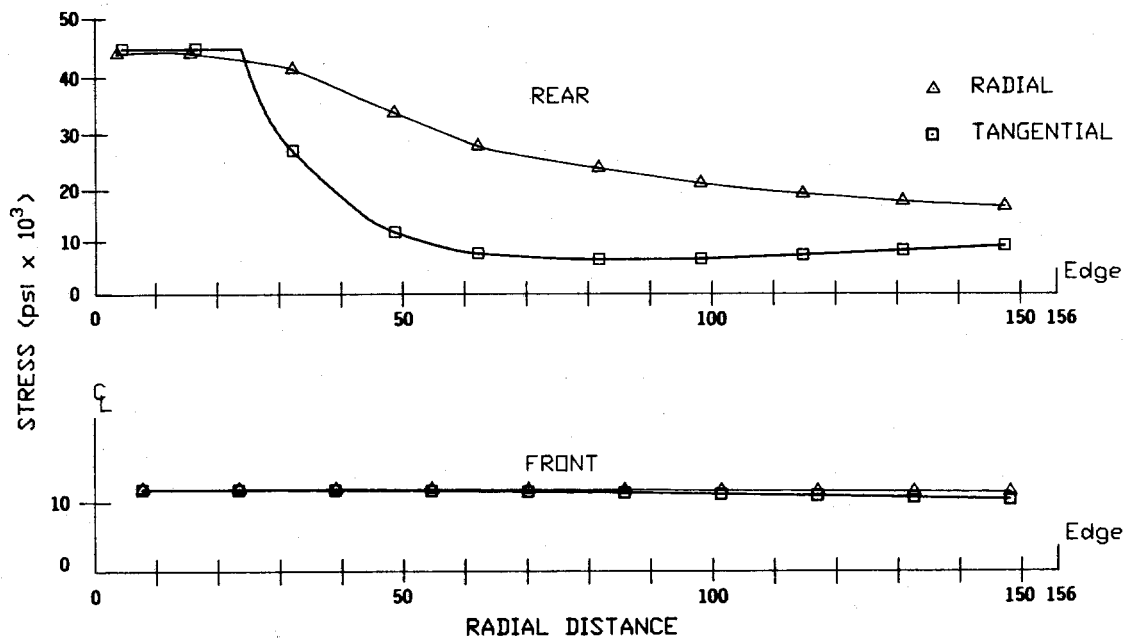


Figure 11.0-1. Membrane Focusing Analysis--Membrane Deflections

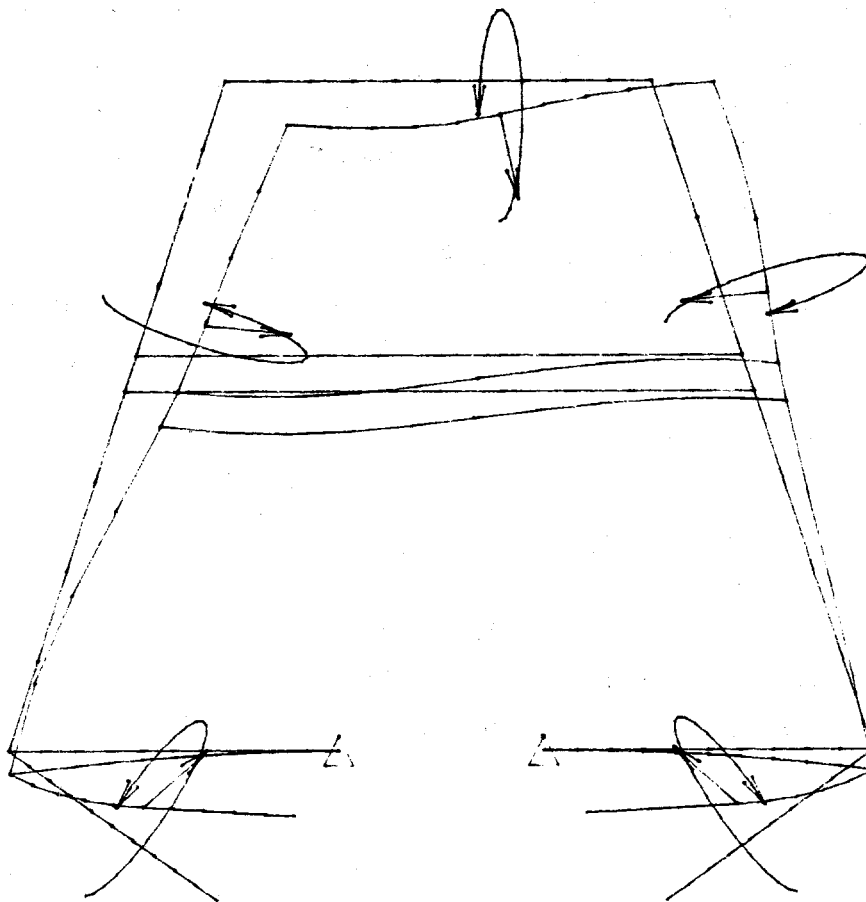
MEMBRANE FOCUSING ANALYSIS MEMBRANE STRESS



12/14/87

Ref. NASTRAN Run SAI12C

Figure 11.0-2. Membrane Focusing Analysis--Membrane Stress



DEFLECTIONS MAGNIFIED 2000X

Figure 11.0-3. Hub Model Deformed Under Applied Loading

12.0 FABRICATION OF THE PROTOTYPE MIRROR MODULE

Fabrication and installation were critical to the successful completion of the prototype mirror module. As was the case in the first generation prototype, the components were fabricated in San Diego, CA in SAIC's Concentrator Development Laboratory and then shipped to the Central Receiver Test Facility at Sandia National Laboratories in Albuquerque, NM for assembly and installation. On-site installation is required because the mirror module's size, 8-m (26-ft) in diameter, is too large for any form of conventional shipping.

The major pieces of special tooling required for San Diego fabrication included:

1. Stationary roll-resistance welder,
2. 1.22-m by 9.14-m (4-ft by 30-ft) membrane vacuum table,
3. Hand-held tack/spot welder,
4. Ring nickel electroplating equipment,
5. 9.14-m (30-ft) long membrane welding carriage,
6. Reflective film lamination equipment,
7. Electronic test equipment for simulation and checkout of the focus-control electronics.

The major pieces of special tooling required for assembly in Albuquerque included:

1. 8-m (26-ft) diameter adjustable-level table,
2. Ring leveling revolving laser,
3. 8.23-m (27-ft) diameter membrane tensioning reaction ring with inflatable bladder,
4. Hand held roll-resistance welder,
5. Nine adjustable support stanchions for positioning of the mirror module ring and reaction ring.

The two fabrication processes considered most critical were the membrane welding process and the membrane tensioning and attachment process. A sketch of the membrane welding process is shown in Figure 12.0-1. The 60.96-cm by 9.14-m (24-in wide by 30-ft long) strips of .0762-mm (.003-in) thick stainless steel foil were first tack welded together at 2.5-cm (1-in) intervals while on the 1.22-m by 9.14-m (4-ft by 30-ft) membrane vacuum table. The definition of the flatness of the membrane is determined during the tack-welding process. This process is analogous to pinning a garment before it is sewn. As the membrane strips were tack welded, the membrane was rolled onto a 22.9-cm (9-in) diameter roller as shown in Figure 12.0-1. The membrane was then routed through the roll-resistance weld heads to a second 22.9-cm (9-in) diameter roller. The continuous roll-resistance seam welds were then executed by movement of the roller-support carriage. Obtaining the proper welder parameters is critical in obtaining a high-quality weld. Critical parameters include the wheel width, wheel pressure, electric current, AC cycle time, and weld carriage speed.

The method used for tensioning the membranes is depicted in Figure 12.0-2. The tensioning method replicates the membrane tensioning device described in Section 7.0 (Commercial Manufacturing Scenario) to the extent practically possible. The prototype tensioning fixture shown allows in-plane tensioning of the membrane and provision for circumferential expansion by the use of intermittent attachments to the tensioning device. These two facts are critical in providing uniform circumferential and radial tension in the membrane. The use of the air-inflated tensioning bladder imparts uniform stress rather than uniform strain on the membrane, which is important in removing any inconsistencies and wrinkles in the membrane.

As shown in Figure 12.0-2, a reaction ring was placed around the outside of the actual heliostat ring. The reaction ring was in the form of an I-beam with a tensioning bladder on the outside of the web. Stainless steel strips were welded to the perimeter of the top and bottom membranes as shown. The strips were 10-cm (4-in) wide and made from 0.203-mm (.008-in) stainless steel foil. The bladder was then inflated, which pulled the strips out radially and tensioned the membranes. Once the membranes were under tension, the hand-held roll-resistance welder was used to weld the membranes to the heliostat ring along the nickel electroplate strips at the top and bottom flanges. Once the membranes

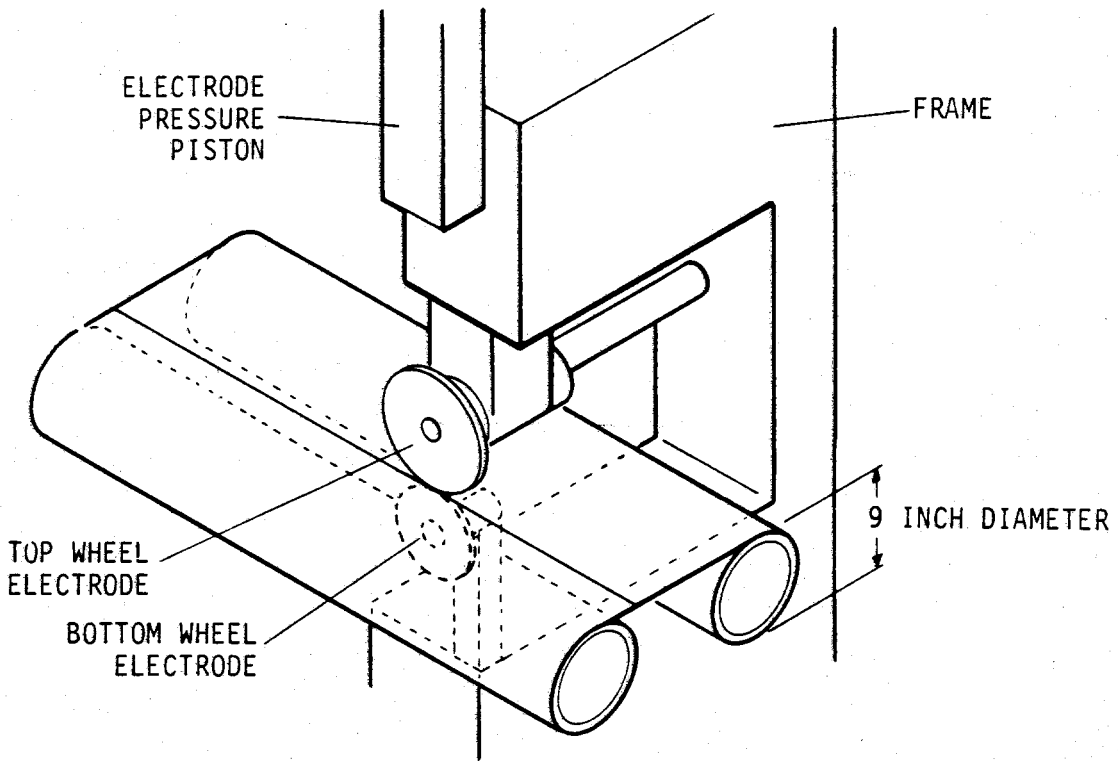


Figure 12.0-1. Second-Generation Prototype Welding Fixture

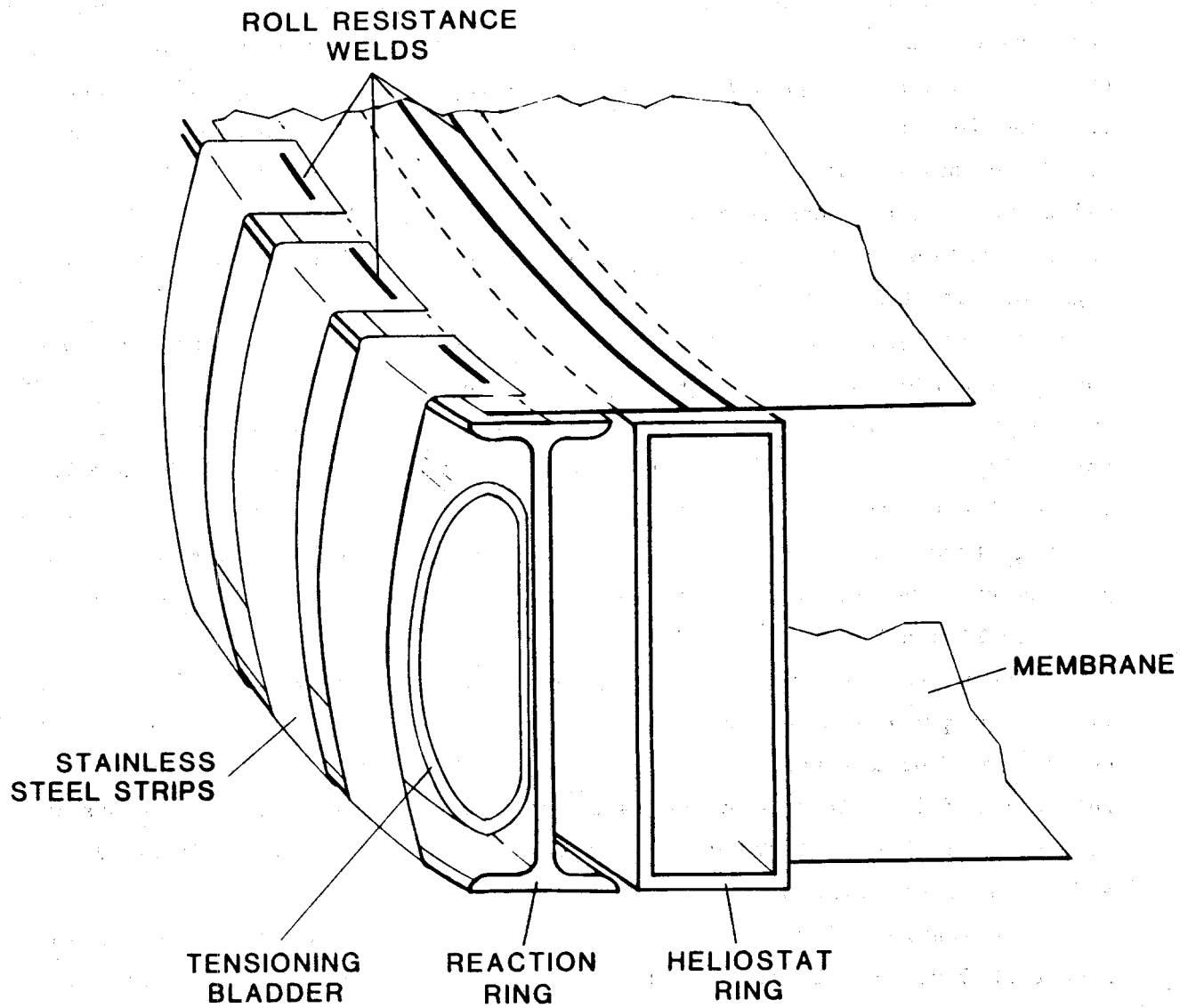


Figure 12.0-2. Prototype Mirror Module Membrane Tensioning

were welded to the ring, the bladder pressure was released and the tensioning strips, reaction ring, and excess membrane material removed. Some compression of the ring and relaxation of the membranes then took place. No ring pre-compression was used, in contrast to the commercial tensioning system design. Effective ring pre-compression would require significant tooling to hold the ring in-plane in order to avoid ring buckling before the membranes were attached. To reduce tooling cost, the membranes were overstressed to 120-MPa (17,500-psi), welded to the ring, then released to achieve the desired operating tension. This is achievable with steel components (membrane and ring) because of the relatively high modulus of elasticity.

A more general description of the remainder of the mirror module fabrication process with reference to photographs is included here. The 5.08-cm by 15.24-cm (2-in by 6-in) carbon steel rectangular tube was rolled into three ring segments by a local San Diego ring roller. As shown in Figure 12.0-3, the nickel electroplating was then applied to the ring segments. The truss-to-ring attachment brackets are shown in Figure 12.0-4. The membrane welding process with the roll-resistance welder and membrane support fixture tooling is shown in Figure 12.0-5 and 12.0-6.

The reflective film lamination process is shown in Figure 12.0-7. A dry lamination process was used to laminate the film between the seam welds. Reflective tape was then used to overlap the seam welds and the edges of the reflective film. Once membrane fabrication was complete, the membranes were rolled up on 22.9-cm (9-in) diameter cardboard tubes as shown in Figure 12.0-8, and prepared for shipment.

Fabrication of the tapered triangular ring support trusses is shown in Figure 12.0-9. Fabrication of the prototype hub required large machine tools that were not available at the SAIC Concentrator Development Laboratory. Therefore, the hub drawings were submitted to a local vendor for fabrication. The completed hub is shown in Figure 12.0-10. As shown in the photo, a dummy drive was fabricated as a spacer to assure the proper placement of the torque-tube attachment flanges.

Checkout of the focus-control system electronics is shown in Figure 12.0-11. The response of the control system was monitored with an oscilloscope as the membrane position input signal was varied. Subsequent tests included

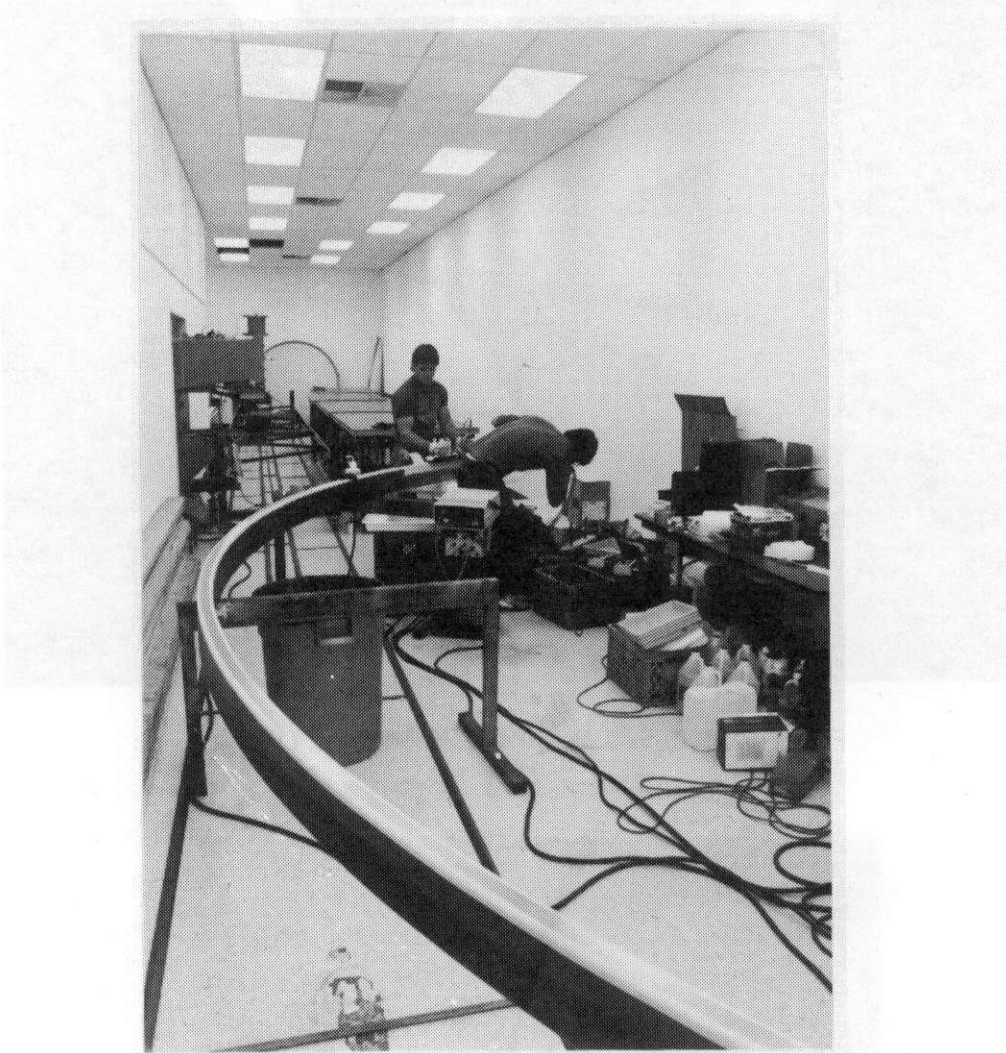


Figure 12.0-3. Ring Section Nickel Electroplating

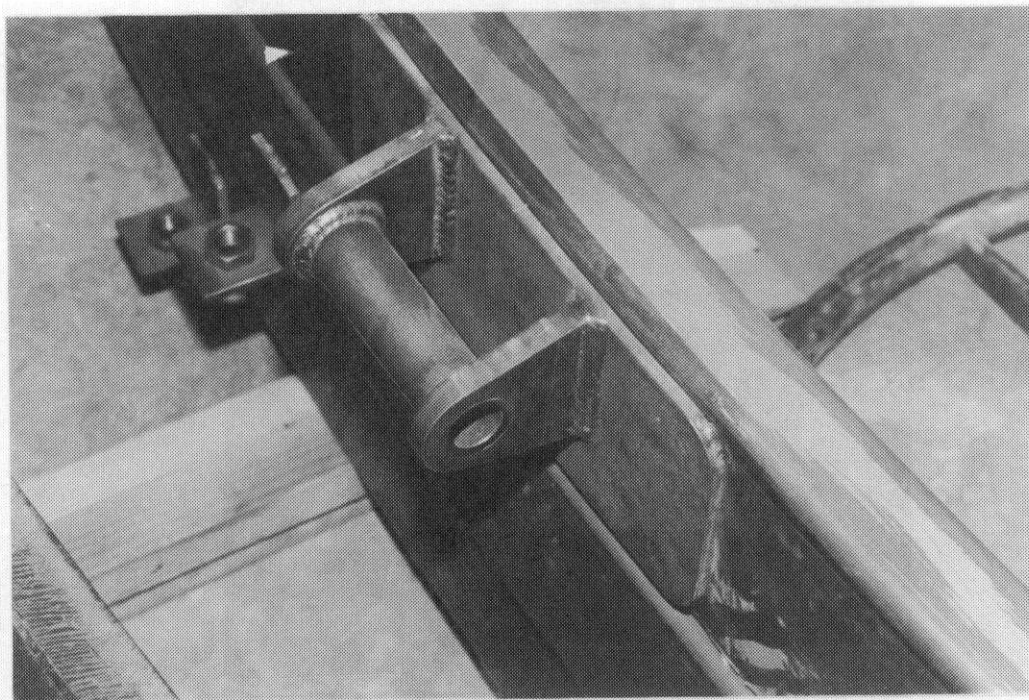


Figure 12.0-4. Prototype Ring-to-Truss Attachment Bracket



Figure 12.0-5. Membrane Welding (View 1)

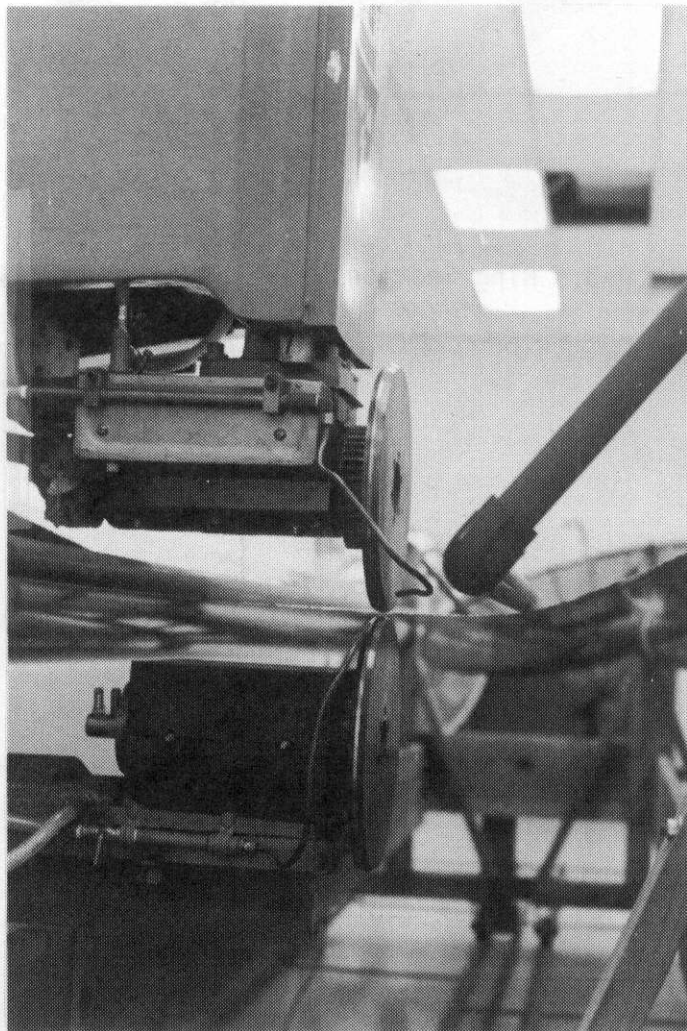


Figure 12.0-6. Membrane Welding (View 2)

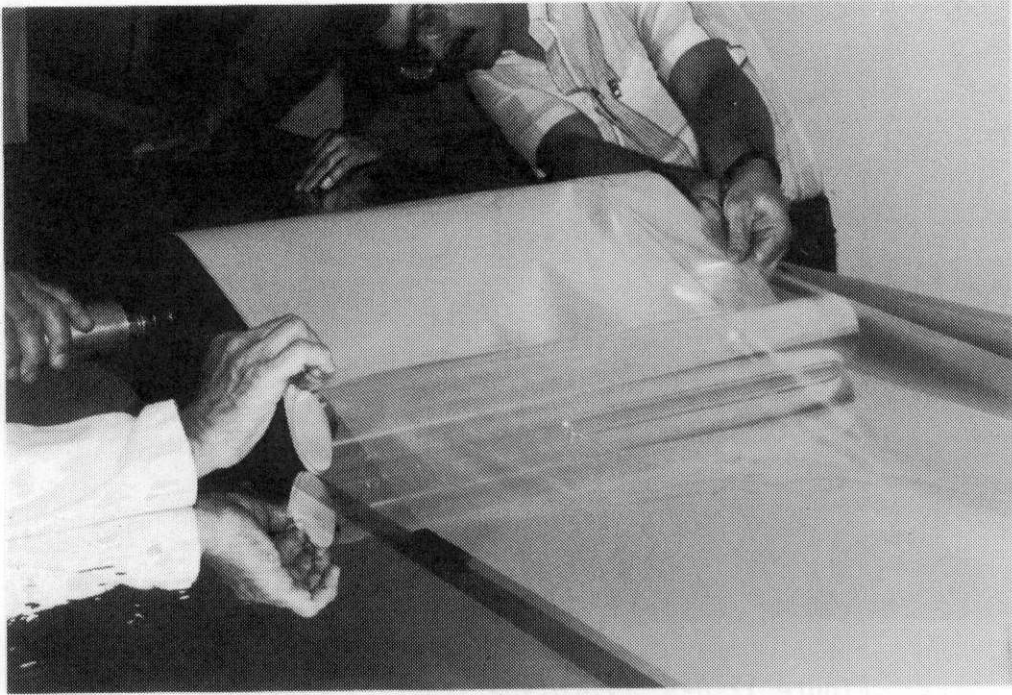


Figure 12.0-7. Reflective Film Lamination to Membrane



Figure 12.0-8 Membranes Prepared for Shipment

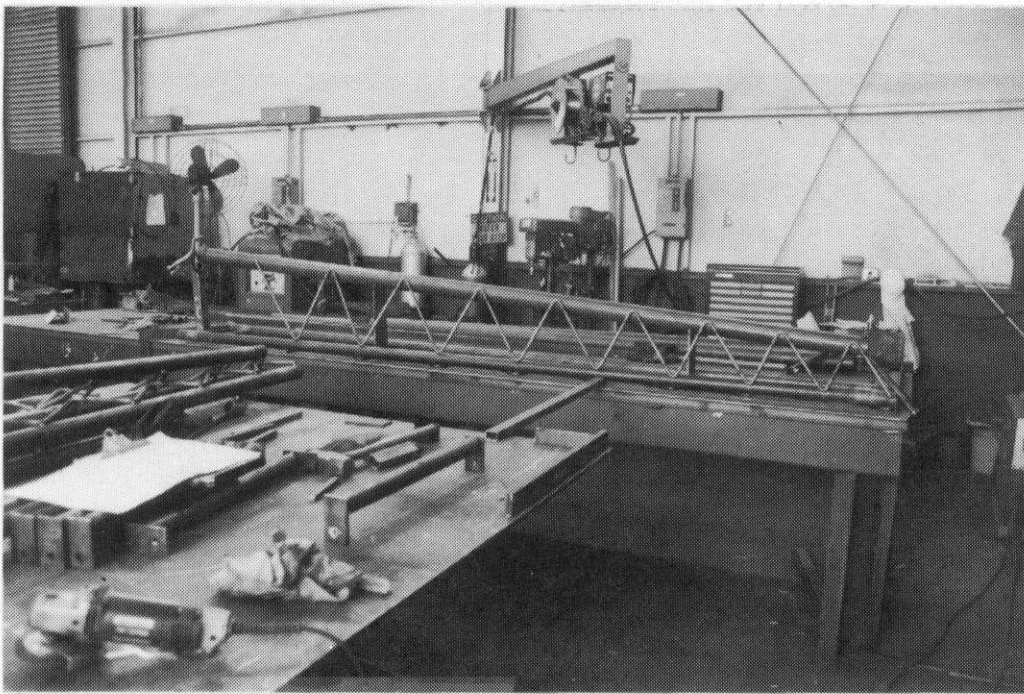


Figure 12.0-9 Prototype Truss Fabrication

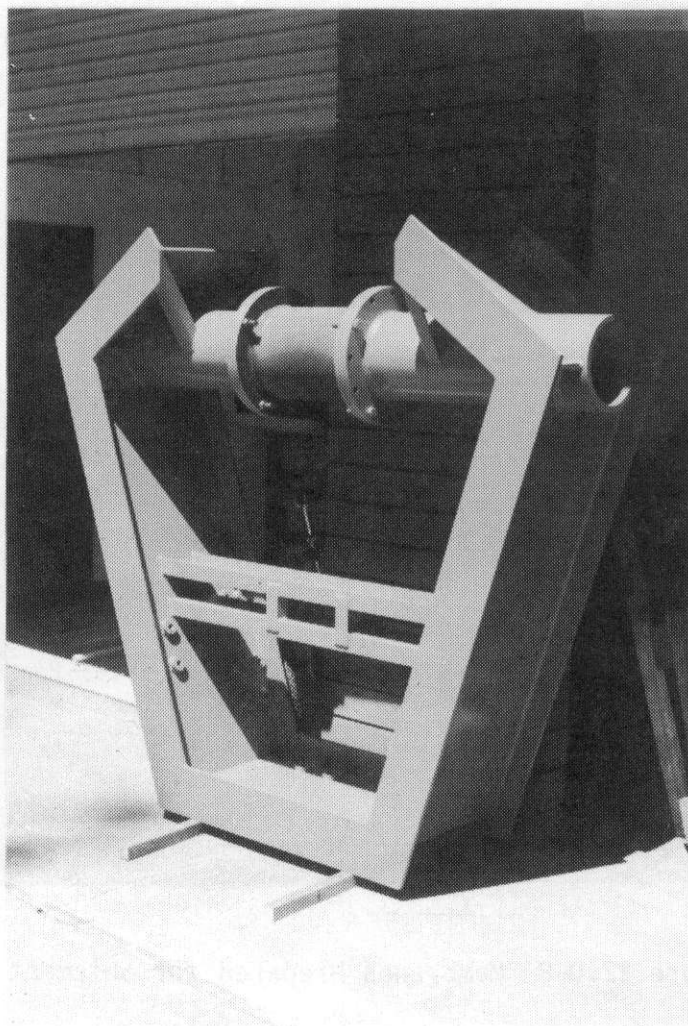


Figure 12.0-10. Prototype Hub

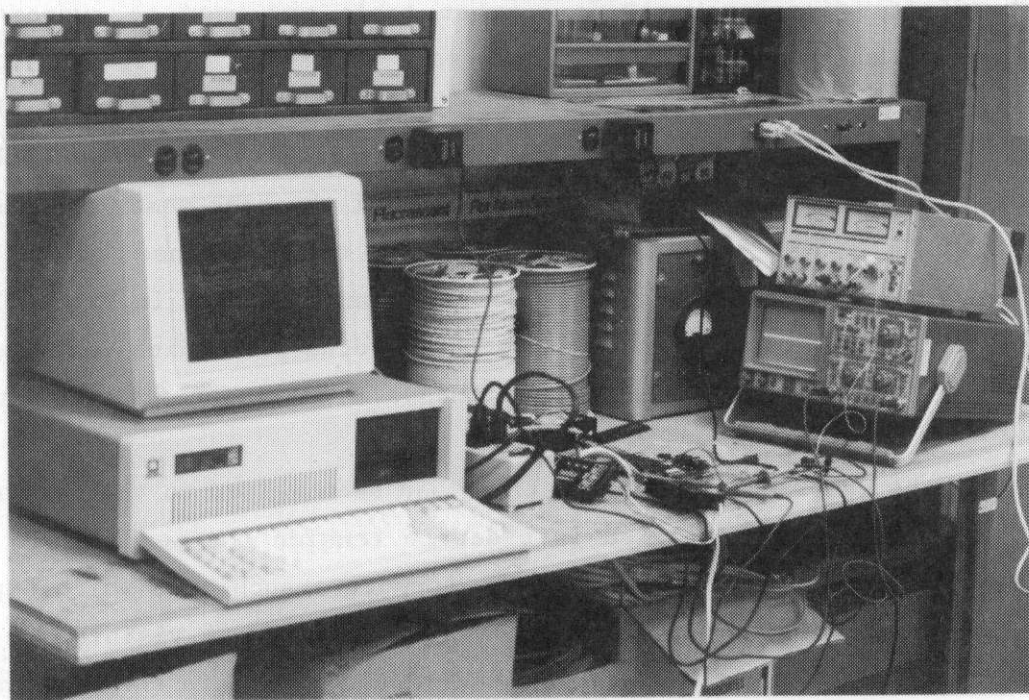


Figure 12.0-11. Checkout of the Focus Control System

attachment of the plenum pressure equalization valve and linear actuator to the control system to verify their operation.

After all the components were fabricated in San Diego, a trial fit-up of the hub, trusses, and ring was completed. After some minor adjustments, these components, along with the membranes and focus-control components, were loaded in a truck and shipped to the Central Receiver Test Facility in Albuquerque. The 7.92-m (26-ft) diameter membrane support table was used to support the membranes during the module fabrication process. As shown in Figures 12.0-12 and 12.0-13, the tensioning strips were welded to the top and bottom membrane with the use of a hand-held roll resistance welder. Installation of the membrane reinforcement rings around the hole in the center of the back membrane is shown in Figure 12.0-14. The focus/defocus pads were then attached to the back membrane. A view of the inside of the back membrane is shown in Figure 12.0-15. The small ring visible in the photo is the defocus pad, which contacts the front membrane during the defocus process when a significant frontal wind is present.

Once all the membrane tensioning strips had been welded to the membranes, the tensioning bladder was inflated in order to tension the membranes. This process is depicted in Figure 12.0-16. The support stanchions, which support both the heliostat ring and the reaction ring, are also visible in this photograph. As shown, bricks were used as ballast to maintain the position of the stanchion bases during the ring leveling process.

Once the membranes were brought to the proper tension level, the membranes were welded to the heliostat ring as shown in Figure 12.0-17. The membrane strain was measured to determine the stress level. A hand-held roll resistance welding unit manufactured by Unitek was used to accomplish the over-lapping spot type seam weld. The weld site was water quenched to limit overheating and to preclude carbon precipitation to the surface of the membrane. Two membrane-to-ring welds, parallel to one another, were used.

As shown in Figure 12.0-18, the hub and truss subassemblies were assembled separately. The hub and truss subassembly was then placed on the completed mirror module and attached at the five mounting locations, as shown in Figure 12.0-19. The overhead crane in the assembly building was utilized for this process. Once the truss/hub structure was attached, a final check of the



Figure 12.0-12. Tensioning Strips to Membrane Weld (View 1)

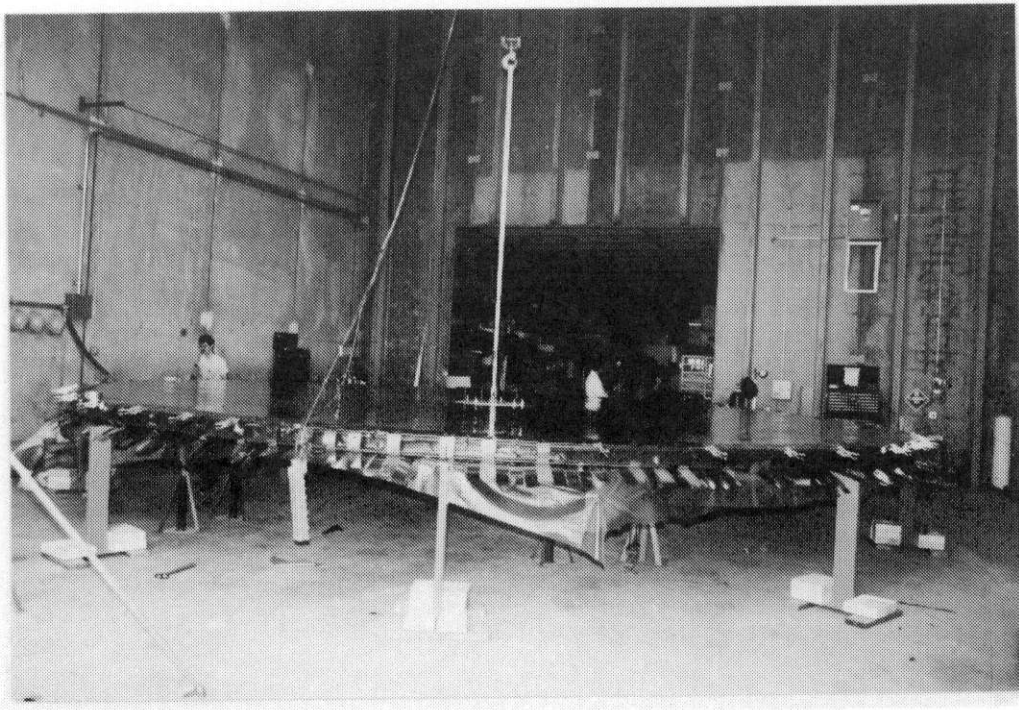


Figure 12.0-13. Tensioning Strips to Membrane Weld (View 2)

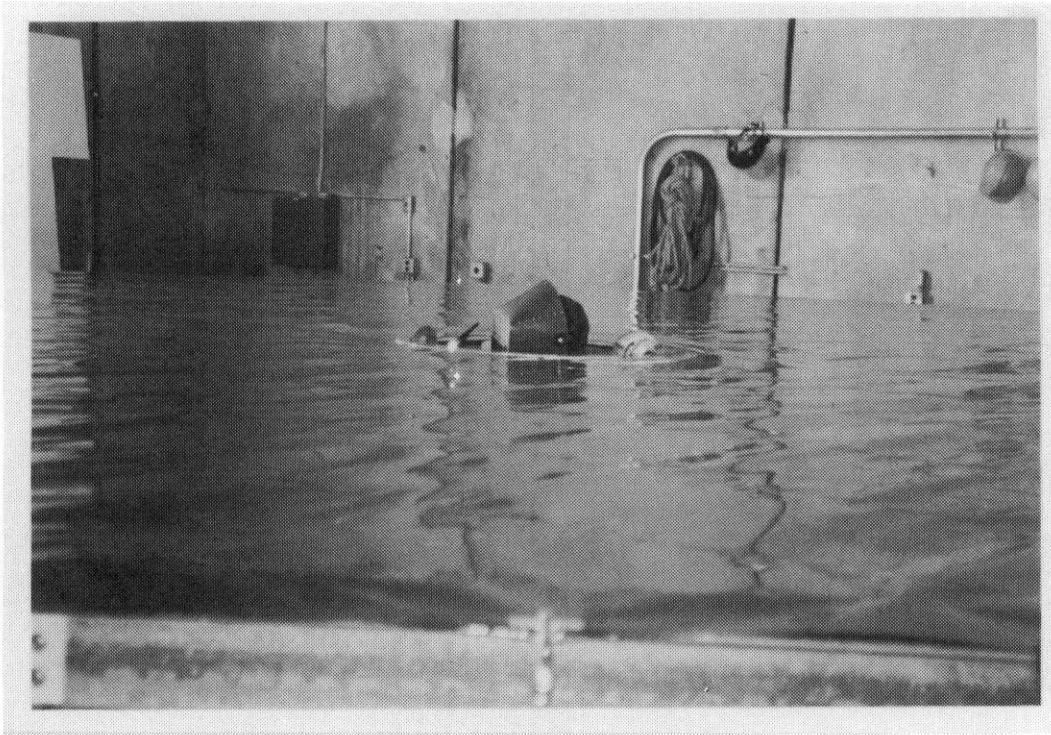


Figure 12.0-14. Welding of Back Membrane Porthole Reinforcement



Figure 12.0-15. View of Inside of Back Membrane

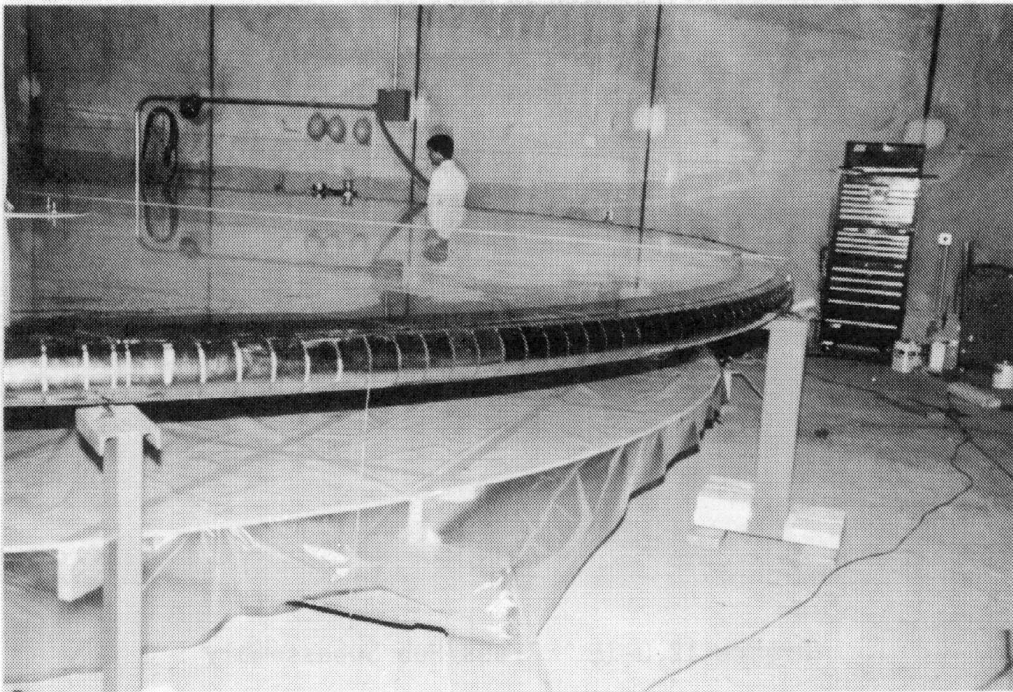


Figure 12.0-16. Membrane Tensioning



Figure 12.0-17. Membrane to Ring Welding



Figure 12.0-18. Truss/Hub Subassembly

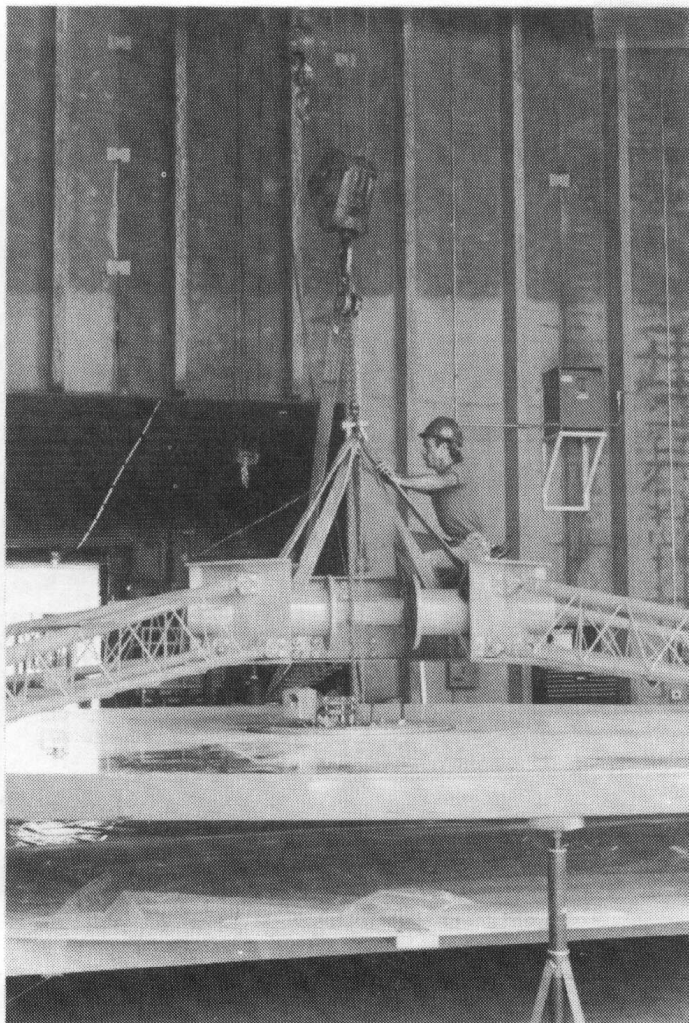


Figure 12.0-19. Mirror Module Assembly

level of the ring was made before installation of the mirror module on the drive system. Installation of the mirror module on the drive system is shown in Figures 12.0-20 through 12.0-22. Once the mirror module was mounted on the drive, the focus-control electronics box was mounted on the lower truss and the LVDT was mounted and adjusted. The data link with the control computer was then established. The optimum focal length set point was determined by adjusting the focal length set point and minimizing the image on the target. The other focus-control input parameters were then set to the desired levels. Subsequently, the defocus and stow modes were checked out. Following these checkouts, the heliostat assumed normal operation successfully.

Assembly of the mirror module in Albuquerque began on 21 June 1988. Checkout was completed, and successful operation was achieved on 8 July 1988. The entire tooling set-up, assembly, installation and checkout of the mirror module were accomplished in thirteen working days. On the average, four people were on the SAIC site crew during this period.

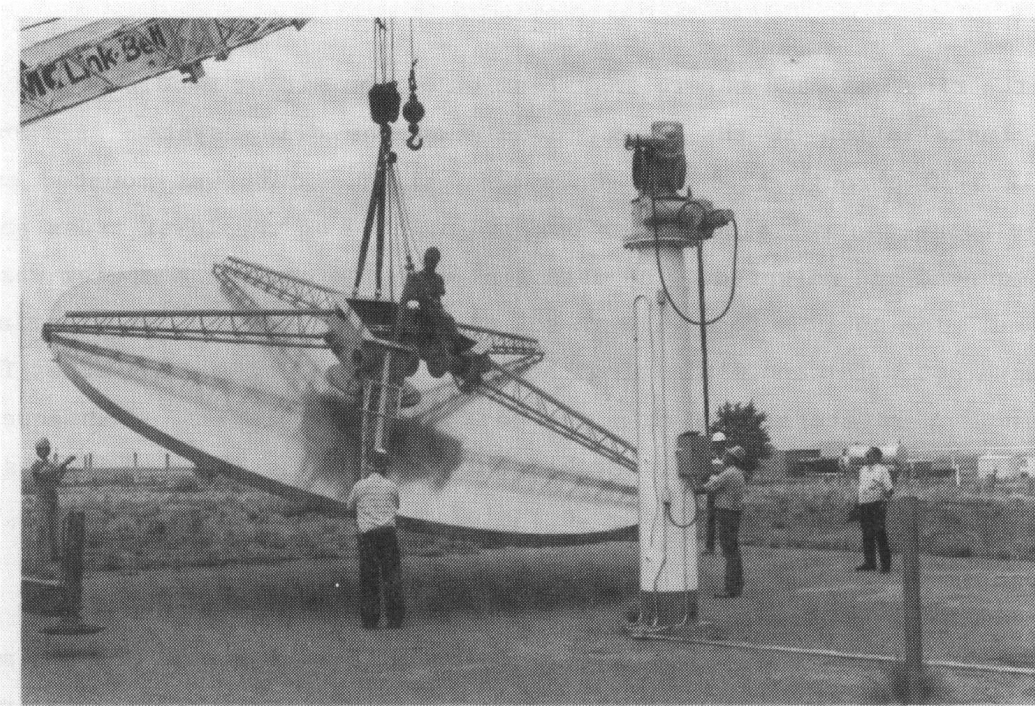


Figure 12.0-20. Installation of Mirror Module (View 1)

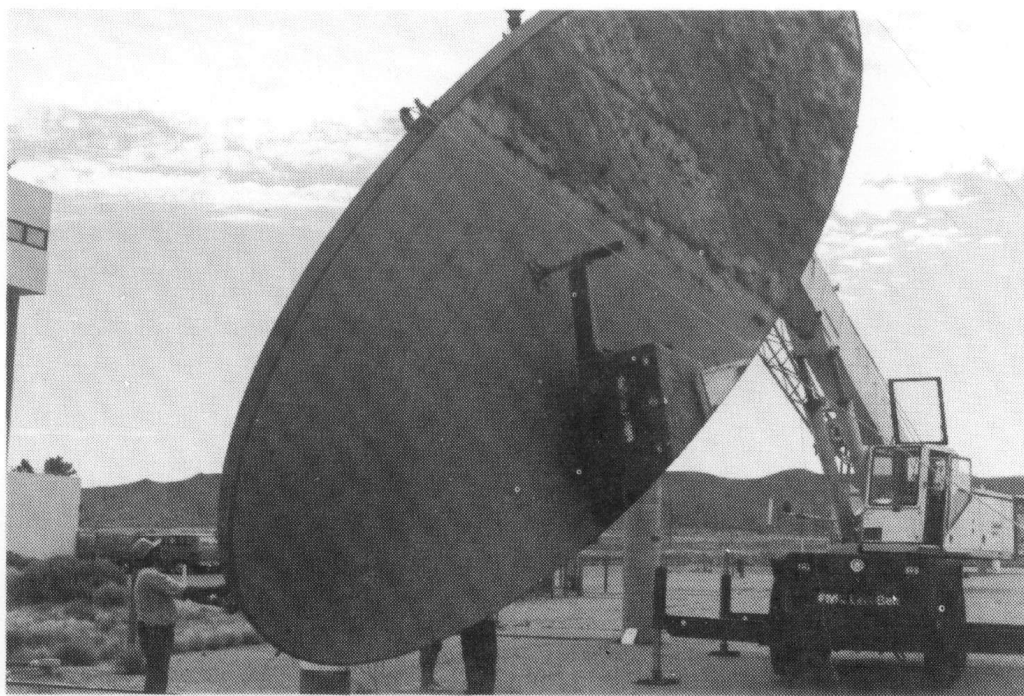


Figure 12.0-21. Installation of Mirror Module (View 2)



Figure 12.0-22. Installation of Mirror Module (View 3)

13.0 PRELIMINARY TEST RESULTS OF THE PROTOTYPE HELIOSTAT

The 50-m² second-generation prototype stretched-membrane heliostat was assembled and installed at the Central Receiver Test Facility in July 1988. Preliminary test results from the mirror module have shown excellent optical performance and focus-control system performance under calm and gusting wind conditions.

A flux contour map, as measured with a beam characterization system at the CRTF, is shown in Figure 13.0-1. A comparison of the measured beam shape with an analytical prediction generated by the HELIOS computer program is shown in Figure 13.0-2. For a reflected cone containing 90% of the reflected energy, the cone half-angle is 1.4 mRad (2.8 mRad full-angle). This indicates that the optical quality of the stretched-membrane mirror module is very good.

Measurements of the on-target energy from the mirror module as a function of wind speed have shown that the novel focus-control system used on this prototype is very effective in keeping the image quality high in gusting winds. As shown in Figure 13.0-3, the time to defocus the image of the mirror module is about 3 to 4 seconds. Additional optical and structural testing of the second-generation prototype mirror module will take place in the next year.

Preliminary observations of the focus-control system power requirements indicate a 5-watt continuous load and peak loads of 15 watts when the linear actuator is operating. The linear actuator operates about 5% of the time.

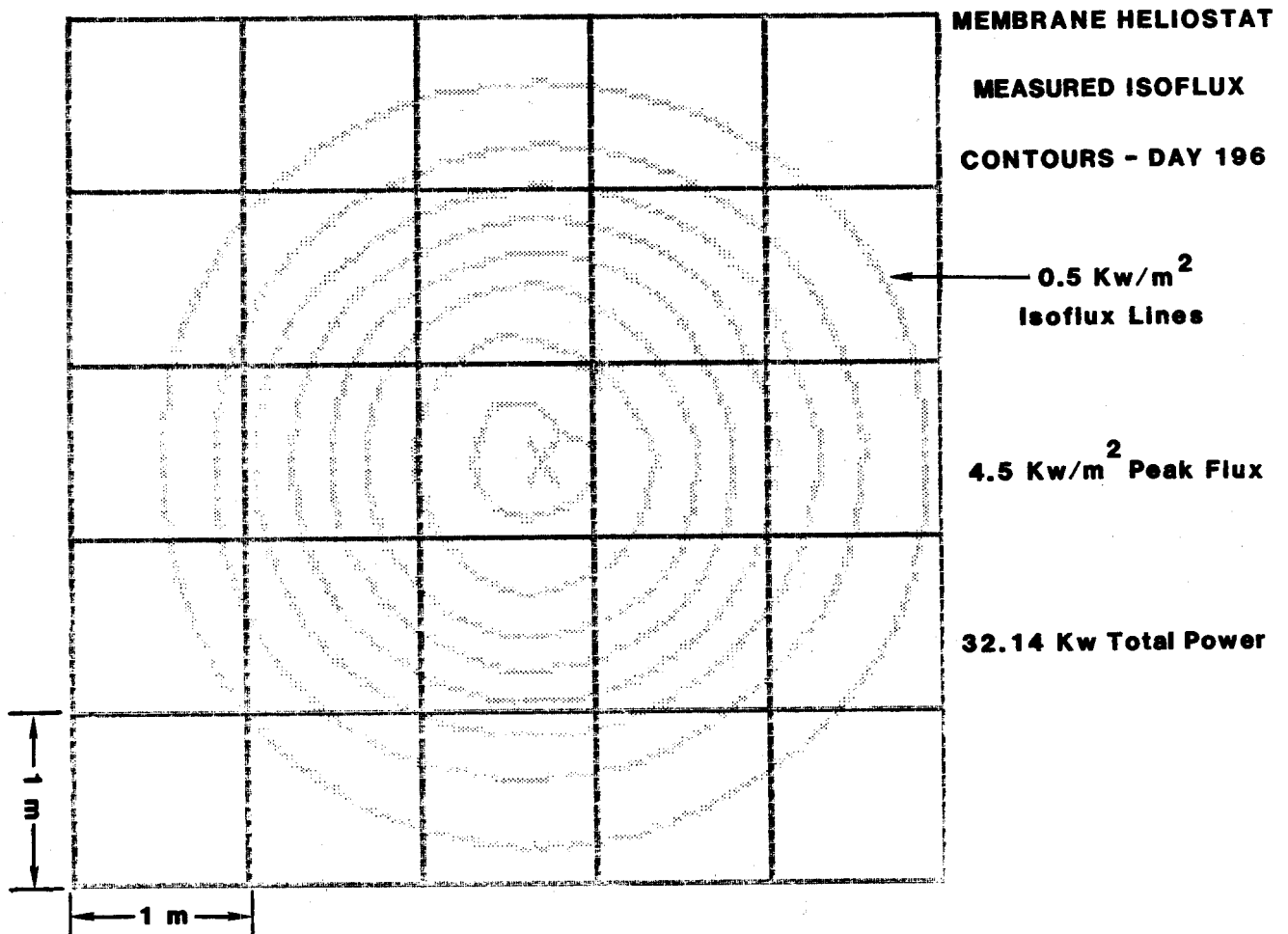


Figure 13.0-1. Membrane Heliostat Measured Isoflux Contours - Day 196

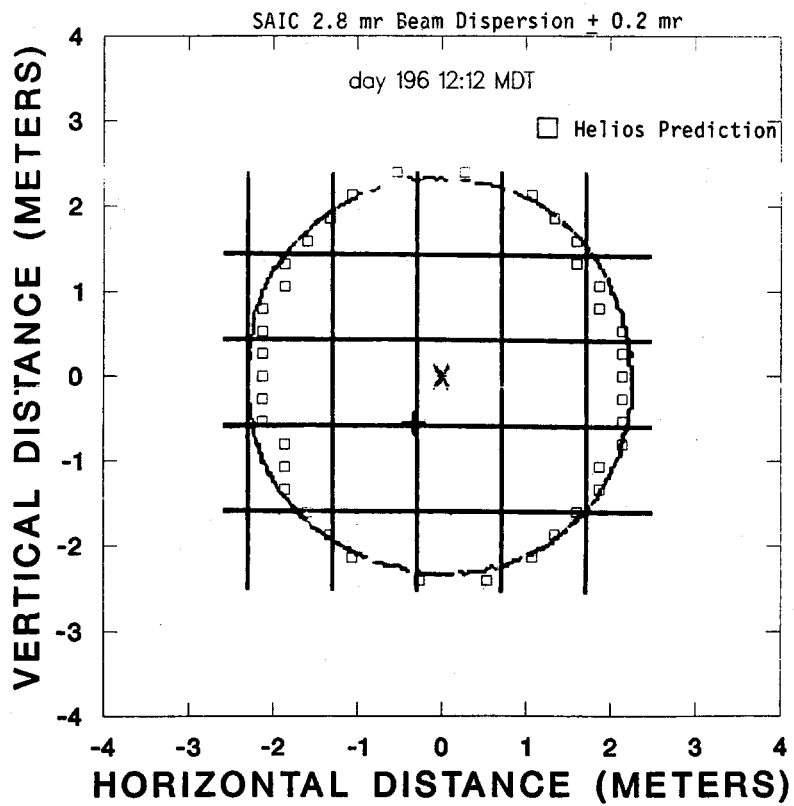


Figure 13.0-2. Full Beam Cone Angle at 90% Power Intercept Actual Versus Helios Prediction

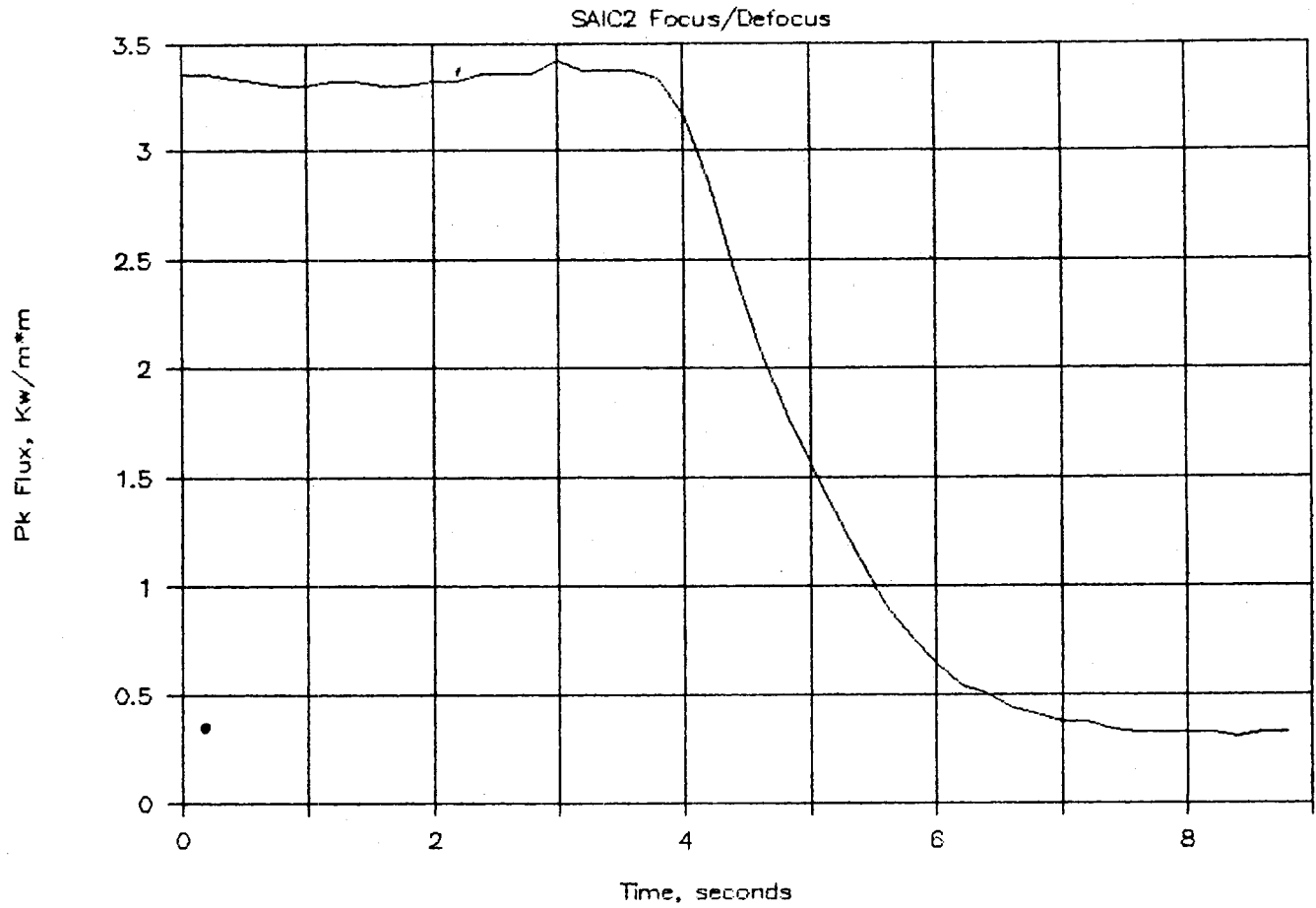


Figure 13.0-3. Defocus Time of the Membrane Heliostat

14.0 SUGGESTIONS FOR FURTHER DEVELOPMENT

Substantial improvements were made in the SAIC second-generation stretched-membrane mirror module as compared to the original first-generation module. Significant improvements were made in the areas of analysis techniques, mirror module design, and fabrication techniques. The "as-tested" optical quality of membrane heliostats has now been proven to be well suited to central receiver applications. Although further improvements in optical quality are achievable, this area is seen as secondary compared with investigating methods to further reduce costs, improving the lifetime of the reflective surface, and designing of tooling for the manufacture of large quantities of heliostats.

14.1 Potential Cost Reduction

Any further cost reduction for stretched-membrane heliostats must be accomplished by reducing materials and/or labor cost. Material cost may be reduced by reducing the amount of material used for various components, substituting lower cost materials, or using alternate design concepts.

Several areas of uncertainty in the second-generation mirror module design may have caused the over-design of some components. For example, the portion of membrane wind loads that is transferred directly to the focus-control system linear actuator was not considered in designing the support trusses for the ring. At the time of the design, it was thought that some failure modes of the focus control system might cause the full wind load to be reacted by the ring support trusses. Therefore, the trusses were designed to withstand the full wind load. Also, the dynamic effects of modulating the rear membrane to offset wind gusts were not well understood. Further, the nature of the wind loads themselves is not well understood. Further research in these and other areas through design analysis and testing of the prototype mirror module may reveal locations where the size of structural components may be reduced.

The SAIC mirror module is essentially all fabricated from low-cost carbon steel, except for the membrane material and the reflective film. SAIC's supplier of flattened stainless steel foil has suggested that Type 201 stainless steel might be a suitable substitute for the Type 304L stainless steel currently

utilized in the design. Type 201 has the same chemical makeup as type 304, except for a lower chromium content. The cost and availability of chromium have driven up the cost of 300-series stainless steels recently. The chromium content is required for high-temperature applications, but is not necessarily required for the ambient temperature conditions of stretched-membrane heliostats. A savings of 25% in membrane materials may be achievable if Type 201 stainless steel is utilized.

The ECP-300 silverized polymer reflective film is by far the highest cost component of the mirror module. More cost-effective methods of reflective film production, or alternate methods of reflectorizing the mirror module membrane, could substantially reduce the cost of the mirror module. Such alternate methods include use of micro-sheet glass, or direct deposition of Sol-gel or hard silicon resin as protective layers for the reflective surface.

A major area of potential cost reduction is the utilization of an alternate means for support and tracking of the mirror module. The pedestal-type drive system, originally designed for glass/metal heliostats, provides support at the center of the back of the mirror module. This method works satisfactorily for glass/metal heliostats because the wind and gravity loads are essentially distributed evenly over the area of the mirror module support structure. In the case of stretched-membrane heliostats, the wind loads must be transferred from the membranes to the support ring, and then back to the pedestal drive unit through the support trusses. These two loading conditions are analogous to a cantilevered beam with a distributed load versus a cantilevered beam with a tip load of equal magnitude. Considerably higher moments and stresses are found in the beam with the tip load. Capability of face-down stow is also more important for stretched-membrane heliostats because the reflective surface is more vulnerable to hail damage. The possible solution to these problems is to support the mirror module at the perimeter rather than at the center. "Rim drive" systems such as this have been proposed and partially developed by DAN-KA Products, SAIC, SKI, and others.

14.2 Life of the Reflective Surface

The reflective surface of the prototype mirror module is composed of 3M brand ECP-300, .010-mm (.004-in) thick silvered acrylic film. The film has a spectral reflectance of 94% and a pressure-sensitive adhesive backing. The film consists of vapor deposited silver on a sheet of acrylic film.

A major factor affecting the cost to maintain stretched membrane heliostats is the lifetime of this reflective film. The major degradation mechanisms are delamination between the top acrylic layer and the silver, and oxidation of the silver. Delamination has been observed on all the prototype stretched-membrane heliostats fabricated to date. It first appears at a corner or edge of a strip of the reflective film and slowly works into the center of the strip. Delamination may also begin at a crack or crease in the reflective film. Moisture has been observed in most delaminated areas of the film and probably plays a role in the delamination process.

Since delamination usually begins at an edge, improvements in the edge-sealing techniques could improve the reflective film's life. Improvements in the reflective film-to-membrane lamination process itself may also extend the film's life. Research at the Solar Energy Research Institute (SERI) is focused on developing the polymer layer composition to provide more protection for the reflective silver from oxygen and UV degradation.

Given the current status of reflective film technology, the film must be removed and replaced at five- to ten-year intervals. The labor and materials for this procedure will have a major impact on the heliostat life-cycle cost. Therefore, research to extend the life of the reflective film, and also to find alternate methods of applying a reflective surface to the membrane, should be a major priority. Sandia National Laboratories is currently developing a silver/Sol-gel process in which the silver and thin layers of Sol-gel (a glass-like substance) are applied directly to the metal membrane. Another technique available is the use of flexible micro-sheet glass with a metalized second surface.

14.3 Development of Commercial Tooling

Even with the demonstrated success of the stretched-membrane concept in the last few years, immediate commercialization of this technology would be difficult because of the lack of tooling to produce heliostats in large numbers. Even construction of a single power plant requiring 3,000 to 6,000 heliostats would require extensive development. Experience gained on the contracts to develop two stretched-membrane mirror modules has revealed the importance of proper design, development, and fabrication of tooling. Design and fabrication of tooling for large-quantity production would require a major effort.

The cost of production tooling design could be at least partially offset by the revenue from heliostat sales. However, in order to increase the possibility of commercialization of the technology, early generation of preliminary designs for the major pieces of fabrication tooling would be very valuable. Government-sponsored research to bring the fabrication tooling development to the preliminary design stage would aid in making more accurate predictions of the cost of heliostat production, reduce the amount of time required for tooling design and fabrication when required, and reduce the perceived risk to the customer and heliostat manufacturer alike.

14.4 Suggested Development Program

In summary, the following programs are suggested in order to bring stretched-membraned heliostat technology to a state of readiness for commercialization.

1. Continue research on alternate mirror module drive designs in order to reduce support structure weight and cost. Designs that allow for face-down stow of the mirror module should be considered. Face-down stow protects the reflective membrane from hail damage and most likely will extend the life of the reflective film by reducing exposure to soiling and moisture.

2. After choosing the heliostat drive system or systems, reoptimize the commercial heliostat size in conjunction with the drive. The 150-m² size chosen for the stretched-membrane commercial heliostat has been based on operation with a pedestal-type drive system. Optimization with an alternate drive will most likely result in a different size.
3. Design and fabricate a fully integrated commercial-scale mirror module and drive system. To date, stretched-membrane mirror modules have been adapted to existing pedestal drive systems for the purposes of demonstration and testing. Integration of a stretched-membrane mirror module with an optimized drive system at the optimized commercial size would be a logical next step in the development of this technology.
4. Continue analysis and experimentation on the structural response of stretched-membrane heliostats to wind and gravity loads. As more is understood about this subject, structural safety factors may be reduced in some areas, resulting in decreased weight and cost.
5. Continue efforts to extend the life of the silverized polymer reflective film. Also continue research on Sol-gel/silver reflective surfaces, and micro-sheet glass/silver reflective surfaces. Consideration should be given to surfaces that have a high reflectivity in the ultraviolet range for use in toxic waste destruction applications.
6. Develop preliminary designs for the key pieces of fabrication tooling. Determine the cost of the major pieces of fabrication tooling. Perform bench-scale experiments for development of large-quantity production tooling where applicable. The production capacity of the tooling should be adequate for supplying heliostats for a single full-scale commercial central receiver power system because this is the most likely first large-scale production

opportunity. Subsequent increases in heliostat production capacity would probably be accommodated by automating additional labor-intensive fabrication steps, and by replicating the key pieces of fabrication tooling to provide parallel production streams.

Research on stretched-membrane heliostat technology to date has made great strides in reducing the weight and cost, and increasing the performance of heliostats. Although stretched-membrane heliostats are nearing readiness for commercialization, implementation of the suggested development program would greatly increase the chances of successful commercialization of stretched-membrane heliostats in particular, and central receiver power systems in general.

15.0 REFERENCES

1. Science Applications International Corporation, San Diego, CA, Development of Stressed Membrane Heliostat Mirror Module Final Report, SAND87-8179, April 1987.
2. Solar Kinetics, Inc., Dallas, TX, Development of the Stressed Membrane Heliostat, SAND87-8180, Albuquerque: Sandia National Laboratories, April 1987.
3. M. Berry, Plastic Heliostat and Heliostat Enclosure Analysis, Sandia Report - SAN81-8188, Livermore, CA: Sandia National Laboratories, p. 200, 1981.
4. R. Gillette, "Heliostat Environmental Protective Enclosures." Review of Polymer Requirements for Solar Thermal Energy Systems. Proceedings of a workshop sponsored by DOE and SERI, Alexandria, VA. SERI/CP-251-1419. Golden, CO: Solar Energy Research Institute; pp. 277-326, August 1981.
5. Solar Central Receiver Prototype Heliostat, Vol. I, Final Technical Report. SAN/1604-1. Seattle, WA: Boeing Engineering and Construction Co June 1978.
6. Solar Central Receiver Prototype Heliostat, Phase I, Final Technical Report. SAN-1468-1. Schenectady, NY: The General Electric Co. October 1979.
7. United States Patent No. 4,511,215, "Lightweight Diaphragm Mirror Module System for Solar Collectors," Butler, B. L. assigned to United States Department of Energy/Solar Energy Research Institute, October 1979, issued April 16, 1985.
8. L. M. Murphy, Technical and Cost Benefits of Lightweight, Stretched-Membrane Heliostats, SERI/TR-253-1818, Golden, CO: Solar Energy Research Institute, May 1983.
9. Second Generation Heliostat Evaluation-Summary Report. SAND81-8024. Livermore, CA: Sandia Livermore Heliostat Division, Sandia National Laboratories. Note that this report estimates second-generation heliostats to cost \$110/m² in 1980 dollars; expressed in 1982 dollars this cost is \$126/m², January 1982.
10. Martin Marietta Corp., Second Generation Heliostat Optimization Studies. Contractor Report MEK-82-1700, Sandia Report SAND82-8275. Prepared for Sandia National Laboratories, Livermore, CA. May 1982.
11. Sandia National Laboratories, National Solar Thermal Technology Program - Five Year Research and Development Plan 1985-1989, Livermore, CA, December 1984.
12. McDonnell Douglas Astronautics Col, Optimization of the Second Generation Heliostat and Specification, Contractor Report MDC9762, Sandia Report SAND82-8181, prepared for Sandia National Laboratories, Livermore, CA, May 1982.

13. R. B. Pettit and E. P. Roth, "Solar Mirror Materials: Their Properties and Uses in Solar Concentrating Collectors," in Solar Materials Science, Academic Press, 1980.
14. R. B. Pettit, "Characterization of the Reflected Beam Profile of Solar Mirror Materials," Solar Energy, Vol. 19, 1977, p. 733.
15. B. H. Khoshalm, "50-kW Solar Membrane Concentrator." Presented at the Solar Thermal Collectors Workshop (Sponsored jointly by the Saudi Arabian National Center for Science and Technology and the United States Department of Energy). Sheraton Inn Lakewood, CO, April 11-14, 1983.
16. Wind Forces on Structures, ASCE Paper No. 3269, Transactions, American Society of Civil Engineers, Vol. 126, Part II, 1961.
17. L. M. Murphy, D. V. Sallis, and D. Simms, Structural Design Considerations for Stretched Membrane Heliostat Reflector Modules with Stability and Initial Imperfection Considerations, SERI/TR-253-2338, Golden, CO: Solar Energy Research Institute, Draft, May 1985.
18. L. M. Murphy, Moderate to Large Axisymmetric Deformation of Optical Membrane Surfaces, Solar Energy Research Institute, Golden, CO, April 1986.
19. L. M. Murphy and D. V. Sallis, Analytical Modeling and Structural Response of a Stretched-Membrane Reflective Module, SERI/TR-253-2101, Solar Energy Research Institute, Golden, CO, October 1986.
20. L. M. Murphy, A Variational Approach for Predicting the Load Deformation Response of A Double Stretched Membrane Reflector Module, SERI/TR-253-2626, Solar Energy Research Institute, Golden, CO, February 1985.
21. S. P. Timoshenko and J. M. Gere, Theory of Elastic Stability, Second Edition, New York: McGraw Hill, 1961.
22. R. J. Roark and W. C. Young, Formulas for Stress and Strain, Fifth Edition, New York: McGraw Hill, 1982.
23. Foundry Industry Scoping Study, Center For Metals Production, No. 86-5, November 1986.
24. Hugh Hanes and John McFadden, HIP'ing of Castings: An Update on Progress, Center For Metals Production, April 1983.
25. Plating, Finishing, and Coating: State-of-the-Art Assessment, Electric Power Research Institute, EPRI EM-4569, August 1986.

APPENDIX A
SAIC HELIOSTAT DESIGN CRITERIA

TOLERANCES

Total optical error budget for the mirror module structure:

Commercial Design - 1.0 mRad RMS Slope Error

Prototype Design - 1.2 mRad RMS Slope Error

The allowable component error breakdown for 27 mph wind is as follows:

	<u>Commercial Design</u>		<u>Prototype Design</u>	
	<u>Slope Error</u>	<u>Equivalent Deflection</u>	<u>Slope Error</u>	<u>Equivalent Deflection</u>
Truss-hub Assembly Tip Deflection	0 mRad	(.44 inch)	0 mRad	(.25 inch)
Maximum Deflection Variation Between Any Two Truss Tips	0.16 mRad	(.044 inch)	0.16 mRad	(.025 inch)
Amplified Ring Out-of-Plane Manufacturing Error (N = 2)	0.227 mRad	(.0885 inch)	0.401 mRad	(.0885 inch)
(Approximate Non-Amplified)		(.0625 inch)		(.0625 inch)

Ring Out-of-Round Error (Radius Tolerance)	.01 mRad	(.44 inch)	.01 mRad	(.25 inch)
Wind Load Deflection Error (N = 4) (4 Supports)	.60 mRad	(.165 inch)	.60 mRad	(.094 inch)
Wind Load Deflection Error (N = 5) (5 Supports)	.60 mRad	(.148 inch)	.60 mRad	(.083 inch)

MEMBRANE TENSION

The operating membrane tension (lb/ft) shall be less than one-half of the critical buckling tension for N=2 case (potato chip) which occurs due to initial imperfections. The mode shape for wind loading is N=4. The displacement amplification factor for $T = 1/2 T_{cr}$, N=2 is approximately 2.

The membrane tension shall not go below 30 lb/inch (10,000 psi for .003 mil) at the maximum operating temperature of 50°C (122°F).

The membrane stress shall not go above .6 x yield strength:

Maximum stress for annealed stainless steel = (.6) 40,000 psi = 24,000 psi

MECHANICAL PROPERTIES

Annealed 304 SS:

Tensile strength = 90,000 psi

Yield strength = 40,000 psi

Elastic modulus = 28×10^6 psi

Elongation yield to failure = 50%

Density = 0.29 lb/inch³

Coefficient of thermal expansion = 9.6 inch/inch/°Fx10⁻⁶

Rectangular Steel Tube Grade-A500B Cold Formed:

Tensile strength = 58,000 psi

Yield strength = 46,000 psi

Coefficient of thermal expansion = 8.0 inch/inch/°Fx10⁻⁶

The ring tensile stress shall not go above .6 x yield strength:

Maximum stress = (.6)(46,000) = 27,000 psi

= 27,000 psi

WIND

The wind speed specifications during daylight hours at a reference height of 10m (30 ft) shall be:

Speed Frequency

<u>Speed, m/s (mph)</u>	<u>Frequency, Percent</u>
0-2 (0-4.5)	29
2-4 (4.9-9.0)	21
4-6 (9.0-13.5)	19
6-8 (13.5-18.0)	14
8-10 (18.0-22.5)	8
10-12 (22.5-27.0)	5
12-14 (27.0-31.5)	3
14- (31.50)	Less than 1

For the calculation of wind speed at other elevations, assume the following model:

$$V_H = V_1(H/H_1)^c$$

where:

V_H = wind velocity at height H

V_1 = reference wind velocity

H_1 = reference height (assume 10 m (30 Ft))

$c = 0.15$

In computing the angle between the wind direction and the plane of the heliostat reflective surface, the wind shall be assumed to deviate by up to plus or minus 6.6° from the horizontal.

Operational Limits

The collector subsystem must meet performance requirements for the following conditions unless the component is located in a controlled environment (building).

<u>Environment</u>	<u>Level</u>
Wind, including gusts	12 m/s maximum (27 mph)
Temperature	0 to 50°C (32 to 122°F)
Gravity	All elevation angles

To achieve morning operational position or evening stow position, the heliostat will be required to function with ambient temperatures down to -9°C (16°F) and component temperatures that are colder or hotter than ambient temperatures due to thermal lag and/or absorption of direct insolation.

Stowage Initiation

The heliostats will continue to track the target with wind speeds up to 16 m/s (35 mph), but with degraded performance allowed, above which stowage action will be initiated as a result of an externally provided signal. The heliostat must maintain structural integrity in a non-operational state in a 22 m/s (50 mph) wind in any orientation.

The focus-control system will be capable of responding to the following:

Wind Rise Rate

Under normal conditions, the maximum wind rise rate is 0.01 m/s² (0.02 mph/s). A maximum wind of 22 m/s (50 mph) from any direction may occur resulting from unusual rapid wind rise rates, such as severe thunderstorm gust fronts.

Wind

The wind profile used in the mirror module modeling effort and the associated dynamic pressures are shown in Figures A-1 and A-2. The pressure profile shown in Figure C-2 is the total of the positive pressure on the upwind membrane, and negative pressure on the downwind membrane. The table below assumes 67.9% of the drag force on the upwind membrane, and 32.1% on the downwind membrane [Ref. 16]. It also assumes no deflection at the center of the front (reflective) membrane.

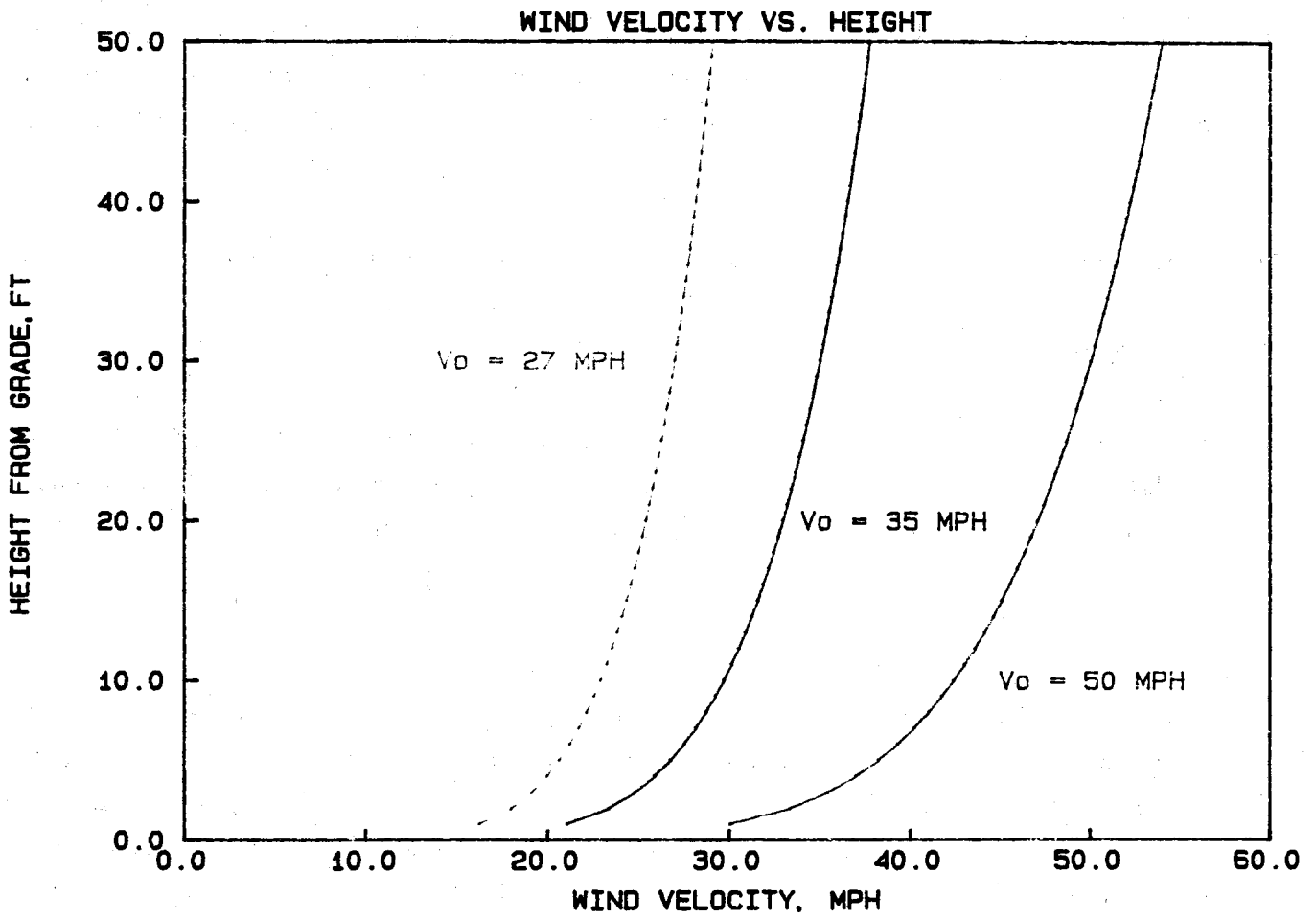


Figure A-1. Wind Velocity Profiles

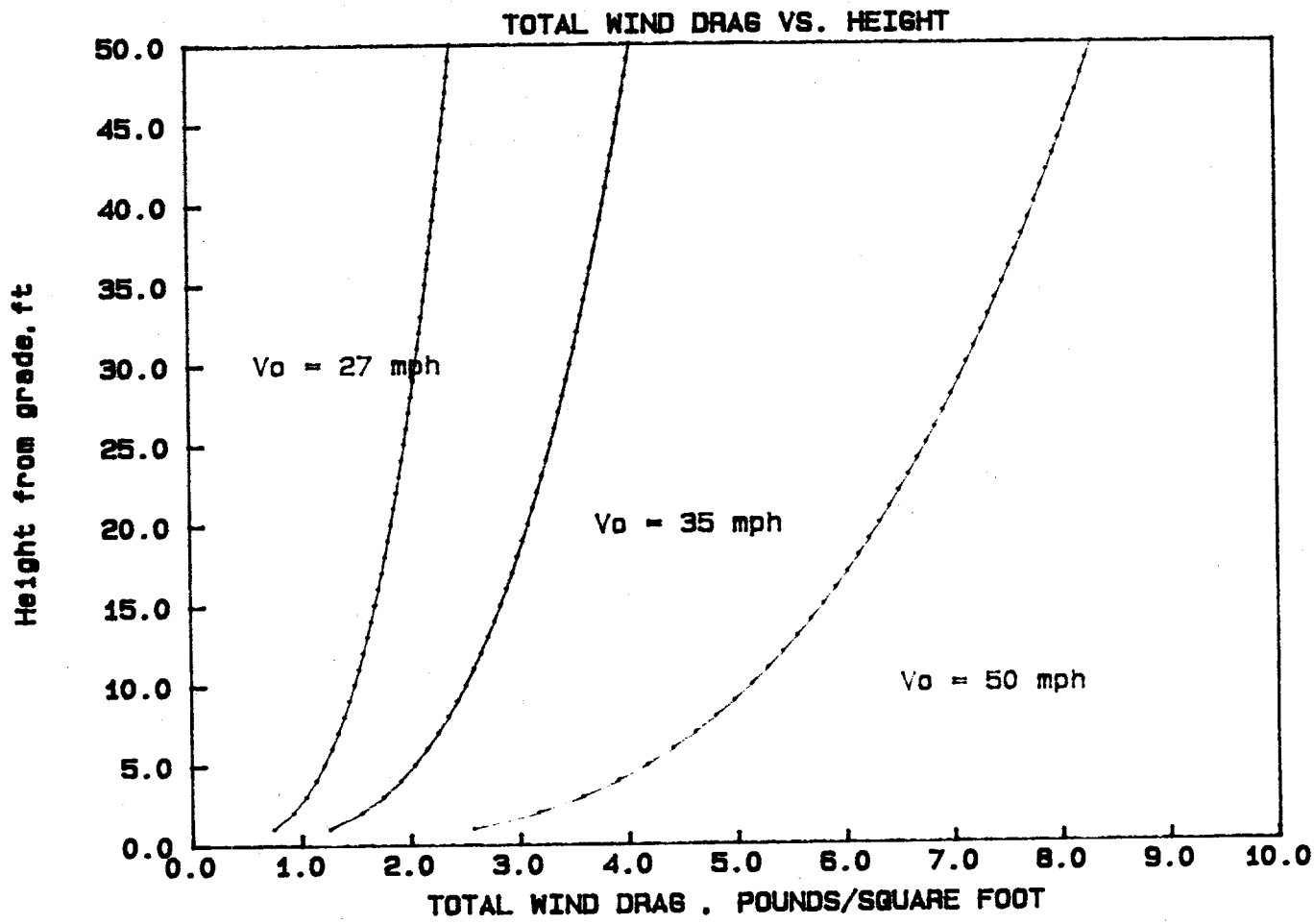


Figure A-2. Wind Drag Profiles

REQUIRED PLENUM PRESSURES

<u>Wind Speed</u>	<u>Commercial Design</u>		<u>Prototype Design</u>	
	<u>Front Membrane</u>	<u>Back Membrane</u>	<u>Front Membrane</u>	<u>Back Membrane</u>
	<u>Upwind</u>	<u>Upwind</u>	<u>Upwind</u>	<u>Upwind</u>
27 mph	.00918 psig	- .00434 psig	.00781 psig	- .00369 psig
35 mph	.0154	- .00729	.00131	- .00620
50 mph	.0315	- .0149	.0268	- .0127

These pressures will act on the inside of both membranes.

Drag Coefficients

Taken from:

"Wind Forces on Structures," ASCE Paper No. 3269, Transactions, American Society of Civil Engineers, Vol 126, Part II, 1961. [16]

The equation for moment on a flat plate about its center due to an aerodynamic load is:

$$M = \frac{1}{2} \rho L V^2 A C_m \frac{1}{32.2}$$

where (for a heliostat):

- p - air density
- V - wind velocity
- L - length of reflective area
- A - area
- C_D - drag coefficient
- C_L - lift coefficient
- C_{cp} - center of pressure coefficient
- C_m - moment coefficient

The air density was chosen to be 0.081 lbm/ft³ corresponding to approximately 32°F, 14.7 psia.

Wind velocity was calculated according to the equation:

$$V = (V_o)(h/30 \text{ ft})^{.15}$$

where:

V_o - free stream velocity in ft/sec

h - height of center of pressure above ground (ft)

The moment coefficient (C_m) was calculated from data presented in ASCE Paper No. 3269, "Wind Forces on Structures." A plot of these data is shown in Figure A-3.

The moment coefficient (C_m) was calculated based on the wind load force diagram in Figure A-4.

$$\text{Moment} = \frac{1}{2} \rho V^2 A L C_m \frac{1}{32.2}$$

$$\text{Drag} = \frac{1}{2} \rho V^2 A C_D \frac{1}{32.2}$$

$$\text{Lift} = \frac{1}{2} \rho V^2 A C_L \frac{1}{32.2}$$

$$\begin{aligned} \text{Moment} &= \text{Drag} \times L \sin a (1/2 - C_{cp}) \\ &+ \text{Lift} \times L \cos a (1/2 - C_{cp}) \end{aligned}$$

$$\frac{1}{2} \rho V^2 A L C_m = \frac{1}{2} \rho V^2 A L (1/2 - C_{cp}) (C_D \sin a + C_L \cos a) \frac{1}{32.2}$$

$$C_m = (1/2 - C_{cp}) (C_D \sin a + C_L \cos a)$$

Some results of this equation are given in Table A-I. The operating wind loads for the heliostat oriented at a 20° angle to the wind produce the highest moments.

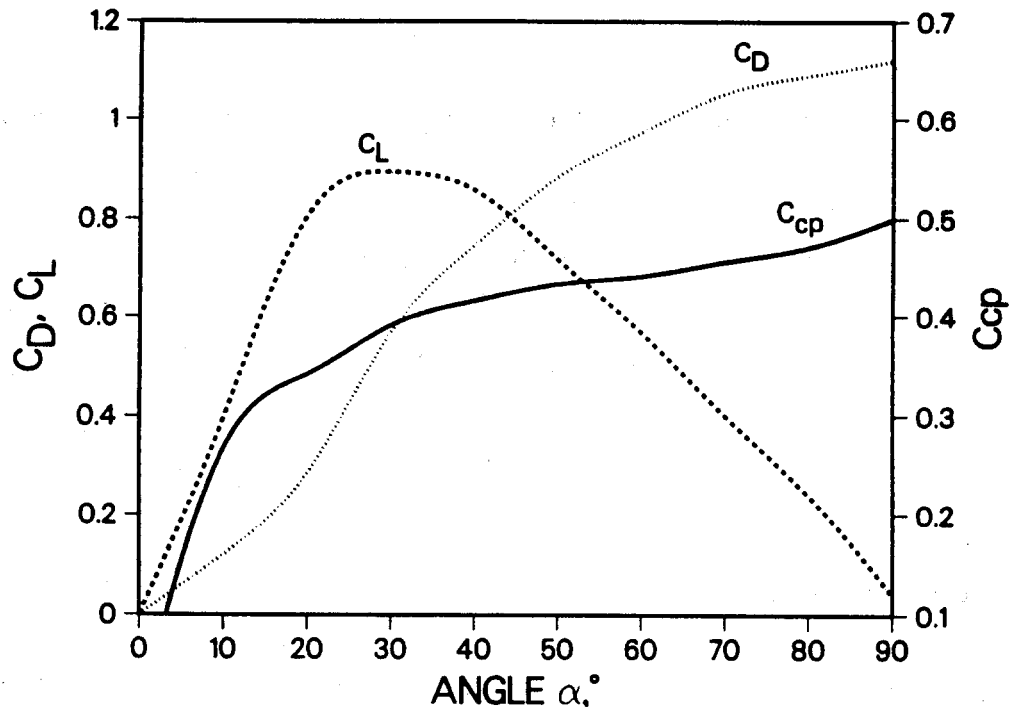


Figure A-3. Aerodynamic Coefficients

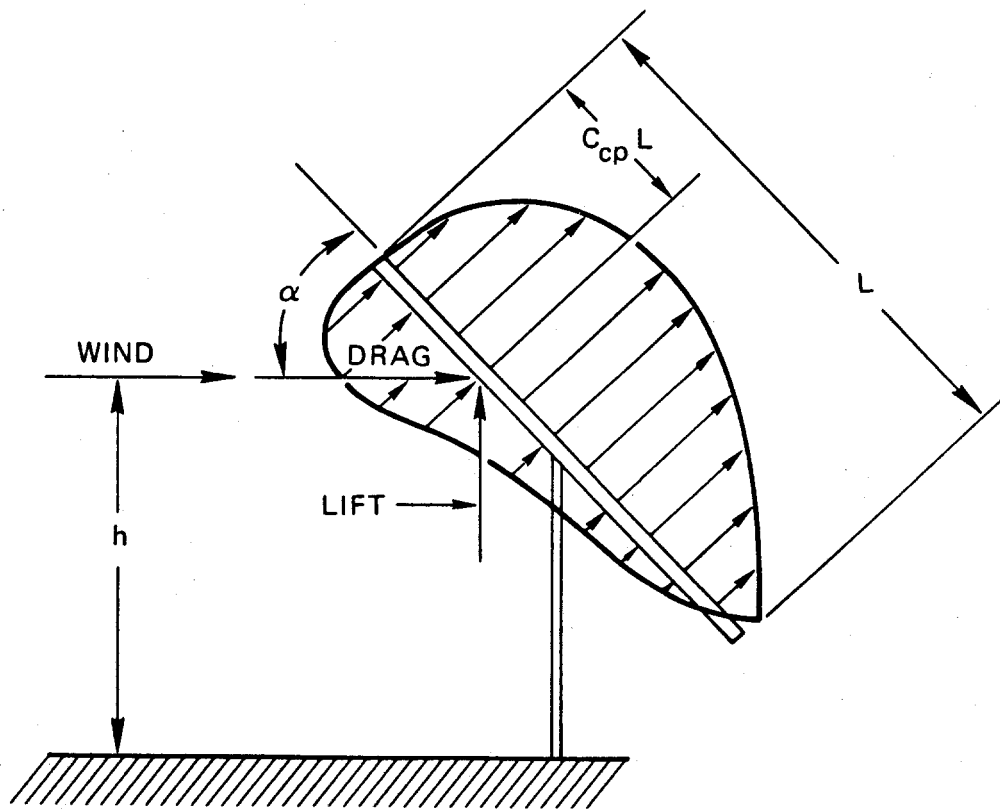


Figure A-4. Diagram of the Wind Load Force

Table A-I

AERODYNAMIC COEFFICIENTS

	C_{cp}	C_L	C_D	C_m
0	0	0	0	0
10	0.267	0.394	0.119	0.095
20	0.342	0.806	0.284	0.135
30	0.391	0.893	0.567	0.115
40	0.416	0.857	0.746	0.084
50	0.433	0.716	0.884	0.076
60	0.441	0.567	0.973	0.066
70	0.456	0.400	1.054	0.050
80	0.471	0.239	1.090	0.03
90	0.500	0.040	1.120	0

FOCUS CONTROL REQUIREMENTS

The prototype design shall include the supporting ring, membranes, mirror surface, supporting structure, focal length control, and all equipment above the drive unit. A remote control unit shall be included to allow the operational focal length set point to be changed to any value between 200 meters and infinity. The pressure control unit shall have the capability of changing the mirror contour from any focal length within the operational range to the "emergency" convex state (focal length of - 200-m) within five seconds. It is also desirable that the unit provide a fail-safe characteristic such that the membrane mirror reverts to the convex state upon loss of power or communication.

APPENDIX B

*STRUCTURAL/OPTICAL COUPLING EQUATIONS DERIVATION

As shown in Figure B-1 for a circular ring of radius a , lying in or near the x-y plane, center at origin, the z-displacement (out-of-plane) is given by:

$$z(a, \theta) = \sum_{n=0}^{\infty} A_n \cos [n(\theta + \phi_n)] \quad [1]$$

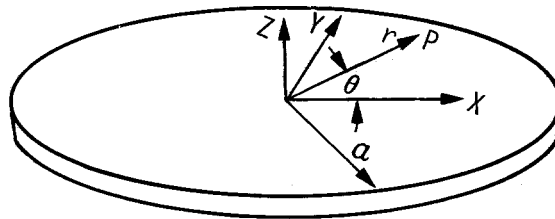


Figure B-1 Coordinate System

An ideal membrane supported by this ring will take the shape defined by

$$z(r, \theta) = \sum_{n=0}^{\infty} A_n (r/a)^n \cos[n(\theta + \phi_n)] \quad [2]$$

(Note:

n=0 term is piston motion, or simple z displacement with no rotation nor deformation.

n=1 term is simple rigid body rotation, which is a pointing or tracking error, not slope error.

n=2 term is the so-called potato chip shape.

n>2 term are similar saddle shapes with n high spots and n low spots on the circumference of the rim.

(All can coexist, and the displacements linearly superimpose.)

* Obtained from the Solar Energy Research Institute

MEMBRANE/FRAME DEFORMATION RELATED POINTING OR TRACKING ERROR

An effective pointing or tracking error results from deformation of the ring frame structure due to asymmetrical loading (most wind loads). This is independent of the deformation of the support structure due to the same loads, and causes an additional error, which should be included in design calculations.

The effective angular rotation is given by

$$\beta = A_1/a \quad [3]$$

SHAPE CHANGES, $n > 1$ TERMS.

The $n = 0$ and 1 terms are simple translation and rotation of the membrane/frame, and do not constitute shape changes. We therefore classify the $n > 1$ terms as contributing to slope error. For computing slope errors, we include only the $n = 2, 3, 4, \dots$ terms.

SLOPE AT A POINT ON THE MEMBRANE

At any point P on the membrane surface, the magnitude of the slope is given by

$$\gamma_p = \left[\left(\frac{dz}{dr} \right)^2 + \left(\frac{1}{r} \frac{dz}{d\theta} \right)^2 \right]^{1/2} \quad [4]$$

For a surface defined by [2], the slope at point P, relative to average mirror normal direction, is

$$\gamma_p = \left\{ \left[\frac{d}{dr} \sum_{n=2}^{\infty} A_n (r/a)^n \cos[n(\theta + \phi_n)] \right]^2 + \left[\frac{1}{r} \frac{d}{d\theta} \sum_{n=2}^{\infty} A_n (r/a)^n \cos[n(\theta + \phi_n)] \right]^2 \right\}^{1/2}$$

(continued)

$$\begin{aligned}
&= \left\{ \left[\sum_{n=2}^{\infty} \frac{n A_m}{a^m} r^{n-1} \cos[n(\theta + \phi_n)] \right]^2 \right. \\
&\quad \left. + \left[\frac{1}{r} \sum_{n=2}^{\infty} \frac{n A_m}{a^m} r^n \sin[n(\theta + \phi_n)] \right]^2 \right\}^{1/2} \\
&= \left\{ \left[\sum_{n=2}^{\infty} \frac{n A_m}{a^m} r^{n-1} \cos[n(\theta + \phi_n)] \right]^2 \right. \\
&\quad \left. + \left[\sum_{n=2}^{\infty} \frac{n A_m}{a^m} r^{n-1} \sin[n(\theta + \phi_n)] \right]^2 \right\}^{1/2} \quad [5]
\end{aligned}$$

SURFACE RMS SLOPE

$$\begin{aligned}
\gamma_{\text{RMS}} &= \left[\frac{\int_A \gamma_p^2 dA}{\int_A dA} \right]^{1/2}, \quad dA = r d\theta dr, \\
\pi a^2 \left[\gamma_{\text{RMS}} \right]^2 &= \int_0^a \int_0^{2\pi} \left[\sum_{n=2}^{\infty} \frac{n A_m}{a^m} r^{n-1} \cos[n(\theta + \phi_n)] \right]^2 r d\theta dr \\
&\quad + \int_0^a \int_0^{2\pi} \left[\sum_{n=2}^{\infty} \frac{n A_m}{a^m} r^{n-1} \sin[n(\theta + \phi_n)] \right]^2 r d\theta dr \quad [6] \\
&= \int_0^a \int_0^{2\pi} \left[\sum_{n=2}^{\infty} \left(\frac{n A_m}{a^m} \right)^2 r^{2n-2} \cos^2 [n(\theta + \phi_n)] \right] r d\theta dr
\end{aligned}$$

(continued)

$$\begin{aligned}
& + \int_0^a \int_0^{2\pi} \sum_{n=2}^{\infty} \left(\frac{n A_n}{a^n} \right)^2 r^{2n-2} \sin^2 [n(\theta + \phi_n)] r d\theta dr \\
& + 2 \int_0^a \int_0^{2\pi} \sum_{\substack{n=2 \\ m=n+1}}^{\infty} \left(\frac{n A_n}{a^n} \right) \left(\frac{m A_m}{a^m} \right) r^{m+n-2} \cos [n(\theta + \phi_n)] \cos [m(\theta + \phi_m)] r d\theta dr \\
& + 2 \int_0^a \int_0^{2\pi} \sum_{\substack{n=2 \\ m=n+1}}^{\infty} \left(\frac{n A_n}{a^n} \right) \left(\frac{m A_m}{a^m} \right) r^{m+n-2} \sin [n(\theta + \phi_n)] \sin [m(\theta + \phi_m)] r d\theta dr
\end{aligned}$$

or,

$$\begin{aligned}
\pi a^2 [\gamma_{\text{RMS}}]^2 & = \int_0^a \int_0^{2\pi} \sum_{n=2}^{\infty} \left(\frac{n A_n}{a^n} \right)^2 r^{2n-1} d\theta dr \\
& + 2 \int_0^a \int_0^{2\pi} \sum_{\substack{n=2 \\ m=n+1}}^{\infty} \left(\frac{n A_n}{a^n} \right) \left(\frac{m A_m}{a^m} \right) r^{m+n-1} \\
& \left[\cos [n(\theta + \phi_n)] \cos [m(\theta + \phi_m)] + \sin [n(\theta + \phi_n)] \sin [m(\theta + \phi_m)] \right] d\theta dr \\
& = 2\pi \sum_{n=2}^{\infty} \left(\frac{n A_n}{a^n} \right)^2 \int_0^a r^{2n-1} dr \\
& + 2 \int_0^a \sum_{\substack{n=2 \\ m=n+1}}^{\infty} \left(\frac{n A_n}{a^n} \right) \left(\frac{m A_m}{a^m} \right) r^{m+n-1} \int_0^{2\pi} \cos [n(\theta + \phi_n) - m(\theta + \phi_m)] d\theta dr \\
& = 2\pi \sum_{n=2}^{\infty} \left(\frac{n A_n}{a^n} \right)^2 \frac{a^{2n}}{2n}
\end{aligned}$$

(continued)

$$+ 2 \int_0^a \sum_{\substack{n=2 \\ m=n+1}}^{\infty} \left(\frac{n A_n}{a^n} \right) \left(\frac{m A_m}{a^m} \right) r^{m+n-1} \int_0^{2\pi} \cos[(n-m)\theta + n\phi_n - m\phi_m] d\theta dr$$

$$\pi a^2 \left[\gamma_{\text{RMS}} \right]^2 = 2\pi \sum_{n=2}^{\infty} \left(\frac{n A_n}{a^n} \right)^2 \frac{a^{2n}}{2n}$$

Finally, we see that the RMS "slope error" ($n > 1$ terms in deformation expression) is given by

$$\left[\gamma_{\text{RMS}} \right]^2 = \sum_{n=2}^{\infty} n \left(\frac{A_n}{a} \right)^2 \quad [7]$$

where the values of A_n are the coefficients from the ring deformation equation [1], and "a" is the radius of the ring.

PROCEDURE FOR ESTIMATING RMS SLOPE ERROR AND POINTING ERROR

If, by experiment or by finite element analysis, one obtains estimates of the frame z-displacement at many points, N, around the frame, then a fit of equation [1] can be made to those data. This involves finding the A_n and ϕ_n for a suitable number of terms in the equation for instance, by a least squares method. For numerical stability it is suggested that the number of terms be limited to one less than the square root of the number of data points you have, that is.

$$z(a, \theta) = \sum_{n=0}^k A_n \cos[n(\theta + \phi_n)] , \quad k < \sqrt{N} - 1$$

Then, having obtained the A_n values, equation [7] can be used to estimate the RMS slope of the frame.

EXAMPLE

Consider a flat membrane/frame rigidly supported at six points. A uniform wind load is imposed, causing a deflection of the rim that is for the most part $n=6$ buckling, with a little $n=12, 18, 24, \dots$ thrown in. For our purposes, we might assume that it is pure $n=6$. Suppose that on the 6-m diameter ring, the deflection is found to be 10-mm. The equation for the ring would then be

$$z(a, \theta) = A_0 + A_6 \cos[6(\theta + \phi_6)]$$

or,

$$z(3, \theta) = -0.005 + 0.005 \cos[6\theta]$$

In this case, there is an average 5-mm displacement of the whole membrane frame with a 5-mm amplitude cosine wave superimposed. There is no tilt or pointing error, since $A_1 = 0$. The RMS slope error is

$$\gamma_{\text{RMS}} = \sqrt{6} \frac{0.005}{3.0} = 0.00408 = 4 \text{ mrad,}$$

If the displacement is given by

$$z(3, \theta) = -0.0055 + 0.005 \cos[6\theta] + 0.001 \cos[12\theta],$$

which is more likely (due to a distributed wind load reacted by point supports), then the RMS slope error is

$$\gamma_{\text{RMS}} = \left[6 \left(\frac{0.005}{3.0} \right)^2 + 12 \left(\frac{0.001}{3.0} \right)^2 \right]^{1/2} = 4.24 \text{ mrad.}$$

So, even though the edge displacement is the same, the relatively small higher order term appreciably increases the RMS slope error. Therefore, the higher order terms should not be neglected.

APPENDIX C

BENCH SCALE TENSIONING EXPERIMENT - OPERATING PROCEDURE

The operation of the bench-scale tensioning device is as follows:

- System pressure is controlled by the relief valve on the manifold protruding from the top of the fluid tank on the floor. To change system pressure, turn unit on, loosen lock nut on relief valve, turn adjustment screw: clockwise to increase pressure, counter-clockwise to decrease pressure setting. When desired pressure is reached on pressure gauge, tighten lock nut.
- Maximum system working pressure is 1500 psi. NEVER RUN THE SYSTEM ABOVE 1500 psi.
- The maximum system working pressure is based on the hydraulic equipment limitations. Due to mechanical limitations in the current system configuration, it is recommended to run the system BELOW 750 psi.

GRIPPING PROCEDURE:

- Turn unit on.
- To actuate gripping cylinders pull back on the left lever. Flow control and pressure control can be accomplished by adjusting the knobs on the valve cartridges. The gripper circuit is the bottom circuit, so adjusting the bottom flow control valve or pressure control valve will only affect the gripper circuit. When the left lever is released the grippers will remain closed. There is a check valve in the gripper circuit so they will remain closed and fully pressurized until the left lever is pushed forward. Doing so will activate the check valve pilot and the grippers will open. NEVER OPEN GRIPPERS WHEN THEY ARE HOLDING A SAMPLE UNDER TENSION.

TENSIONING PROCEDURE:

- Once a sample has been gripped, it can be tensioned. The middle lever on the directional control valve block controls the pushing cylinders. Pulling back on this lever extends the cylinders, while pushing forward on the middle lever retracts the pushing cylinders. The middle flow control and pressure control valves control the pushing circuit. Adjusting the middle valves will only affect the pushing circuit.

- The right lever on the directional control valve block controls the pulling cylinders. Pulling back on this lever retracts the pulling cylinders, while pushing in on the right lever extends the pulling cylinders. The top flow control and pressure control valves control the pulling circuit. Adjusting the top valves will only affect the pulling circuit.

- The pushing and pulling action must be coordinated to push on the rectangular tube section while simultaneously pulling on the sample. NOTE: There is no check valve in the pushing and pulling circuits so that if the control levers are released, these circuits will slowly depressurize.

ENGINEERING DATA:

CYLINDER	DIRECTION	EFFECTIVE CYLINDER PISTON AREA (Inch ²)
-----	-----	-----
Gripper	extend	0.442
	retract	0.393
Pusher	extend	1.485
	retract	1.296
Puller	extend	1.485
	retract	1.296

Revised 5/89
UNLIMITED RELEASE
INITIAL DISTRIBUTION

U.S. Department of Energy (6)
Forrestal Building
Code CE-314
1000 Independence Avenue, SW
Washington, DC 20585
Attn: H. Coleman
S. Gronich
F. Morse
M. Scheve
R. Shivers
T. Wilkins

U.S. Department of Energy
Forrestal Building
Code CE-33
1000 Independence Avenue, SW
Washington, DC 20585
Attn: C. Carwile

U. S. Department of Energy
CE-1, Forrestal
1000 Independence Avenue, SW
Washington, DC 20585
Attn: D. Fitzpatrick

U.S. Department of Energy (2)
Albuquerque Operations Office
P.O. Box 5400
Albuquerque, NM 87115
Attn: D. Graves
G. Tennyson

U.S. Department of Energy
San Francisco Operations Office
1333 Broadway
Oakland, CA 94612
Attn: R. Hughey

Advanced Thermal Systems
7600 East Arapahoe
Suite 215
Englewood, CO 80112
Attn: D. Gorman

Allegheny Ludlum Steel (2)
Market and Product Development
Alabama and Pacific Avenues
Brackenridge, PA 15014
Attn: Joseph M. Hunt
John P. Ziemianski

Allegheny Ludlum Steel
80 Valley St.
Wallingford, CT 06492
Attn: John J. Halpin

Analysis Review & Critique
6503 81st Street
Cabin John, MD 20818
Attn: C. LaPorta

Arizona Public Service Company
P.O. Box 53999
Phoenix, AZ 85072-3999
Attn: W. J. McGuirk M/S 9110

Arizona Solar Energy Office
Dept. of Commerce
1700 W. Washington, 5th Floor
Phoenix, AZ 85007
Attn: Dr. Frank Mancini

Asinel
Ctra. Villaviciosa
de Odón a Móstoles
Km 1,700
28935 Móstoles
Madrid Spain
Attn: Jesús M. Mateos

Atlantis Energy Ltd.
Thunstrasse 43a
3005 Bern, Switzerland
Attn: Mario Posnansky

Babcock and Wilcox
91 Stirling Avenue
Barberton, OH 44203
Attn: D. Young

Battelle Pacific Northwest
Laboratory
P.O. Box 999
Richland, WA 99352
Attn: T. A. Williams

Bechtel National, Inc. (4)
50 Beale Street
50/15 D8
P. O. Box 3965
San Francisco, CA 94106
Attn: P. DeLaquil
B. Kelly
J. Egan
R. Leslie

Black & Veatch Consulting
Engineers (4)
P.O. Box 8405
Kansas City, MO 64114
Attn: J. C. Grosskreutz
J. E. Harder
L. Stoddard
J. Arroyo

Bomin Solar
Industriestr. 8
D-7850 Lorrach
Federal Republic of Germany
Attn: Dr. Hans Jurgen Kleinwachter

Tom Brumleve
1512 Northgate Road
Walnut Creek, CA 94598

California Energy Commission
1516 Ninth Street, M-S 43
Sacramento, CA 95814
Attn: A. Jenkins

California Polytechnic University
Dept. of Mechanical Engineering
3801 West Temple Ave.
Pomona, CA 91768-4062
Attn: W. Stine

California Public Utilities Com.
Resource Branch, Room 5198
455 Golden Gate Avenue
San Francisco, CA 94102
Attn: T. Thompson

Center for Energy and
Environmental Research
GPO Box 3682
San Juan, PR 00936
Attn: Director

Centro Investigaciones Energeticas (2)
Medioambiental Tecnologica (CIEMAT)
Avda. Complutense, 22
28040 Madrid
SPAIN
Attn: F. Sanchez
M. Romero

Danka Products
3905 S. Mariposa St.
Englewood, CO 80110
Attn: Dan Sallis

DLR EN-TT (2)
Institute for Technical
Thermodynamics
Pfaffenwaldring 38-40
7000 Stuttgart 80
Federal Republic of Germany
Attn: Dr. C. Winter
Dipl. Ing R. Buck

DLR
Linder Hoehe
5000 Cologne 90
Federal Republic of Germany
Attn: Dr. Manfred Becker

El Paso Electric Company
P.O. Box 982
El Paso, TX 79946
Attn: J. E. Brown

Electric Power Research
Institute (2)
P.O. Box 10412
Palo Alto, CA 94303
Attn: J. Bigger
E. DeMeo

Engineering Perspectives
20 19th Avenue
San Francisco, CA 94121
Attn: John Doyle

Flachglas Solartechnik GmbH
Muhllengasse 7
D-5000 Koln 1
Federal Republic of Germany
Attn: Joachim Benemann

Flachglas Solartechnik GmbH
Sonnesstr. 25
D-8000 Munchen 1
Federal Republic of Germany
Attn: Dr. Michael Geyer

Foster Wheeler Solar Development
Corporation (2)
12 Peach Tree Hill Road
Livingston, NJ 07039
Attn: S. F. Wu
R. Zoschak

Georgia Institute of Technology
GTRI/EMSL Solar Site
Atlanta, GA 30332
Attn: T. Brown

Georgia Power
7 Solar Circle
Shenandoah, GA 30265
Attn: Ed. Ney

Leo Gutierrez
434 School Street
Livermore, CA 94550

HGH Enterprises, Inc.
23011 Moulton Parkway
Suite C-13
Laguna Hills, CA 92653
Attn: Dick Holl

Interatom GmbH (2)
P. O. Box
D-5060 Bergisch-Gladbach
Federal Republic of Germany
Attn: M. Kiera
W. Meinecke

Lawrence Berkeley Laboratory
MS 90-2024
One Cyclotron Road
Berkeley, CA 94720
Attn: Arlon Hunt

Los Angeles Department of Water
and Power
Alternate Energy Systems
Room 661A
111 North Hope Street
Los Angeles, CA 90012
Attn: Bill Engels

Luz International (2)
924 Westwood Blvd.
Los Angeles, CA 90024
Attn: D. Kearney
M. Lotker

Meridian Corporation
4300 King St.
Suite 400
Alexandria, VA 22302-1508
Attn: D. Kumar

MITI
Electrotechnical Laboratory
Solar Energy Applications Section
1-1-4 Umezono, Tsukuba
Ibaraki 305, Japan
Attn: Koichi Sakuta

Nevada Power Co.
P. O. Box 230
Las Vegas, NV 89151
Attn: Mark Shank

ORMAT Energy Systems, Inc.
610 East Glendale Ave.
Sparks, NV 89431-5811
Attn: Dr. Lucien Bronicki

Peerless Winsmith, Inc.
172 Eaton St.
P. O. Box 530
Springville, NY 14141
Attn: W. Hellar

Platforma Solar de Almeria
Aptdo. 7
Tabernas (Almeria)
E-04200 Spain

Public Service Company of New Mexico
M/S 0160
Alvarado Square
Albuquerque, NM 87158
Attn: T. Ussery
A. Martinez

Pacific Gas and Electric Company (3)
3400 Crow Canyon Road
San Ramon, CA 94526
Attn: G. Braun
T. Hillesland
B. Norris

Polydyne, Inc.
1900 S. Norfolk Street, Suite 209
San Mateo, CA 94403
Attn: P. Bos

PSI (2)
CH-5303 Wurenlingen
Switzerland
Attn: W. Durish
P. Kesselring

Public Service Company of Colorado
System Planning
5909 E 38th Avenue
Denver, CO 80207
Attn: D. Smith

Ramada Energy Systems Ltd.
1421 S. McClintock Drive
Tempe, AZ 85281
Attn: R. Bingman

San Diego Gas and Electric Company
P.O. Box 1831
San Diego, CA 92112
Attn: R. Figueroa

SCE
P. O. Box 800
Rosemead, CA 91770
Attn: W. vonKleinSmid

Schlaich, Bergermann & Partner
Hohenzollernstr. 1
D-7000 Stuttgart 1
Federal Republic of Germany
Attn: Wolfgang Schiel

Sci-Tech International
Advanced Alternative Energy
Solutions
5673 W. Las Positas Boulevard
Suite 205
P.O. Box 5246
Pleasanton, CA 84566
Attn: Ugur Ortabasi

Science Applications
International Corporation
10260 Campus Point Drive
San Diego, CA 92121
Attn: B. Butler

Science Applications
International Corporation (10)
10401 Roselle Street
San Diego, CA 92121
Attn: J. Sandubrae
K. Beninga (9)

Solar Energy Research Institute (8)
1617 Cole Boulevard
Golden, CO 80401
Attn: B. Gupta
L. M. Murphy
P. Schissel
T. Wendelin
J. Anderson
R. Wood
A. Lewandowski
M. Carasso

Solardämmerung, GmbH
Attn: Prof. Dr. Fahren Mit Phaëton
2403 Georgene Dr. NE
Albuquerque, NM 87112 USA

Solar Kinetics, Inc. (4)
P.O. Box 540636
Dallas, TX 75354-0636
Attn: J. A. Hutchison
D. White
A. Konnerth
P. Schertz

Solar Power Engineering Company
P.O. Box 91
Morrison, CO 80465
Attn: H. C. Wroton

Solar Stream
P. O. Box 32
Fox Island, WA 98333
Attn: D. Wood

Southern California Edison
P.O. Box 325
Daggett, CA 92327
Attn: C. Lopez

Stearns Catalytic Corporation
P.O. Box 5888
Denver, CO 80217
Attn: T. E. Olson

Stone and Webster Engineering
Corporation
P.O. Box 1214
Boston, MA 02107
Attn: R. W. Kuhr

Sulzer Bros, Ltd.
New Technologies
CH-8401 Winterthur
Switzerland
Attn: Hans Fricker, Manager

Tom Tracey
6922 South Adams Way
Littleton, CO 80122

United Solar Tech, Inc.
3434 Martin Way
Olympia, WA 98506
Attn: R. J. Kelley

University of Arizona
Engineering Experimental Station
Harvil Bldg., Room 151-D
Tucson, AZ 85721
Attn: Don Osborne

University of Houston (3)
Solar Energy Laboratory
4800 Calhoun
Houston, TX 77704
Attn: A. F. Hildebrandt
L. Vant-Hull
C. Pitman

University of Utah
Mechanical and Industrial
Engineering
Salt Lake City, UT 84112
Attn: B. Boehm

Eric Weber
302 Caribbean Lane
Phoenix, AZ 85022

WG Associates
6607 Stonebrook Circle
Dallas, TX 75240
Attn: V. Goldberg

3M Corp.
3M Center
Building 207-1W-08
St. Paul, MN 55144
Attn: B. A. Benson

Universidad del Turabo
attn: Eng. J. V. Otts
Dean, Dept. of Engineering
Box 3030
University Station
Gurabo, PR 00658

Clayton Mavis
626 Tina Way
Livermore, CA 94550

3141-1 S. A. Landenberger (5)
3151 W. I. Klein (3)
3154-1 C. L. Ward (8)
For DOE/OSTI
6200 V. L. Dugan
6210 B. W. Marshall
6215 J. T. Holmes
6215 K. R. Boldt
6215 C. P. Cameron
6215 R. M. Houser
6215 Library (15)
6216 D. J. Alpert (5)
6216 J. W. Grossman
6216 J. E. Pacheco
6216 C. E. Tyner
6216 L. Yellowhorse
6216 T. R. Mancini
6217 P. C. Klimas
8024 P. W. Dean
8133 A. C. Skinrood
8165 C. L. Mavis
8524 J. A. Wackerly



8232-2/069187



00000001 -



8232-2/069187



00000001 -



8232-2/069187



00000001 -

